

POLITECNICO DI TORINO

Master's Degree in Mechanical Engineering



Master's Degree Thesis

Effect of Process Parameters on the Quality of 17-4 PH Samples Produced by Directed Energy Deposition

Tutors:

Federica Bondioli

Alberta Aversa

Alessandro Carrozza

Erica Librera

Candidate:

Lorenzo Badi

April 2021

Contents

Abstract	2
1 Additive Manufacturing Technologies	3
1.1 Brief History of AM Development	5
1.2 Generic AM process.....	7
1.3 Classification of AM processes	9
1.3.1 Powder Bed Fusion	10
1.3.2 Directed Energy Deposition.....	11
1.4 Metal Powder Manufacturing	15
2 Stainless steel.....	17
2.1 17-4 PH	19
2.1.1 AM microstructure	19
2.1.2 Mechanical properties.....	22
3 Materials and Methods.....	24
3.1 DED Machine in Prima Additive.....	24
3.2 Powder.....	26
3.3 Single Scan Tracks.....	30
3.4 Massive Cubes	33
4 Results and Discussion	38
4.1 Powder.....	38
4.2 Single Scan Tracks.....	42
4.3 Cubes	50
4.3.1 Porosity.....	52
4.3.2 Microstructure.....	68
4.3.3 Hardness	70
5 Conclusions	74
References.....	75

Abstract

This thesis project is the result of the collaboration between Politecnico di Torino and Prima industrie S.p.A. The group Prima Industrie operates in the field of the mechanical industry, in particular it develops, manufacture and markets lasers, sheet metal cutting machinery, electronics, CNCs components and additive manufacturing systems. This last field is the most recent and is managed by the newly constituted Prima Additive division. It deals with both Directed Energy Deposition and Powder Bed Fusion technologies.

Directed Energy Deposition is an innovative Additive Manufacturing method that represents the evolution of the cladding technology. However, it is still on evolution, and, for this reason, the process parameters must be evaluated and optimized case by case. In the framework of a scientific support, Prima Additive assigned the analysis of single scan tracks and massive cubes samples made of 17-4 PH. The single scan tracks were produced covering a wide range of process parameters and the aim was providing a correlation between the process parameters and the meltpools' characteristics. The massive cubes, instead, were printed using different sets of parameters selected by the experience with the objective of analysing their quality.

In this dissertation, the state of the art of Additive Manufacturing technologies is described, focusing on the metal based ones and presenting the metal powder production. Then, the 17-4 PH stainless steel is presented, providing an outline of its characteristics when used in Additive Manufacturing processes. The experimental section of the thesis describes the machine of Prima Additive, the powder feedstock used, how the samples were produced, prepared, and characterized. The feedstock powder was analysed in terms of particle size distribution, flowability and tap density. It was observed an excellent flowability, crucial for DED applications. Then, the on-top and the cross-section observations were carried on the single scan tracks, defining the deposition effectiveness and the meltpools' geometrical characteristics. Some correlations between them and process parameters were found. The massive cubes' quality was analysed in terms of porosity, microstructure, and hardness. Generally, they had high hardness and good porosity values, even if few sets of parameters showed more defects than others. In conclusion, the single scans' analysis allowed to exclude the most critical sets of process parameters while the overall most promising sets were found through the massive cubes' analysis.

1 Additive Manufacturing Technologies

The term *Additive Manufacturing* (AM) denotes the industrial process of fabricating an object, by the addition of layers, from a 3D CAD model (**Fig. 1.1**). This innovative technology is particularly suitable for complex shaped components that would be impossible, or inconvenient, to produce using traditional subtracting methods [1]. The term *3D-printing* is informal and used by the general public or in a domestic DIY context.

The first commercialized machines date back to the mid-80s, when the first patent was filed in the USA. In this period, this technology was used only to build conceptual prototypes and so was known as *Rapid Prototyping* (RP). The main advantage was that the model was built in short time, few hours, without tools nor process planning required. Afterwards, not only prototypes but also casting patterns (*Rapid Casting*) and tools (*Rapid Tooling*) were built. During the last two decades, the expression *Additive Manufacturing* has been spreading, since end-useable parts could be produced, reaching the highest and most valuable application of the technology [1].

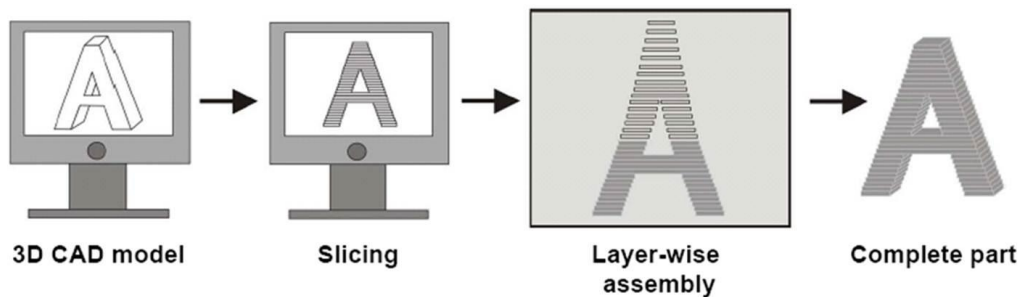


Fig. 1.1 General additive manufacturing process [2]

Nowadays, amongst manufacturing processes, AM technologies are the fastest growing in the global market and they are becoming faster and cheaper year after year [3]. The advantages of adopting these technologies are both in process and product: one machine can produce almost any kind of shape in just one manufacturing step and without needing a mould or special tools, leading to a reduced operator intervention [4]. So, thanks to the design freedom, complex hollow shapes can be created, obtaining an optimized and lightweight product. Consequently, in AM time and costs are only related to size, not to complexity, in first approximation. Traditional manufacturing, instead, is based on subtractive processes and requires a certain level of human interaction, for example, part must be repositioned or relocated within the machine or even in a different one. In this case, the cost of a component strongly depends on its complexity, as schematized in **Fig. 1.2**.

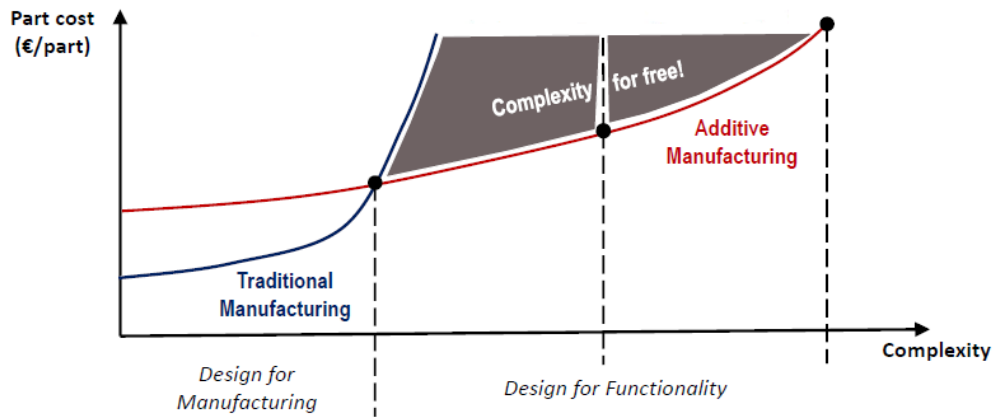


Fig. 1.2 Comparison between part costs in traditional manufacturing and AM [4]

On the other hand, AM technologies are a fairly new and still evolving reality, thus they have some drawbacks that restrict their field of application. First of all, large objects cannot be produced due to the working chamber size limitations and, in some cases, due to lack of strength in the material itself. Building large objects might also be impractical due to the limited machine speed [5]. Then, even if prices are falling, both machines and materials are still expensive, so onerous investments from the companies are usually required [6]. Also, the materials choice is currently limited and these are mostly polymers [4]. At the end, object produced through AM often have some imperfections in the superficial finish that might result ribbed and rough [6]. For this reason, a certain amount of post-processing is typically required.

Even if many researches and improvements have been carried on during the last decades, it is unrealistic that AM techniques will make the traditional ones obsolete. It is expected, instead, that AM will progressively increase its role as complementary technology in the industrial landscape [6].

1.1 Brief History of AM Development

The concept of producing a 3D object layer by layer occurred long before the advent of CAD software or AM ideas.

One of the first patents dates back to 1902: George J. Peacock filed a patent for laminated horseshoes “*Method of making composition horseshoes*” [7]. It consisted of many layers of strong fabric with a thin rubber in between. The attempt was to create custom horseshoes in a much easier way than in the traditional methods.

The origins of the real AM technology, however, are intricate to define. There were definitely a lot of researches in the 1950s and 1960s, but the applications became effective only thanks to remarkable development of associated technologies, such as computers, lasers, controllers, CNC machines etc. in the early 1980s [1]. The first material used in AM was a photopolymer resin, invented in the 1950s by the chemical industry DuPont (Wilmington, Delaware) [8]. Through a process called polymerization, the liquid resin hardened when exposed to a light source, such as a laser. From the late 60s to the 80s many studies and experiments on the resin were carried out, mostly in USA, but also in Japan and France [1].

In 1984, Charles Hull of UVP, Inc. (San Gabriel, California) invented and filed the first stereolithography apparatus to produce three-dimensional objects [9]. He described a process of directing a computer-controlled UV laser beam in a vat of photopolymer resin: 3D prototypes were formed by curing the resin layer by layer while submerging the build platform deeper into the vat while between [8] (**Fig. 1.3**).

In 1986, Hull and Raymond Freed co-founded 3D Systems Inc. (Valencia, California) [10]. The following year, SLA-1 system was launched: (**Fig. 1.4**) this was the first ever commercialized AM system in the world and showed impressively detailed parts for that time [8].

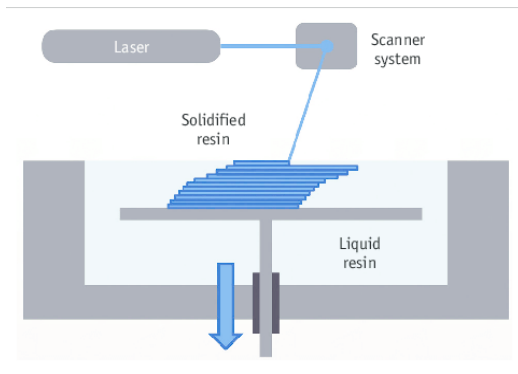


Fig. 1.3 Basic working principle of stereolithography apparatus [12]



Fig. 1.4 The SLA-1 system: the first AM technology launched in 1987 by 3D systems [1]

In the following years, Japanese companies were particularly concentrated on improving stereolithography processes, while companies in USA and Israel were developing other approaches to additive manufacturing [8]. The most of AM technologies, indeed, was invented during the 90s.

The first *Fused Deposition Modelling* (FDM) was commercialized by Stratasys (Eden Prairie, Minnesota) in 1991 [3]. A thermoplastic material was extruded in filament form through a computer-controlled deposition head, creating a 3D object [6]. In 1993 the Massachusetts Institute of Technology patented the *Binder Jetting* (BJ): an inkjet mechanism added droplets of liquid binder i.e., glue to layers of ceramic powder [3]. In particular, Soligen, Inc. (Northridge, California) applied this principle and commercialized the *Direct Shell*

Production Casting (DSPC), informally called *Rapid Casting*, to create shells for investment casting processes [8]. In 1994 Solidscape (Wilton, New Hampshire) invented the InkJet Printing (IJP) and launched the Model Maker [13]: The mechanism consisted of an inkjet printing head that deposited wax layer by layer. Using the same concept, 2 years later, 3D Systems sold the first 3D printer: this was the first mention of the term “3D printers” among industrial machinery [3].

In 1991 Helisys (Torrance, California) invented the *Laminated Object Manufacturing* (LOM) [14]. A roll of plastic material or paper was unrolled, stacked onto the part, and bonded to the previous layers, then, a computer guided laser cut the sheet, and the excess of material was rolled onto the waste roll [1].

In 1992 DTM (Austin, Texas) launched the *Selective Laser Sintering* (SLS) system [14]. The heat of a laser melted powder materials, building layer by layer. A similar machine was patented one year later by Ralf Larson of Larson Brothers co.: The *Electron Beam Melting* (EBM), which was, at the time, the first AM process using a metal powder. In fact, the electron beam was able to weld metallic powder creating a thin layer of solid metal [11].

In 2000 Precision Optical Manufacturing (Auburn Hills, Michigan) introduced the *Direct Metal Deposition* (DMD) technology [8], otherwise called Directed Energy Deposition. Its working principles will be extensively presented in the following chapters.

Starting from the 2000s, AM has been used for production parts and the last two decades are characterized by an exponential growth of AM development [4]. Both the existing technologies and materials keep on evolving while new ones are studied, developed, and commercialized [1].

In 2020 additive manufacturing became very popular to public opinion due to the COVID-19 pandemic because it allowed to produce quickly and cost-effectively specialized surgical instruments and medical devices like valves, masks and everything that may prove to be of primary importance in the fight of the first wave [15]. The idea started in Italy [17] but quickly spread in Europe and USA, so much successfully that AMable, a consortium supported by the European Commission, published an Open Call for solution ideas to fight COVID-19 adopting additive manufacturing [18].

1.2 Generic AM process

The overall process chain is almost the same, regardless from technology adopted and is summarized in **Fig. 1.5**

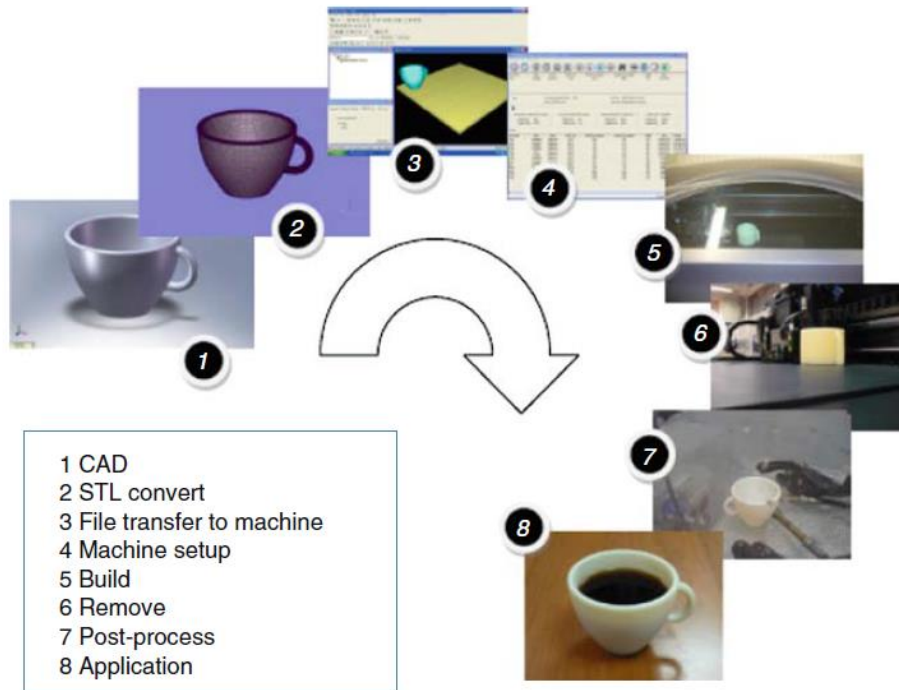


Fig. 1.5 The eight stages of a generic AM process [1]

The process chain consists in the steps required to generate the physical part starting from its concept.

1. Generation of a CAD model

Computer Aided Design (CAD) is basically the first step of every product design process in industry. The output file fully describes the geometry of the part, either in terms of a 3D solid or a set of surfaces [14]. The most common CAD software are SolidWorks, Katia, Autodesk Inventors, Solid Edge, Creo, NX, etc. [19]

2. STL conversion

The CAD model must be converted into acceptable format for the AM machine (STL). Luckily, almost every CAD software can easily convert it. The term STL was derived from the first commercial AM technology: *STereoLithography* [1] and it is also the acronym of "*Standard Triangle Language*" or "*Standard Tessellation Language*" [20]. This file represents external closed surfaces with a triangular mesh, forming the basis for slices calculation. Each triangle is described with its three vertexes and its normal vector direction, indicating where the material is placed.

3. Transfer to AM Machine and STL File Manipulation

During the conversion process, some errors can occur such as gaps between cells, inverted normals or intersections of triangles [14]. Therefore, the first task is to verify that everything in the part is correct. Then, the user can manipulate the part, for example, it is possible to duplicate it to build

more than one part in the same job. It is also possible to linearly scale STL files, to be slightly larger or slightly smaller than the original to consider shrinkage or post-processing coating, typical of some AM methods [1]. The user can set the position within the build chamber and the orientation to optimize the process as well. In fact, additional supports are generally required to hold in place geometries during fabrication [4] and the correct orientation of the part can significantly decrease their number and size. They are usually calculated and added to the part by the software and may be formed of the same material as the part, or a different one. They will be either mechanically removed or dissolved away in secondary operations [1]. Then, the STL model is then sliced into a sequence of parallel planes. This operation is called slicing and it can be performed in two ways. Direct slicing is the simplest method because all the layers have the same thickness, instead, in more sophisticated applications, adaptive slicing is adopted. In this case, the build layer thickness is automatically adjusted to accommodate the surface geometry [4].

4. **Machine setup**

The AM machine must be properly set up prior to the build process. Usually, the build chamber must be cleaned from previous works, then, the raw material is loaded [14]. The energy source level is selected, and the inert gas injection dosed. Finally, the head motion is set up, including scanning speed, hatching distance and layer thickness.

All these parameters are significantly specific to the machine, process, and material. Usually, for advanced machines, the parameters are chosen to optimize final quality, part cost or building time. Unlike classic subtractive technologies, a wrong setup may still produce a part without any serious accidents, although its final quality will probably be unacceptable [1].

5. **Build**

While the previous steps require some human interaction, the build phase is fully automatic. The material deposition and the layer creation can be separate or simultaneous. The machines have a deposition head or a moving platform and they can combine from 3 to up to 5 or even more axis, including roto-tilting mechanisms for particularly complex shapes. As long as no errors are detected (overheating, no more raw material) the machine repeats the process until the build is complete [1].

6. **Removal**

At the end of the building process, the part is removed from the building chamber and a human interaction may be required. For this reason, safety interlocks ensure that the temperatures are sufficiently low and that there are no moving parts [6]. Eventual excess of material in the chamber is cleaned away, and additional supports are removed carefully to avoid possible damages to the part. Also, they can be made of a different material from the part, to facilitate the operation.

7. **Post-Processing**

Unfortunately, only few AM processes build a ready-for-use part: most of them require a significant amount of post-processing [5]. This step is strongly application specific too, as it depends on output accuracy and material properties. Post-processing can be a simple clean up, manual sandpapering, machine polishing, priming, and painting or a more complex operation, such as infiltration or surface coating application to strengthen the final product. Heat treatments or post-curing can be required too [14].

8. **Application:** when all requirements are satisfied, the part is finally completed. The AM processes cover a significantly wide field of application, which is constantly increasing [1]: aerospace, automotive, medical and dental, jewellery, architectural, design and furniture, fashion, food industry, filters and lattice structures, hinges and assemblies, heat exchanges with optimized dissipation surface and new opportunities for fluid dynamics.

1.3 Classification of AM processes

Two different methods of classification may be applied to the AM processes: by material class (polymer, metal etc.) or by raw material form (powder, wire etc.). A certain variety of materials can be processed using the AM technologies: polymers, metals, ceramic and even organic materials. Up to now, polymers have been prevalent in the AM landscape due to their easier formability, but metals have been spreading. AM technologies for production of metallic parts are reported in **Table 1.1**. Powder Bed Fusion (PBF) and Directed Energy Deposition (DED) are the predominant ones and will be exposed in the following dedicated paragraphs.

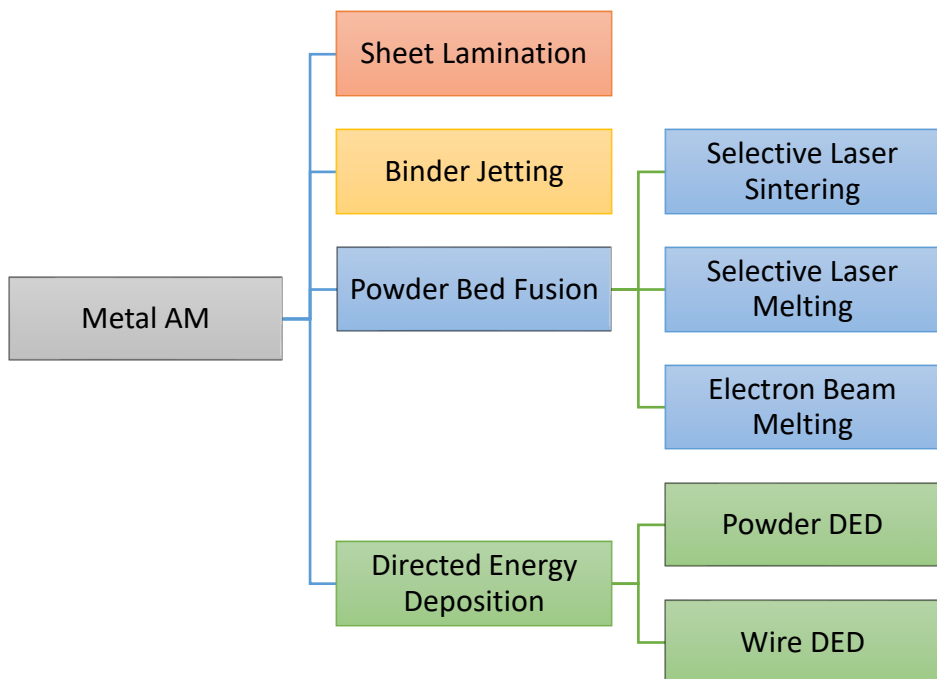


Table 1.1 Metal AM processes

1.3.1 Powder Bed Fusion

In PBF techniques, the object is built on a lowering platform, layer after layer, by an energy source directed on a powder bed. The working principle is depicted in **Fig. 1.6**. A layer of powder is deposited from the delivery system to the fabrication bed by a roller or a recoating blade, then the energy source selectively melts (or sinters) a part of the layer, the platform moves downwards, and the sequence is repeated until the built is completed. The powder bed is usually pre-heated to achieve better compaction and lower residual internal stresses.

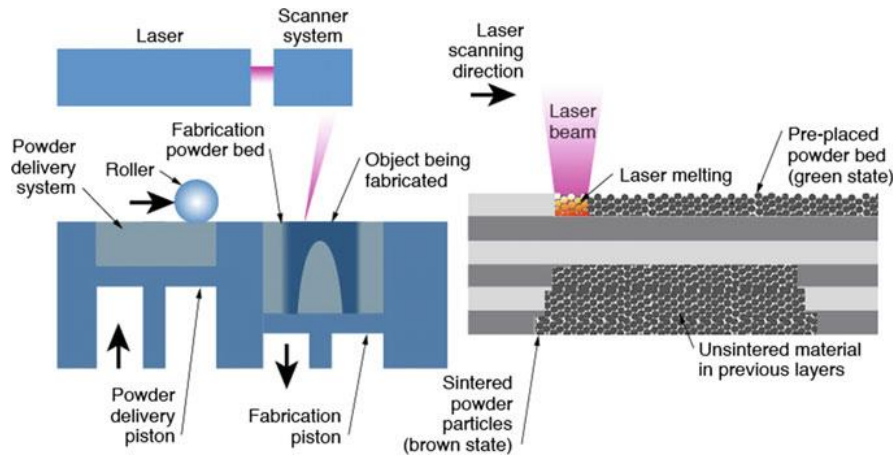


Fig. 1.6 Schematic of Powder Bed Fusion process in Selective Laser Melting configuration [14]

Depending on the energy source type, powder bed processes are divided into electron beam or laser. Laser processes can be further divided into Selective Laser Melting (SLM) and Selective Laser Sintering (SLS), they are essentially the same but SLS gives a lower amount of heat, sintering the metal powder rather than melting it and can be applied also to plastics, glass, and ceramics.

Laser technologies exploit photons directed by a scanner system through a galvanometer mirror, without moving the laser source for higher efficiency. They adopt inert atmosphere of nitrogen or argon to minimize oxidation and porosities, as long as these defects are typically responsible for lower mechanical performances.

Instead, Electron Beam Melting (EBM) uses a thermionic emission gun [3] which emits electrons from a tungsten filament. The environment is a vacuum chamber (high vacuum, 10^{-5} Pa), which makes easier to keep very low oxygen levels. First, the beam preheats the layer and then melts it using a 70-250 μm layer thickness. The high energy of electrons permits a high melting capacity. The beam is deflected by electromagnetic coils, providing a very fast and accurate control resulting in higher productivity than laser processes. EBM also produces lower thermal stresses, but the surface finish is poorer due to larger particle sizes being used.

1.3.2 Directed Energy Deposition

The principle behind DED technique resembles robotic welding and laser cladding (i.e., bonding together two different metallic parts) technologies. Depending on the manufacturer, DED machines sharing the same general approach are indicated by an extreme variety of denominations: 3D Laser Cladding, Directed Light Fabrication, Direct Metal Deposition, Laser Based Metal Deposition, LaserCast, Laser Consolidation, Laser Direct Casting, Laser Freedom Fabrication, LasForm, Laser Engineered Net Shaping etc. [1].

DED creates part by melting and depositing material at the same time, from thin wire or powder feedstock and the focused heat source can be an electron beam or a laser (**Fig. 1.7**).

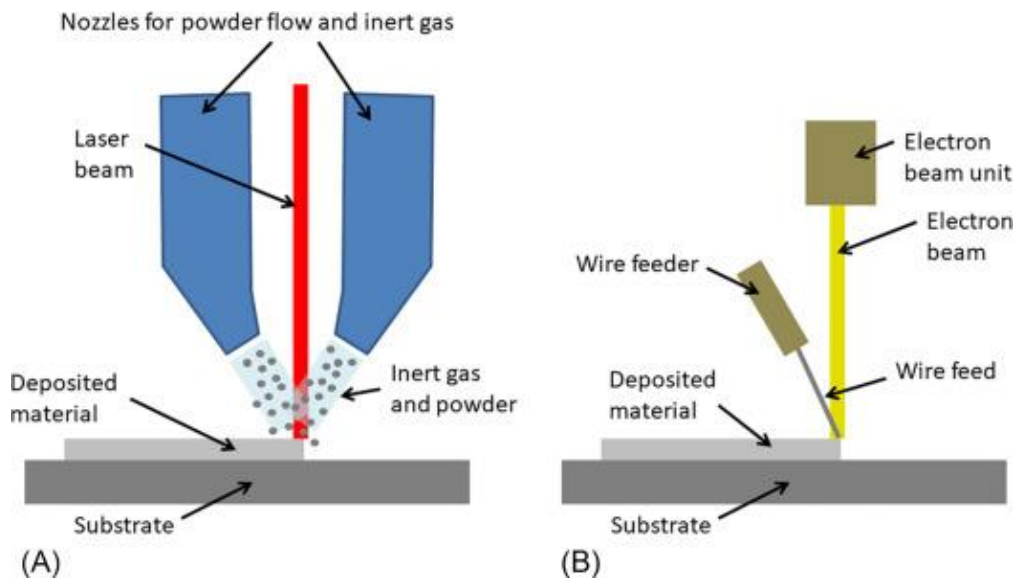


Fig. 1.7 DED configurations: (a) laser beam and powder feedstock and (b) electron beam and wire [21]

Wire feedstock implies a deposition efficiency close to 100%, as approximately all the material used is melted and deposited onto the substrate [21]. Powder, instead, is a more versatile feedstock, it allows to build more complex objects, especially if they have thick and thin regions [1]. Electron beam systems require a vacuum chamber and do not have significant oxidation issues [21]. Laser systems, instead, require some methods to keep oxidation under control that will be exposed in the following pages. The most common configuration is laser (L-DED) using powder feedstock [14] and so the following considerations will refer to this one in particular.

During the process, the laser melts a small point of the substrate, or previous layer, producing the so-called melt pool, highlighted in **Fig. 1.8**. Its dimensions depend on many factors such as the material, laser characteristics and other process parameters. As powder is deposited into the melt pool, it melts and solidifies as soon as the laser beam moves away, creating a thin track. Given the short duration of the melting process, the high cooling rates (1000-5000 K/s) typically generated, produce large thermal gradients and non-equilibrium grain structures impossible to obtain via traditional processes like casting. Neighbour tracks are overlapped, typically 25% of their width, creating a layer. This results in re-melting of the previously deposited material.

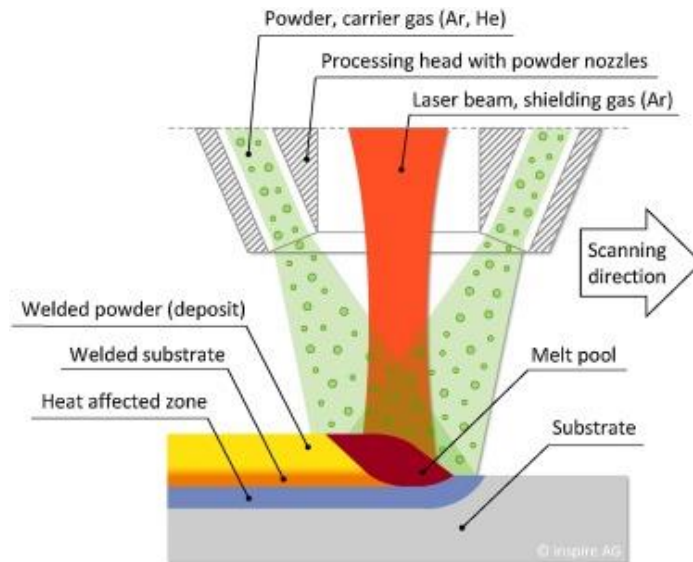


Fig. 1.8 Melt pool in DED [22]

The deposition head can be mounted on a robotic arm [23],[24] or on a classic CNC machine from 3 up to 5 axes [25]. Typically, the object remains in a fixed position but, in case of particularly complex geometries, also the substrate holder can translate, rotate, or tilt, increasing the number of degrees of freedom [25]. Moreover, the beam does not need to be strictly perpendicular to the platform. Within certain angles, the oblique deposition is equally effective thanks to the high velocity of particles [1] (**Fig. 1.9**).



Fig. 1.9 An example of oblique deposition [26]

Powder particles are transported and ejected through the nozzles by an inert gas carrier, such as nitrogen or argon. Different nozzle configurations exist (Fig. 1.10), it can be a single lateral one, 3 or 4 nozzles coaxial to laser beam or a continuous ring, creating a conical nozzle.

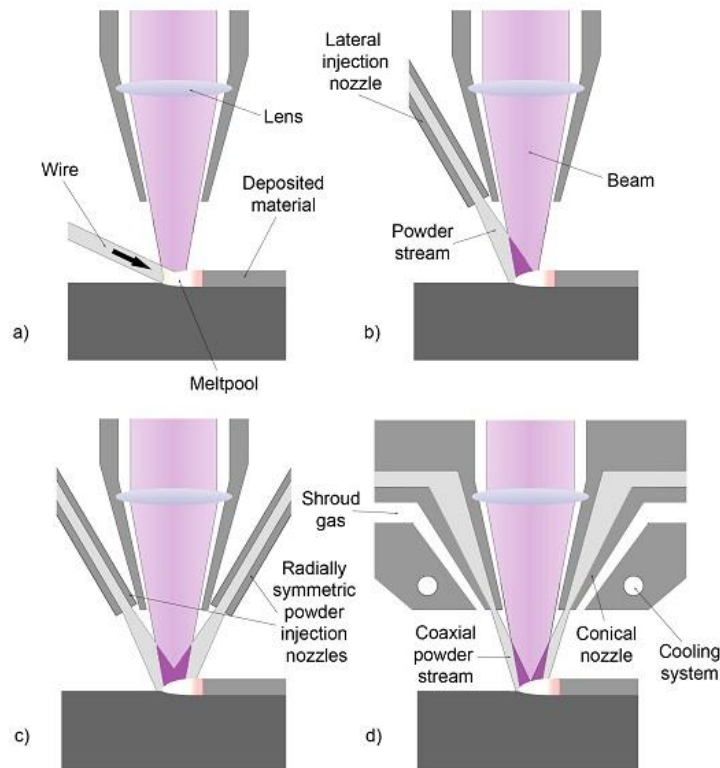


Fig. 1.10 Different nozzle configurations. a) wire, b) single lateral nozzle, c) radially symmetric nozzles and d) conical nozzle. [27]

The 4 nozzles configuration is the most common because it is a good compromise between quality outcome and simplicity of construction [1] (Fig. 1.11).



Fig. 1.11 Deposition head with 4 powder nozzles configuration adopted by Prima Additive [25]

DED technology has some unique characteristics in the AM landscape: it is used to build new parts onto a flat metal plate but also to repair, coat and add features to existing components. DED, in fact, does not require a powder filled chamber, so dealing with much greater objects than in other AM techniques is possible. Moreover, technological development makes possible to adopt different material within the same object [21], avoiding cross contamination problems, almost inevitable in PBF. This technique is also known as Gradient Metal Alloys [28]. Functionally graded materials can be built controlling the composition in each

point of the component, allowing to strategically vary its physical and the mechanical properties. However, this technology is used only in extremely advanced applications.

As previously mentioned, in order to minimize oxidation phenomena and delamination problems, the atmosphere around the melt pool can be controlled in two different ways with inert gas, typically nitrogen or argon. The whole building chamber can be filled with the gas, like in the PBF, or the shielding gas solution can be adopted. In this latter case, a gas flow comes from dedicated nozzles in the deposition head and creates a local protection around the melt pool, this method can be adopted when very large components are processed. Aversa et al. [29] observed that 316L samples produced in a controlled build chamber atmosphere had finer and fewer oxides than the ones produced with the shielding gas method. On the other hand, the latter method is also suitable in case of particularly large parts that might not suit the building chamber.

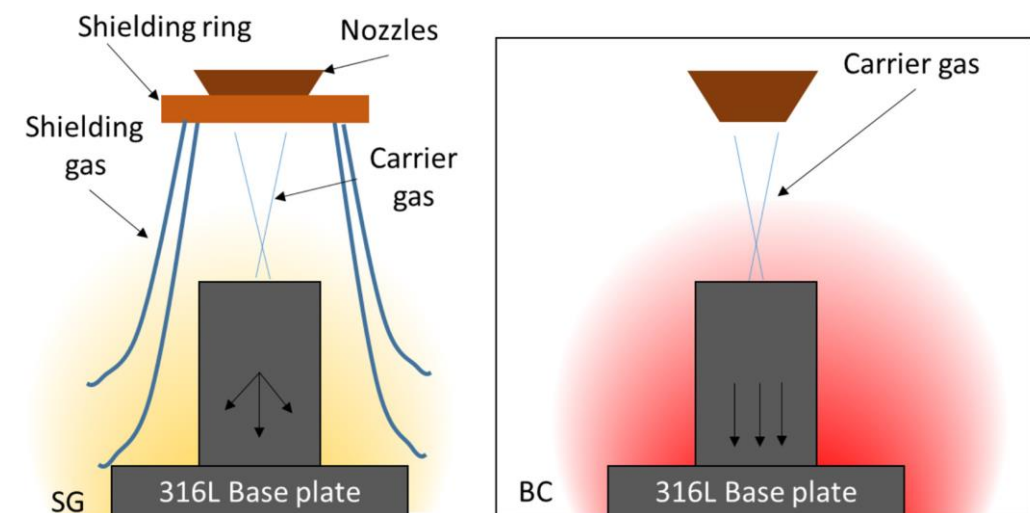


Fig. 1.12 Scheme of the different methods to achieve a controlled atmosphere [29]

Generally, the final part has a very high density, and its mechanical properties are usually better than the ones produced with traditional methods. On the other hand, surface finish is quite poor due to the presence of adhered partially molten particles.

DED is a rather new technology and there is a lack of standardization concerning process parameters and machines. The former can be studied and optimized in order to achieve maximum density, quality, mechanical properties, but also cost and working time. These can be classified in main groups: powder feeder, laser, scanning speed and geometrical parameters. The powder feeder controls the amount of powder feedstock injected into the system and it is measured in g/min. The speed of the particles depends on the carrier gas flow rate, which is measured in l/m. Laser-related parameters include laser power and spot diameter. The scanning speed refers to the linear velocity of the head during the deposition of the scans and it is usually measured in mm/min. The geometrical parameters define the characteristics of the deposition in terms of overlapping between single beads. The hatching distance is the distance between the centre of two consecutive scans while the z-step, or Δz , is the increase of head height between two consecutive layers. Δz must be as close as possible to the actual layer thickness. In the end, the scan pattern, also called scanning strategy, identifies the tracks' directions within one layer and how the subsequent layer changes. A large variety of possibilities exists, an example is reported in **Fig. 1.13**.

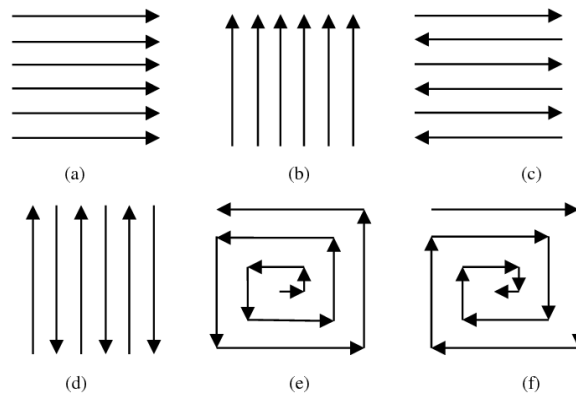


Fig. 1.13 Scanning strategies: a) Parallel horizontal b) parallel vertical c) Anti-parallel horizontal d) Anti-parallel vertical e) Out-Spiral and f) In-Spiral [16]

1.4 Metal Powder Manufacturing

Powder Metallurgy (*PM*) is a set of techniques used to produce a component from metal powder. It was adopted long before the development of additive manufacturing technologies, in fact, classic *PM* has existed since the end of 19th century. In classic *PM*, the metal powder is compressed into the desired shape by a rigid die, roll, or injection mould and then sintered i.e., heated at a temperature well below melting. Instead, in *AM* technologies many layers of powder are stacked and melted [14].

There are several methods to produce metal powder, which strongly influence powder characteristics and, consequently, the properties of the final component. For example, the final component density reflects the presence of the internal porosity of particles and air gaps between them, also chemical composition is important in order to avoid possible undesired phases or defects like oxide films. Also powder flowability has an important role in *AM* because it affects its spread or deposition behaviour. It mainly depends on particles' size and morphology. The preferred shape is spherical because it guarantees higher flowability and better results. Some methods accomplish rather spherical particles, while others require further processing. Different properties can even occur amongst different vendors applying the same technique [30]

The powder production technologies are divided in two main groups: mechanical and physical/chemical methods. Mechanical ones, also called atomization processes, are the most common and are based on the dispersion of a molten metal by a high-pressure jet of gas or liquid. Physical/chemical methods, instead, involve a transformation in chemical composition and structure from raw material.

The gas atomization (**Fig. 1.14a, e**) is the most widespread process, and it is used for a large variety of alloys like Fe, Ni, Co but also Ti and Al [14]. A furnace melts, usually under vacuum, the metal, then the molten metal enters the chamber through nozzles in a thin flow and it is dispersed into small droplets by a high-pressure inert gas that quickly solidifies into spherical (or near to sphere) shape particles. Their size distribution strongly depends on the metal and system used. An inert gas may be used to avoid oxidation of particularly reactive metals like titanium alloys. Water atomization is a similar process, but it employs a high-pressure water jet instead of a gas and it is recommended for unreactive metals such as steels. It is less

expensive but can create oxidation problems and very irregular shape particles due to even higher cooling rate.

Another atomization technique is the plasma atomization (**Fig. 1.14d**), it is suitable for reactive and high melting temperatures metals like Ti. A plasma torch is used to disperse the metal wire feedstock into droplets. Particles are characterized by highly spherical shape, high flowability and high purity powder with low oxygen content.

The mechanical milling (**Fig. 1.14c**), instead, is the simplest method and has been used for a long time to produce metallic powder, it includes compression, collision, and shear processes but it is not suitable for AM applications since the final particles appear extremely irregular shaped. [30]

The most common physical-chemical method is Electrolysis (**Fig. 1.14b**). Due to its intrinsic characteristics, it is applicable only to pure metals and not alloys and so its adoption is rather limited. [30]

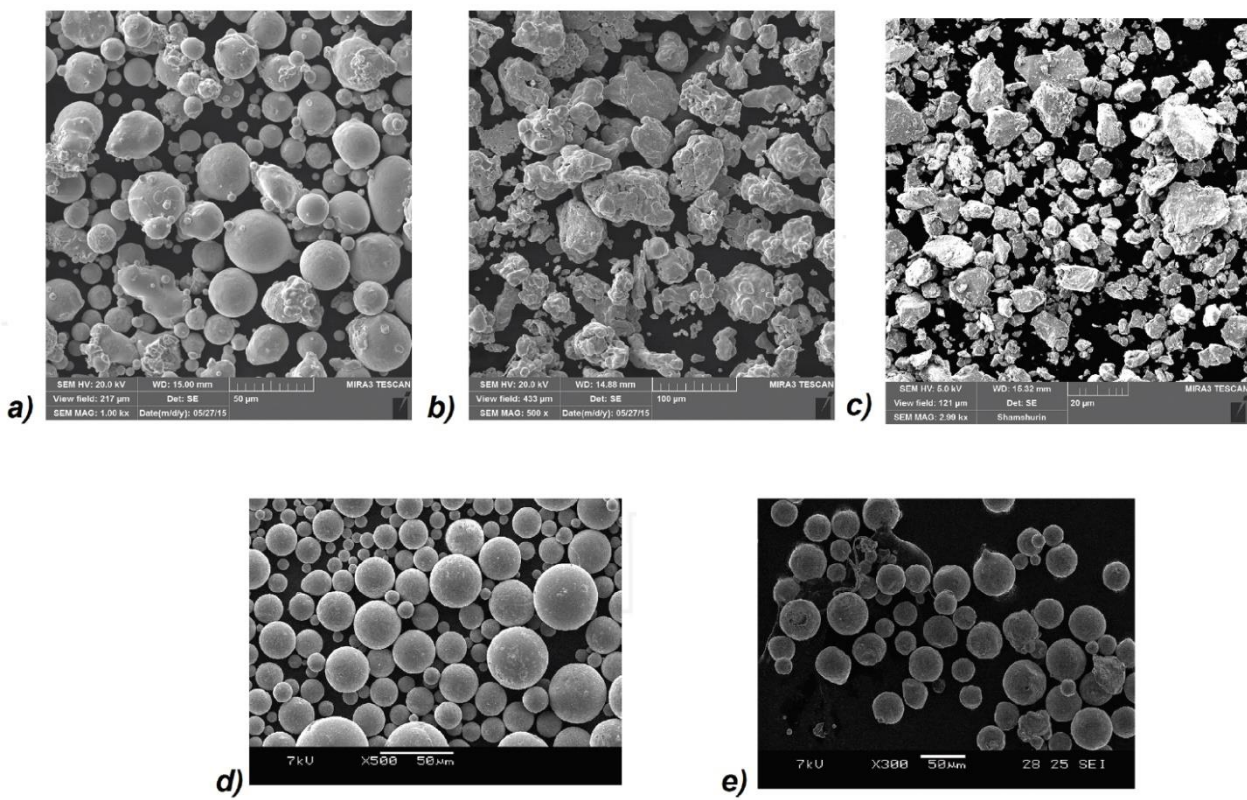


Fig. 1.14 SEM images of different powders: gas atomized In718 (a) and Ti-6Al-4V (e); electrolysed Fe (b); mechanically milled Fe-18Cr-8Ni 12Mn-N (c); plasma atomized Ti-6Al-4V (d). [30]

2 Stainless steel

The steels are the most widespread alloy in the mechanical field. Their peculiar components are iron and carbon but also many other alloying elements can be added such as Mn, Cr, Mo, Ni, Mn, Si while other elements are considered harmful even in low percentages like S, P, O, H, N [32]. Alloying elements modify the Fe-C phase diagram, thus they are generally classified as austenite stabilizer or ferrite stabilizer, depending on the phase field they enhance.

The stainless steels are adopted in aggressive environments due to their high corrosion resistance. According to the EN 10088 standard, steel having a minimum chromium content of 10.5% can be classified as stainless [31] even if, in real applications, a higher percentage is commonly adopted. Chromium has the ability to create an extremely thin layer of oxide (Cr_2O_3) on the surface, protecting the material beneath. This layer is formed spontaneously when the steel is exposed to an oxidizing environment (e.g., air), moreover, it adheres really well and it immediately restores when scratched [32].

Depending on the composition and on the microstructure at room temperature, stainless steels are classified using the Schaeffler's diagram in **Fig. 2.1**

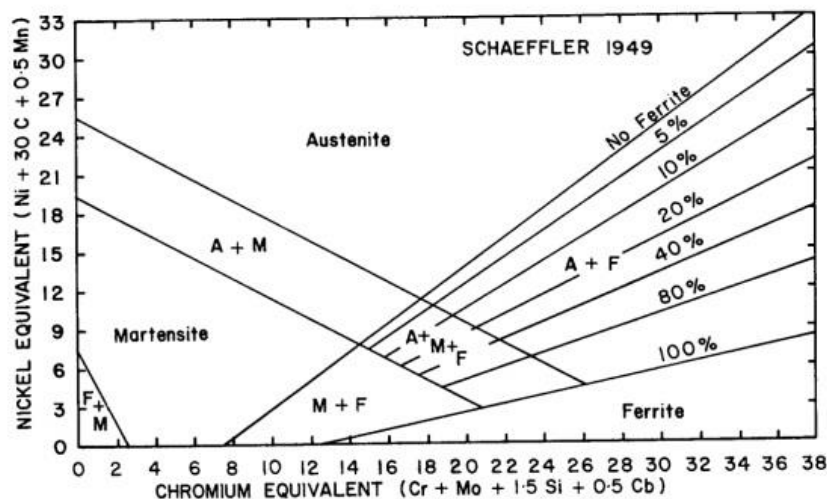


Fig. 2.1 Schaeffler diagram for stainless steels [33]

Four main groups are identified: martensitic, ferritic, austenitic, and duplex.

Martensitic stainless steels have the lowest contents of alloying elements, their mechanical properties depend on the heat treatments adopted, in some case can achieve exceptional ultimate tensile strength, up to 2000 MPa [32]. Due to their high C content, they are the least corrosion resistant among the stainless steels [31]

Ferritic stainless steels have moderate mechanical properties and, depending on the content of Cr and other alloying element, the corrosion resistance ranges from moderate to very good. They have a BCC lattice structure and show ductile-to-brittle transition. [32]

Austenitic stainless steels represent the most widespread group, they have a considerable oxidation and corrosion resistance, they have an FCC lattice structure and so they are amagnetic and do not show ductile-

to-brittle transition. Their mechanical properties are good but cannot be enhanced by heat treatments because they do not have critical points. [32]

Duplex stainless steels have a biphasic structure of austenite and ferrite thanks to the balanced combination of Cr and Ni [31]. They conjugate high mechanical properties and high corrosion resistance.

An additional group, precipitation-hardenable, is not strictly based on microstructure but on the type of heat treatment they usually require [34]. Also called precipitation hardening, or PH, these steels were invented with the aim of enhancing mechanical properties, particularly the fracture toughness, and increasing the corrosion resistance of the classic martensitic stainless steels. They are further classified into subgroups, depending on the microstructure they show, into martensitic, semi-austenitic and austenitic PH stainless steels [34]. The hardening mechanism is achieved through solution annealing and aging heat treatments: alloying elements like copper, aluminium, niobium, and titanium form finely dispersed precipitations, strengthening the crystalline matrix of the steel. The corrosion resistance is ensured by the presence of chromium, nickel, and molybdenum and a very low carbon content, usually lower than 0.1 % [31].

2.1 17-4 PH

The 17-4 PH alloy can assume many different denominations: the aforementioned one is according to ASTM, the EN 10027 designation is X5CrNiCuNb16-4, while the DIN one is 1.4542 and finally the AISI denomination is AISI 630. Due to its composition, reported in **Table 2.1**, it is classified as a martensitic precipitation hardening stainless steel. An example of its microstructure is reported in **Fig. 2.2** The most common heat treatments are solution annealing at 1040°C for 30-60 min and ageing at 480-630 °C for 1-4 hours [31]. Upon them, Cu and Ni precipitate into intermetallic compounds.

Table 2.1 Chemical composition of 17-4 PH stainless steel [31]

Name	% C	%Si	%Mn	%P	%S	%Cr	%Ni	%Mo	%Cu	%Nb
17-4 PH	≤0.07	≤0.70	≤1.50	≤0.040	≤0.015	15.0 ÷ 17.0	3.50 ÷ 5.00	≤0.06	3.00 ÷ 5.00	5 x %C ÷ 0.45

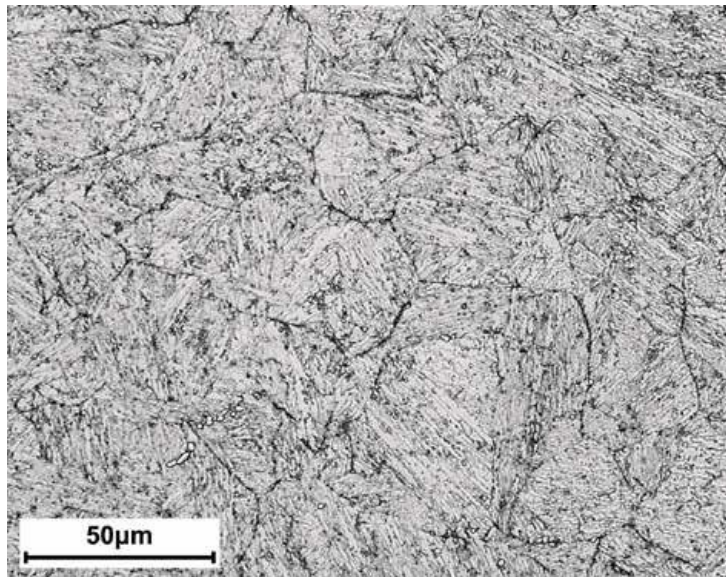


Fig. 2.2 Martensitic microstructure in a 17-4 PH sample after aging treatment at 620°C [31]

17-4 PH shows high mechanical properties and corrosion resistance [35], making it suitable for applications in aerospace, naval, chemical, nuclear, energy and biomedical industries. After thermal treatments, it is possible to achieve a tensile strength of 850-1400 MPa with an elongation between 12% and 25% [31].

2.1.1 AM microstructure

According to Yadollahi et al. [36], precipitation hardening steels are one of the most attracting stainless steels to be processed with AM techniques because of their martensitic/austenitic microstructure and good weldability. 17-4 PH in particular, besides its high mechanical properties and corrosion resistance, has good deposition characteristics [37]. For all these reasons, it is well established in AM applications and studies [23], [24], [35-40].

Generally, the production process strongly influences the characteristics of the metal and, in this case, DED technologies provide cooling rates extremely higher than conventional ones. Thermal history, indeed, defines microstructural features i.e., grain size and morphology, which reflect on mechanical properties consequently [36]. For this reason, in order to achieve the desired mechanical properties, it is crucial to study the influential parameters on microstructure. Studies on different metal alloys used in AM [35], [36] [41-44], show that the resulting solidified microstructure depends on many factors. The most effective are temperature gradient (G) and growth rate (R) i.e., ratio between cooling rate and thermal gradient [41].

$$R = \frac{\text{cooling rate}}{\text{thermal gradient}} = \text{growth rate} \quad (2.1)$$

$$G = \text{temperature gradient at liquid/solid interface} \quad (2.2)$$

Their product $G \times R$ determines the grain size, a higher $G \times R$ results in finer structures while the ratio G/R determines their morphology, as schematized in **Fig. 2.3**

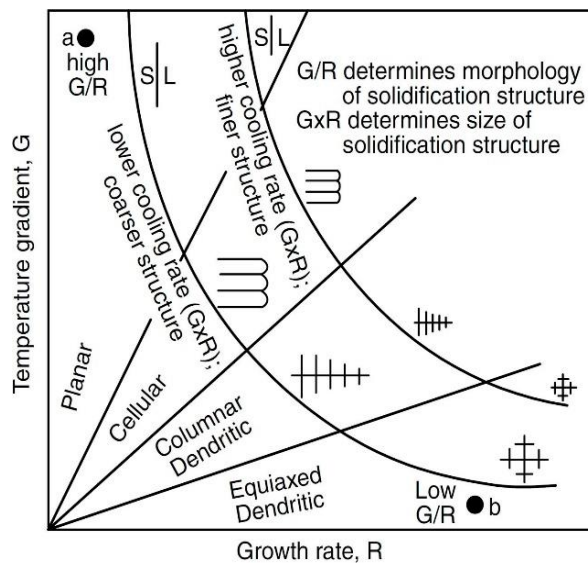


Fig. 2.3 Diagram showing how temperature gradient and growth rate affect morphology and size of the final microstructure [44]

The reason of this phenomenon is that, within the meltpool, different heat transfer mechanisms take place [42]. As showed in **Fig. 2.4**, conduction occurs along the meltpool borders, creating a heat affected zone (HAZ) in the lower layers. In the middle of the meltpool, the metal remains liquid for a slightly longer time, enhancing convection. Lateral sides, instead, are in contact with the environment and radiation is predominant.

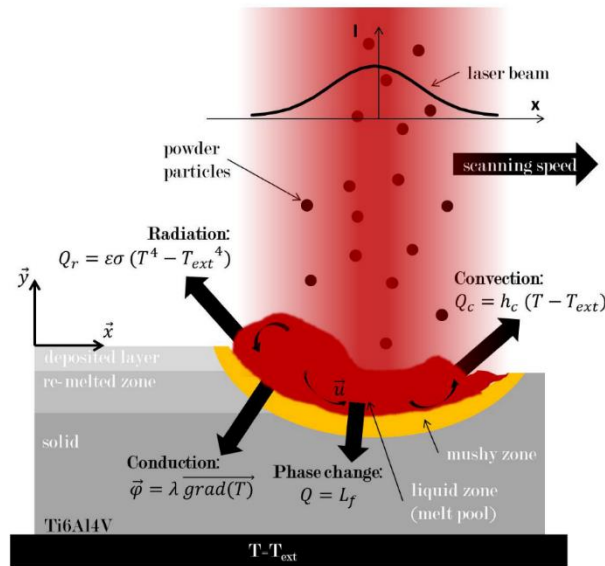


Fig. 2.4 Gaussian distribution of laser beam intensity and different heat transfer mechanisms in the meltpool [43]

These different mechanisms affect G and R parameters and consequently the microstructure: Dendrites with columnar structures (**Fig. 2.5 e**) grow in direction of maximum thermal gradient, perpendicularly to meltpool border towards the centre [35]. In the centre, instead, grains have an equiaxed structure (**Fig. 2.5 d**). Meltpool

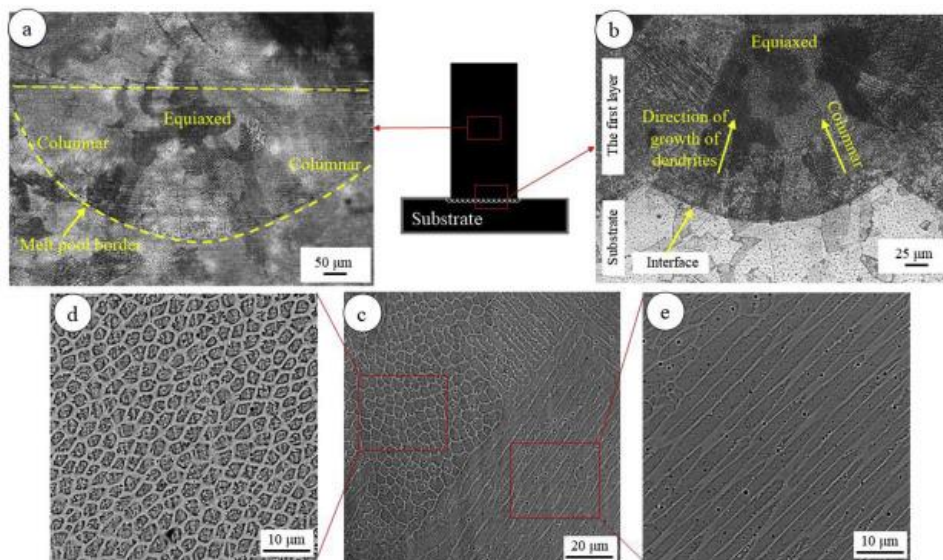


Fig. 2.5 Different structures in melt pools (a), (b), (c): equiaxed (d) and columnar (e) in an AISI 316L sample processed by DED [42]

borders are visible in **Fig. 2.5 a), b)** and it worth observing that they are curved due to gaussian distribution of laser intensity.

The microstructure of the as-built 17-4 PH samples produced by DED is depicted in **Fig. 2.6** and it is composed of martensite and retained austenite. Their percentages depend mainly on the gas process [38]: Argon atmosphere gives a predominantly martensitic microstructure, while in nitrogen atmosphere, due to its austenite stabilizing effect (it can dissolve in melt pool), the retained austenite can reach up to 50% [39].



Fig. 2.6 Equiaxed and columnar grains in a 17-4 PH sample [38]

2.1.2 Mechanical properties

The most common mechanical properties in studies are divided into hardness, usually Vickers hardness (HV) and tensile properties i.e., yield strength (YS), ultimate strength (US) and elongation (ϵ). As-built samples exhibit good properties, but these can be further enhanced by heat treatments, as previously stated. A comparison of them is shown in **Table 2.2**.

Table 2.2 Mechanical properties of 17-4 PH processed by AM before and after heat treatments [35], [36], [40]

Sample type	YS [MPa]	US [MPa]	ϵ [%]	Hardness [HV]
As-built	500-700	950-1050	20-50	250-350
After heat treatments	750-1170	1200-1450	7-20	350-450

The beneficial effects of thermal treatments are manifold: besides the aforementioned precipitation phenomena, retained austenite suppression occurs. Studies showed that the presence of retained austenite has deleterious effects on hardness [37], yield and ultimate tensile strengths but increases elongation [36]. Also, Pavlina et. al [45] demonstrated a certain linear correlation between tensile strength and hardness.

Furthermore, AM processed samples are characterized by a strong anisotropy due to their inhomogeneous microstructure, but the melt pool borders may disappear after heat treatments [38], obtaining a more homogeneous microstructure.

Although the mechanical properties of the 17-4 PH alloy are mainly affected by thermal treatments, studies revealed that also the parameters typical of AM processes affect them.

The Linear Energy Density (LED) is defined as the ratio between laser power and scanning speed. Studies showed that a lower LED has a positive effect both on porosity [23] and microhardness [24], [38]. High LEDs, in fact, promote evaporation and pores formation [37], [40] which have a harmful effect of mechanical properties. Besides, at equal laser powers, high scanning speed values could promote grain refinement, and possibly an increase in microhardness, since there is a shorter interaction-time between the laser and the metal [24].

Not only the LED but also the building direction can affect the tensile properties, as demonstrated in various studies [36], [37], [46]. The built was defined horizontal (or 0°) when the scans were parallel to the tensile direction and vertical (or 90°) in the perpendicular case. As showed in **Fig. 2.7**, scan directions created different structures within the sample, which was characterized by a certain anisotropy. For this reason, horizontal samples had higher tensile properties i.e., YS, US, and ϵ . Yadollahi et al [41] reported that the interfaces between layers created preferential sites for crack formation and propagation because they contained more defects. Oh et al. [37], instead, suggested that heat treatments could homogenize the structure of the samples, reducing their performance discrepancy.

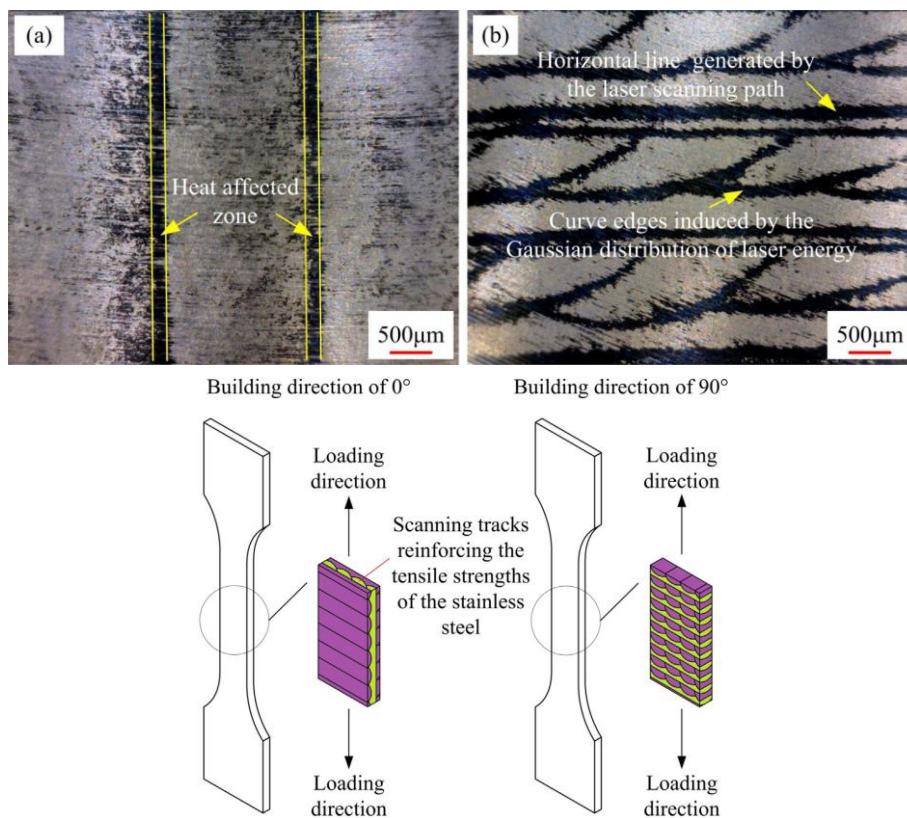


Fig. 2.7 Cross sections and representation of different samples built in the horizontal (a) and in the vertical (b) direction [46]

Mechanical properties depend also on the powder characteristics and powder feed rate: samples built using recycled powder showed a slight degradation of tensile strength and much lower elongation: the reasons could be the more irregular shapes of the particles, that cause an increase in fusion defects, pore number and size [47]. Higher powder feed rate decreases porosity, this effect is more relevant at higher scanning speed [40].

3 Materials and Methods

This chapter describes the experimental procedures of the thesis. First, the characteristics of the DED machine are presented, then, the powder properties are illustrated, as well as the additional characterizations on it. Turning to the main core of the work, the samples are presented and divided into single scan tracks and massive cubes. For each of them, the production, the preparation, and the analysis are detailly explained.

3.1 DED Machine in Prima Additive

The samples were produced in Prima Additive by a DED machine used for experimental researches (**Fig. 3.1**). The machine is a prototype, and it is composed by a complex apparatus, which includes some different commercially available parts.



Fig. 3.1 DED machine prototype in Prima Industrie [48]

The main unit is built on the base of a 3-axes gantry CNC machine and it is controlled through a dedicated software developed by Prima Electro. When the main door is closed, the working chamber is protected from the external environment. This is crucial when a controlled atmosphere is necessary and the working area is filled with inert gas to minimize the oxygen internal content. In this case the glovebox system allows the manipulation of the pieces inside without opening the door. Also, a special dark glass filters the laser light, allowing the operators to see inside the chamber during the building operations safely.

The control panel allows the operator to manage the machine functions. The head can be controlled manually to position it in the correct place prior to the deposition phase. The samples are built using dedicated files, called Part Programs that contain all the process parameters, in particular laser power and head movements. The powder and the gas flow parameters, instead, are controlled through the powder feeder.

The laser source is a commercial Ytterbium fibre laser, with a maximum power of 3 kW (**Fig. 3.2**). The laser beam arrives to the deposition head through an optical fibre cable. The wavelength is 1070 nm, and the laser spot has a diameter of 2mm.



Fig. 3.2 Fibre laser [49]

A chiller is used to cool down the laser, keeping it at a controlled temperature. Another chiller unit is used to cool down the entire optical chain and nozzle, which is close to the process.

The powder feeder is constituted by two hoppers and a control panel (**Fig. 3.3a**). The hoppers have separated circuits so, they can be used to store up to two different materials. The powder feedstock level can be seen through a round glass window at the base of each hopper (**Fig. 3.3b**). Behind it, there is a gear system that

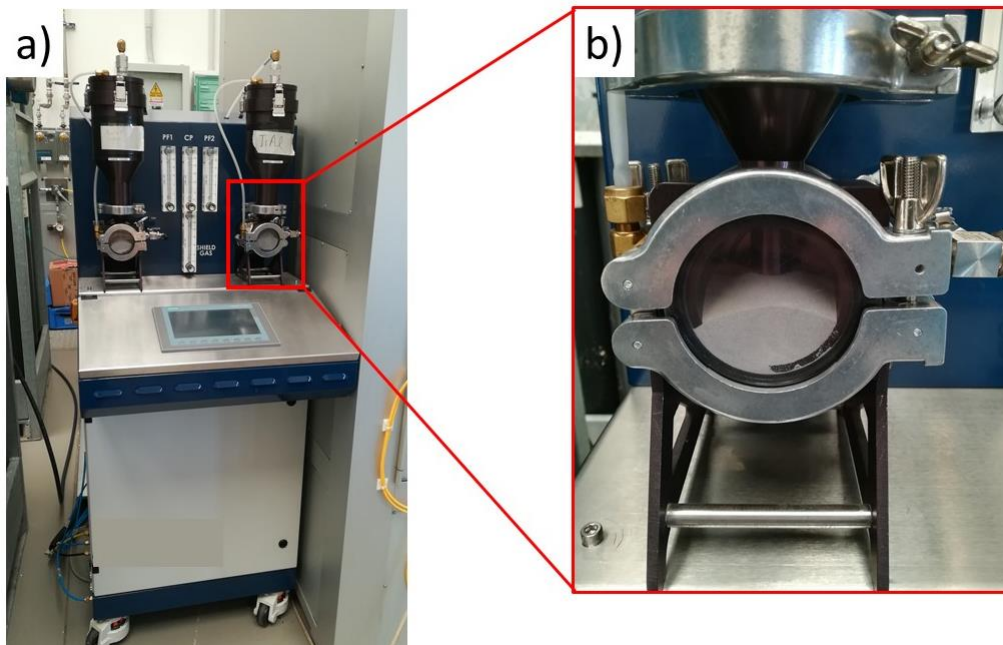


Fig. 3.3 Powder feeder (a) and detail of gear system (b)

doses the powder feed rate, whose rotational speed is set through the control panel. In fact, there is a precise correlation between the main gear RPM and the powder feed rate measured in g/min.

The control panel also manages the flow rates of the gases used as powder transport and as shielding. The inert gases used generally for the direct deposition process are nitrogen and argon. The transport gas is used to push the particles into the pipe system, up to the deposition head.

The deposition head (**Fig. 3.4**) was designed by Prima Additive and the spacer part is produced using the Powder Bed Deposition technique. Its innovative design includes complex internal channels in a slim structure at the same time. The powder is ejected through four holes coaxial to laser beam.



Fig. 3.4 Deposition head [48]

During the deposition, in case of a controlled atmosphere process, an oxygen sensor monitors the oxygen level inside the chamber. In fact, it must be kept at minimum levels to avoid oxidation phenomena.

At the end of the building process, a certain amount of waste powder is present, and a metallic container allows an easier collection of it. However, some residues of powder can be present outside the container, all around the building chamber. For this reason, an industrial vacuum cleaner is used. Different material powders require different bags for further specific recycling treatments or disposal.

3.2 Powder

The 17-4 PH powder used to produce all the samples studied, was produced by an external partner supplier and it was indicated for additive manufacturing applications. The supplier provided a test certificate, in accordance with the standard EN 10204-3.1. The chemical composition is reported **Table 3.1** and the sieve analysis results in **Table 3.2**.

Table 3.1 Powder chemical composition

Element	C	Si	Mn	P	S	Ni	Cr	Mo	Nb	Cu	N	O
Weight composition (%)	0.05	0.61	0.27	0.014	0.004	3.02	15.25	0.04	0.26	3.13	0.09	0.0140

Table 3.2 Particle size distribution

Grain size [μm]	+250	+180	-150	-106	-53	-45
Distribution (%)	0.0	4	84	52	4	1

The powder was further analysed in Politecnico’s laboratories. In particular, it was observed under the Scanning Electron Microscope (SEM), then, the flowability test was carried out and its density was calculated. The SEM adopted was the Phenom XL, produced by the Thermo Fisher Scientific (**Fig. 3.5**). Compared to optical microscopes, SEMs offer a much higher magnification and image resolution, this model offered a 320x – 200.000x magnification and a resolution of 10 nm, according to the specifications provided by the supplier.

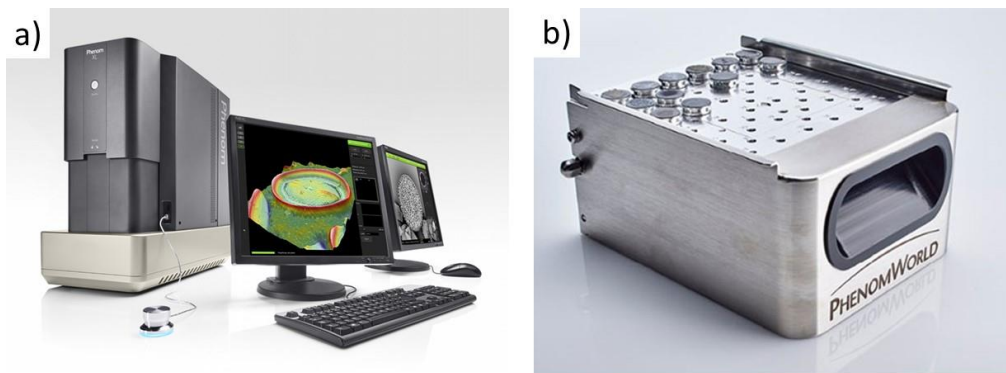


Fig. 3.5 Phenom XL a) and samples holder b) [51]

The SEM analysis was useful not only to check the size and shape of particles, but also to observe possible defects like satellites. All the collected images were further processed through the image-processing software *ImageJ* to calculate the particle size distribution of the powder in the following way: first, the original image was opened (**Fig. 3.6a**), and the scalebar was used to calibrate the measurements. Then, the colours were inverted, a darkness threshold was set and the particles, i.e., the darkest regions, were highlighted (**Fig. 3.6b**). At the end, the area of each particle was measured (**Fig. 3.6c**).

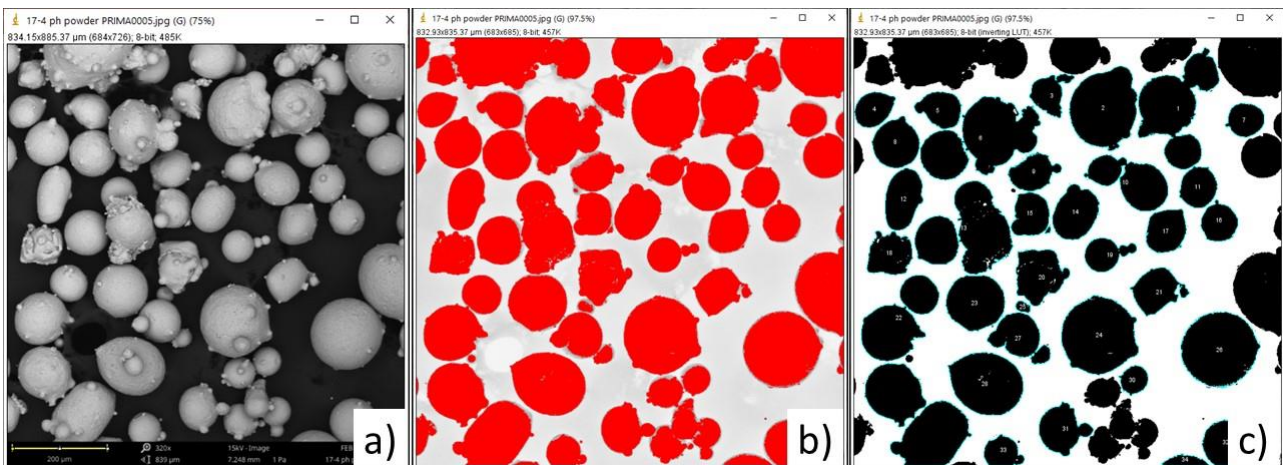


Fig. 3.6 ImageJ steps for particle size analysis: original image (a), inverted colours image with darkest regions highlighted (b), particles counted and measured (c)

The flowability is an important parameter for DED applications and it expresses the ability of a powder to flow. High flowability is usually required to achieve a powder flow as steady as possible from the hopper [14], and hence a stable deposition, but also to avoid system occlusions. The friction between particles depends on their physical characteristics like dimension, shape, and roughness. Generally, large, round, and smooth particles flow faster [30]. Also, humidity can negatively affect flowability, sticking particles together, thus the powder must be kept dry. The flowability test was performed following the ASTM B213 standard [70]. The apparatus is shown in **Fig. 3.7**: it consisted of a conical funnel, called Hall, with a calibrated angle, surface roughness and orifice diameter of 2.54 mm, and a cylindrical brass cup with a capacity of 25 cm³. The bottom of the funnel was placed approximately 25 mm above the cup using a support. So, 50 grams of powder were poured into the Hall funnel, using a finger to block them. When the finger was released, the powder began to flow, if this did not occur, a gentle tap to the funnel was allowed, and the emptying time was measured. In case the tap was ineffective, a funnel with a bigger hole (5.08mm), called Carney, could be adopted. Consistently, the unit of measure of flowability is [s/50g].

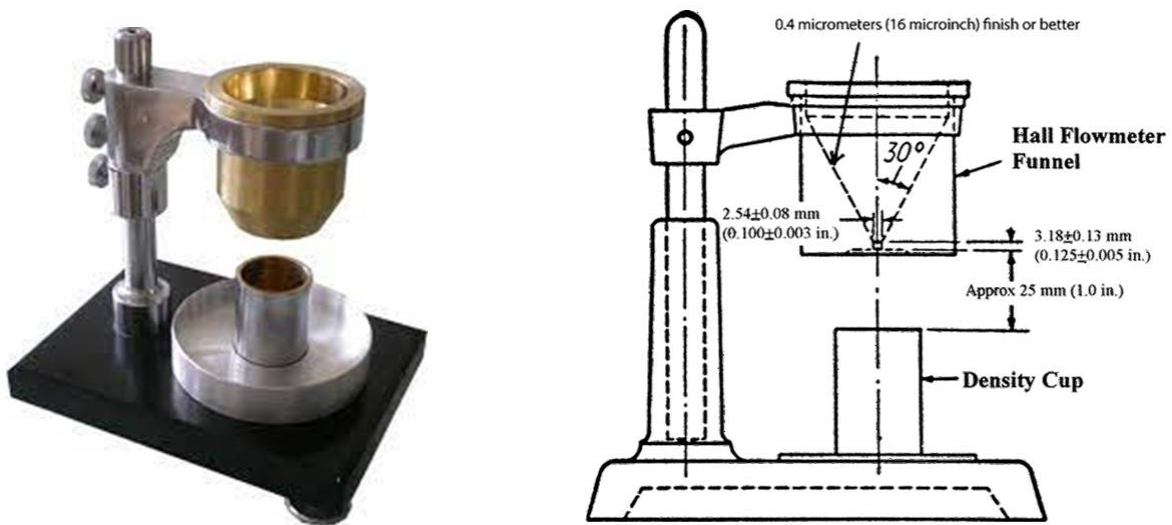


Fig. 3.7 Flowability test apparatus [52]

According to the ASTM B212 standard [71], the density of a powder is reported using two parameters: apparent or bulk density and tap or tapped density. The standard defines how to calculate them: the apparent one was obtained filling up to the edge the aforementioned cup with the nominal capacity of 25 cm³ and measuring the weight. Then, the container was placed onto a shaking plate that compacted the existing powder, so it was filled up to the edge again and weighted. The procedure was repeated until the change between the last two measurements was negligible, the last result was used to obtain the tap density. These two density values were then used to calculate the Hausner ratio and the Compressibility index as follows:

$$\text{Hausner Ratio} = \frac{\rho_{\text{tap}}}{\rho_{\text{apparent}}} \quad (3.1)$$

$$\text{Compressibility Index} = \frac{\rho_{\text{tap}} - \rho_{\text{apparent}}}{\rho_{\text{tap}}} \quad (3.2)$$

As well as the previously mentioned flowability expressed in s/50g, these two parameters are commonly used to judge the quality of a powder in terms of flow. 7 categories of flow exist in the literature and they are shown in **Table 3.3**.

Table 3.3 Flowability characterization [38]

HR	CI	Description of flow
< 1.28	5-15%	Free flowing – excellent flow granules
	12-16%	Free flowing – good flow powders
	8-21%	Fair to passable powdered granule flow
1.28 < HR < 1.57	23-28%	Easy fluidisable powders – poor flow
	28-35%	Cohesive powders – poor flow
>1.57	33-38%	Cohesive powders – very poor flow
	> 40%	Cohesive powder – very very poor flow

3.3 Single Scan Tracks

Depending on the studies carried and their relative objectives, many different types of samples were built. For this thesis project single scan tracks and massive cubes were considered.

Single scan tracks (SST) are the simplest shaped samples: they consist of a linear deposition on the baseplate. The SST of this thesis work are 40 mm long and are illustrated in **Fig. 3.8**.

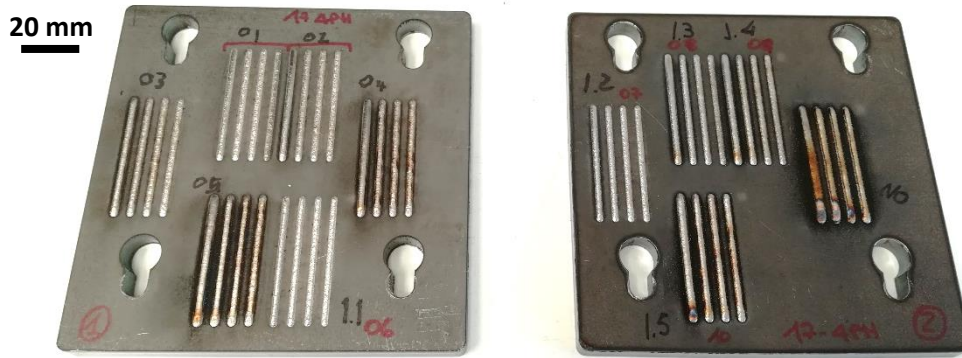


Fig. 3.8 Single Scan Tracks deposited on two baseplates

This type of sample is particularly suitable for preliminary studies and characterizations of materials and processes, allowing to estimate the feasibility window. SST samples do not have geometrical implications because, of course, the multiple meltpool interactions, such as the hatching distance and the z-step, are not present. Secondly, a large number of specimens can be printed changing in a wide range their process parameters. These are summarized in **Table 3.4** and consist of 5 different values of laser power (P), 4 of scanning speed (v) and 2 powder feed rates (F) for a total of 40 different combinations. A nitrogen gas carrier flow was always constant, and no shielding gas was adopted.

According to the trade secret policy of the company, all the process parameter values are a confidential information and for this reason they are expressed as a percentage of the maximum value considered.

Table 3.4 Building parameters adopted in the SST production

Laser power	P	50%, 61%, 72%, 83%, 100%
Scanning speed	v	36%, 57%, 79%, 100%
Powder flow	F	70%, 90%

The Linear Energy Density (LED) is defined as the ratio between the laser power and scanning speed, it is measured in J/mm and it is a commonly adopted as a parameter in single scan tracks studies.

$$LED = \frac{P}{v} \quad (3.3)$$

The analysis on the SSTs allowed to study the dimensions and geometry of the single meltpool, with the aim to carry out a first exclusion on process parameters that did not guarantee satisfactory results and find the correlations between them and the meltpools' geometry. The samples required a certain metallographic preparation, i.e., a series of steps, to obtain a plain, mirror polished and clean surface.

The baseplate was cut around the SSTs using a cutting machine: the plate was held between two clamps, where an abrasive cermet circular blade cut it transversally. During this operation, thermal alterations had to be carefully avoided, so two nozzles supplied a lubricant flow that prevented overheating, blade excessive wear and sparks. Also, the machine was equipped with a fume extractor fan. Then, single scans were cut at around half length, to ensure that a steady state deposition was reached.

Due to the small size of the specimens, the single scan tracks were mounted in resin to facilitate their handling. They were put into a rectangular rubber mould, as shown in **Fig. 3.9**, which was manually filled with an acrylic bicomponent resin. This operation took place under chemical fume hood due to the hazardous vapours released.



Fig. 3.9 Rubber moulds used to mount samples in resin. Keeping trace of the sample ID number is crucial.

After the cutting operations, the surfaces of the samples showed many irregularities and blade scratches, so a grinding process was necessary and the polishing machine *Presi Minitect 233* was used (**Fig. 3.10**).



Fig. 3.10 Polishing machine *Presi Minitect 233*

This machine consisted of a rotating plate where abrasive paper was fixed by a ring. A series of abrasive papers was used, with a progressively finer grit: P400, P800, P2000 and P4000, with a respective grain size of 35, 21.8, 10.3 and 5 μm . A water flow was directed onto the plate to avoid excessive heat and to remove

waste particles. Subsequently, to achieve a finer mirror finish, velvet cloth disks with diamond paste of grain size 3 and then 1 μm were used. Those cloths required an alcohol-based lubricant rather than water.

Then, the samples were carefully washed with water and a drop of liquid soap to remove any impurities from the surface and then gently dried by a compressed air flow. An example of the final result is shown in **Fig. 3.11**.

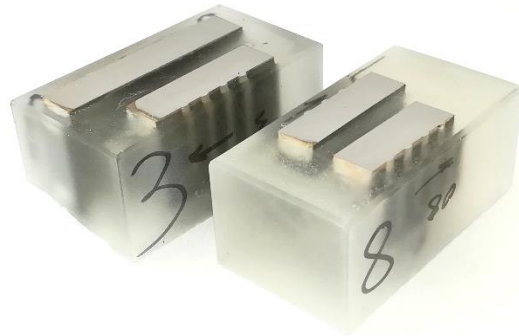


Fig. 3.11 SST mounted in resin and polished

The first analysis was an on-top observation of single scans using a stereomicroscope Leica EZ4W (**Fig. 3.12a**), this could be useful to detect noticeable deposition irregularities or any other issues. Then, images of the cross-sections were taken with a Leica DMI 5000 optical microscope (**Fig. 3.12b**) at 50x magnification.

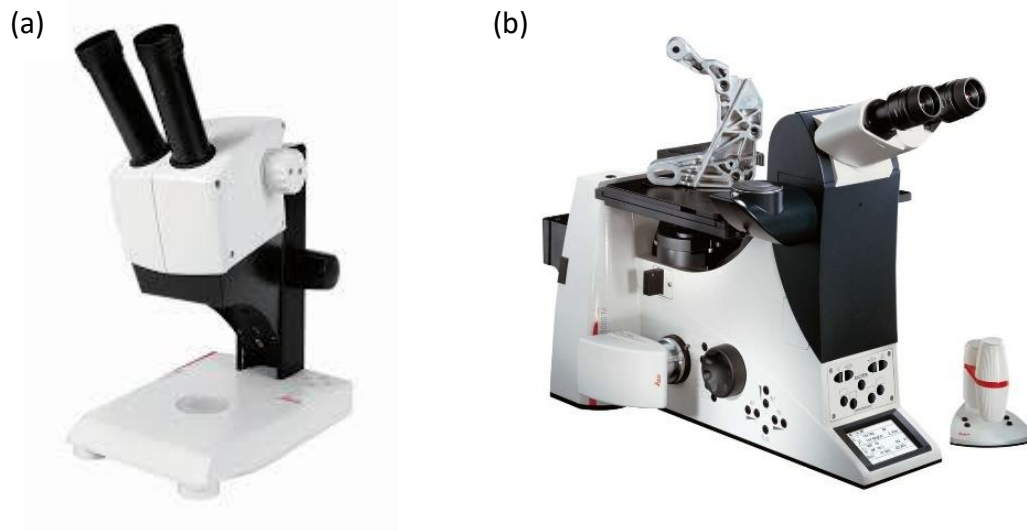


Fig. 3.12 Leica EZ4W stereomicroscope (a) and Leica DMI 5000 optical microscope (b) [53]

The cross-section images allowed to see the melt pools. The geometrical features considered were track width (W), growth (G), and depth (D), as highlighted in **Fig. 3.13**, and they were measured with the image-processing software *ImageJ*.

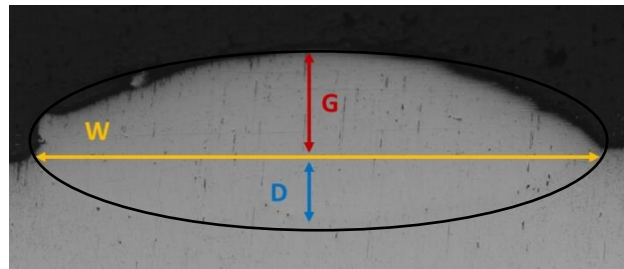


Fig. 3.13 Characteristic features of single scans: Width (W), Growth (G) and Depth (D)

3.4 Massive Cubes

The massive cubes are a type of sample that allows to study how the melt pool interacts one another both horizontally and vertically. Their building requires much more time and material feedstock than the SSTs. Prima Additive chose the process parameters amongst the best ones of the feasibility window found in the SST analysis, in terms of highest productivity. They also considered their past experience.

The massive cubes had theoretical dimensions of 20x20x15 or 20x25x15 mm, the scanning strategy adopted was 0-90°, like as SST deposition, Nitrogen gas carrier flow was always constant, and no shielding gas was adopted.

The parameters adopted for the cubes production are reported in **Table 3.5** and consist of 3 different values of laser power, 4 of scanning speed, 4 powder feeder (powder speed RPM), 3 hatching distance and 3 layer thickness for a total of 7 different combinations.

Table 3.5 Building parameters adopted in massive cubes productions

Laser power	P	50%, 61%, 72%
Scanning speed	v	57%, 64%, 71%, 79%
Powder flow	F	50%, 70%, 80%, 100%
Hatching distance	HD	71%, 93%, 100%
Z step	ΔZ	56%, 78%, 100%

The main evaluation parameter adopted for the analyses of the massive cubes was the Volumetric Energy Density (VED) and it is measured in J/mm^3 .

$$VED = \frac{P}{v \cdot HD \cdot \Delta Z} \quad (3.4)$$

Generally, lower VEDs were associated to higher powder flow rates with the aim of obtaining a rather balanced deposition. In fact, with limited powder flow rates, the amount of the deposited powder was insufficient, leading to a poor outcome.

The cubes, like the SSTs, underwent a certain metallographic preparation process. First of all, the baseplate was cut around the cubes (**Fig. 3.14a**), avoiding the separation between them. Samples were then sectioned using a smaller and more accurate cutting machine *Brillant 220* (**Fig. 3.14b**).

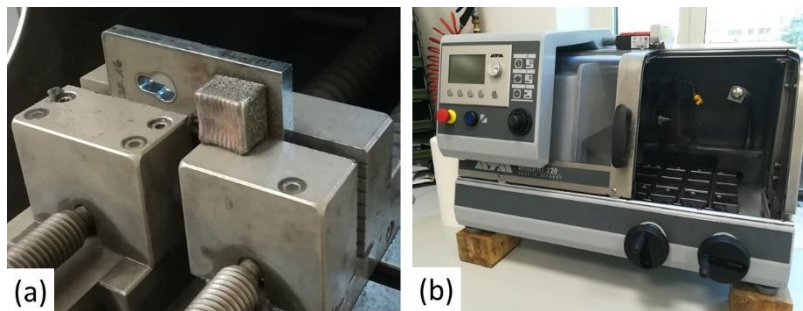


Fig. 3.14 Massive cube ready for baseplate cut (a) and the brilliant 220 cutting machine (b)

All the cubes together are shown in **Fig. 3.15**.

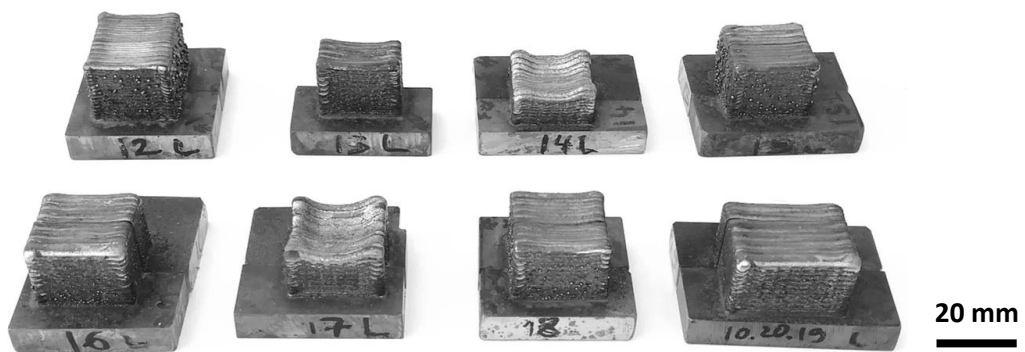


Fig. 3.15 Set of all the 8 cubes produced and analysed

After the cut, the massive cubes were consequently sectioned and polished. In **Fig. 3.16** the two cross-sections of the same cube are shown before and after the polishing operation.



Fig. 3.16 Massive cube sections before and after grinding and polishing operations

The characterization on the massive cubes regarded hardness, porosity, optical and SEM microscope analysis. So, the objective was to identify the best sets of process parameters and also how they influence the cubes' quality.

Hardness

Hardness is a material characteristic expressing its penetration resistance and it is commonly measured by a machine that forces an indenter onto the specimen [32]. According to the standard procedures, the indenter is positioned onto the surface and a load is applied, when it is removed, a mark is visible on the surface. Measuring its dimensions, it is possible to calculate hardness. Different hardness tests exist, such as Vickers, Brinell, Rockwell, Knoop depending on the machine.

In this study, the Vickers hardness, was considered. The instrument used employed a square base pyramidal

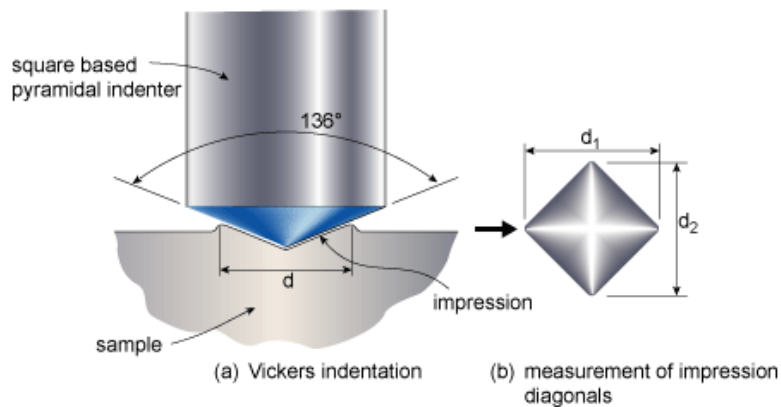


Fig. 3.17 Vickers hardness schematics [54]

indenter made of diamond, with a vertex angle of 136°, as reported in **Fig. 3.17**. It is worth noticing that the square shape guarantees less uncertainty in measurement than, for example, a circle. Impressions were seen through the ocular of the instrument and measured.

Besides the length of impression's diagonals, the parameters defining the Vickers test are the applied load and its time. Finally, the hardness value is given by the formula:

$$HV = 0.1891 \frac{P}{d^2} \quad (3.5)$$

Where P is the applied load in N and d is the mean value of the diagonals in mm.

In this experimental activity, a load of 0.3 Kg was applied for 15 s. For each sample, 3 measurements were performed at the bottom, centre, and top part of the cross section surface, for a total of 9 measurements. The aim was not only to obtain an average value for each sample, but also to investigate if the hardness values changed along the height of the sample.

Porosity

Cubes were placed on the optical microscope at a 100x magnification and a set of 20 images was taken for each of them in an unbiased way. The images were further analysed through ImageJ software, through the passages indicated in **Fig. 3.18**: a darkness threshold was set with the aim of considering the pores but excluding possible scratches, still remaining after the polishing. The percentage of black areas represented the pores percentual porosity.

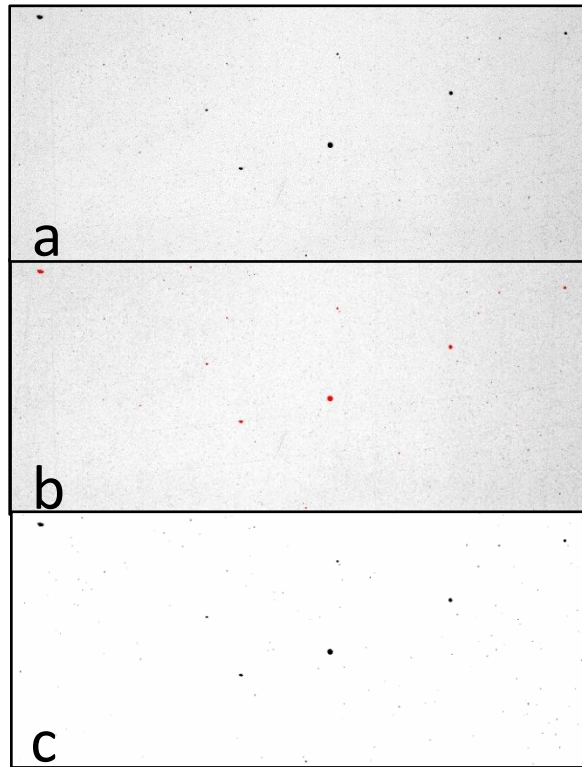


Fig. 3.18 Image elaboration: a) original image. b) darkest region highlighted. c) only black and white image

Furthermore, the software also measured the area and the Feret's diameter of each black dot. The Feret's diameter corresponds to the distance between the two farthest points of a pore, as represented in **Fig. 3.19**.

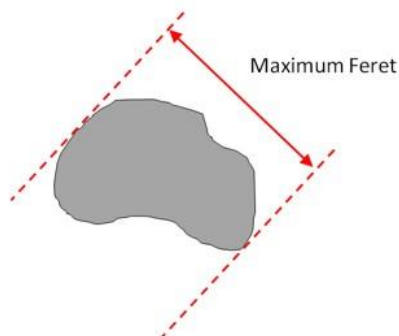


Fig. 3.19 Graphical representation of maximum Feret diameter [33]

This data was useful to make a dimensional distribution analysis of the defects.

SEM observation

A Scanning Electron Microscope (SEM) Phenom XL was used to analyse the samples, in particular to observe fusion defects such as pores, partially molten powder particles or oxides. In case of suspected oxides, the technique Energy Dispersive X-ray Spectrometry (EDS) was adopted: exploiting electron diffraction, it could provide an estimation of chemical composition of the selected spot.

Microstructure

In order to observe the microstructure of the cubes, an acid etching was performed. The acid solution, in fact, selectively attacked grain boundaries, highlighting the microstructure. Marble's reagent was prepared mixing 4 g of copper sulfate (CuSO_4) in 20 mL of hydrochloric acid (HCl) and 20 mL of water, then, always under fume hood, it was gently swept on the sample using a cotton swab and then dried. This technique is called swabbing and it is particularly suitable for strong acid solutions like this one.

Therefore, the samples were again observed under the optical microscope. From each sample, some images were taken at 50x, 100x, 200x, and 500x magnifications to investigate the microstructure and observe defects or particularities.

4 Results and Discussion

4.1 Powder

The scanning electron microscope (SEM) images of a small sample of the powder are collected in **Fig. 4.1**

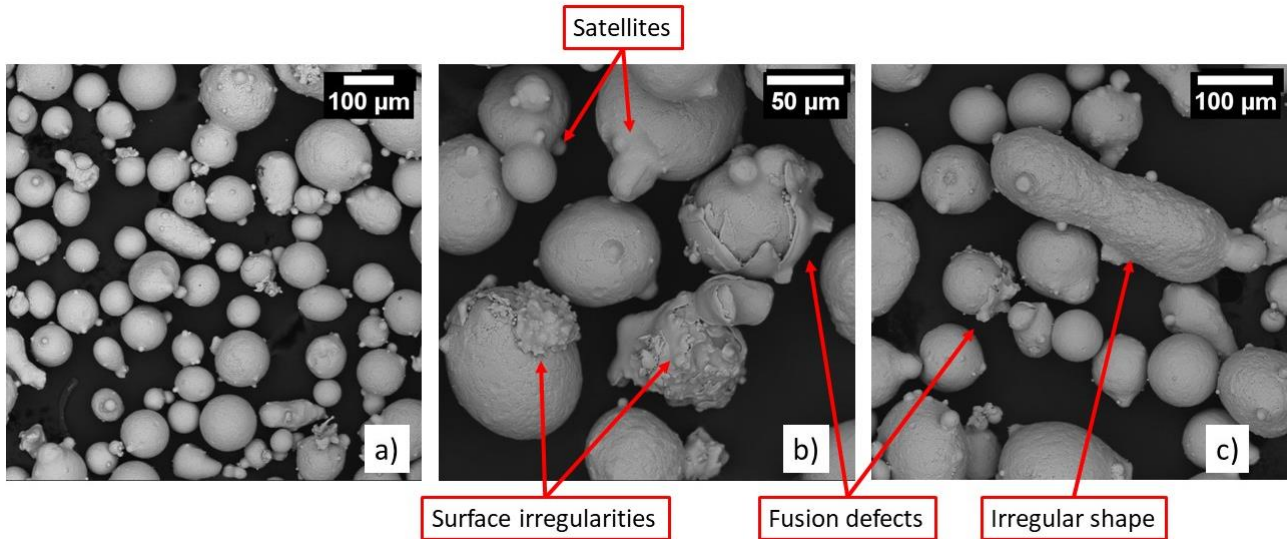


Fig. 4.1 SEM images of powder, general view a) and some defects in particular view b), c)

It was observed that the powder had a considerable amount of defects, the most common ones were satellites of various dimensions. Other defects were elongated shape particles, irregular surfaces, and some not perfectly molten particles. In some other particles, small black dots were visible, and they might be oxides. An example of these suspect oxide is shown in **Fig. 4.2**.

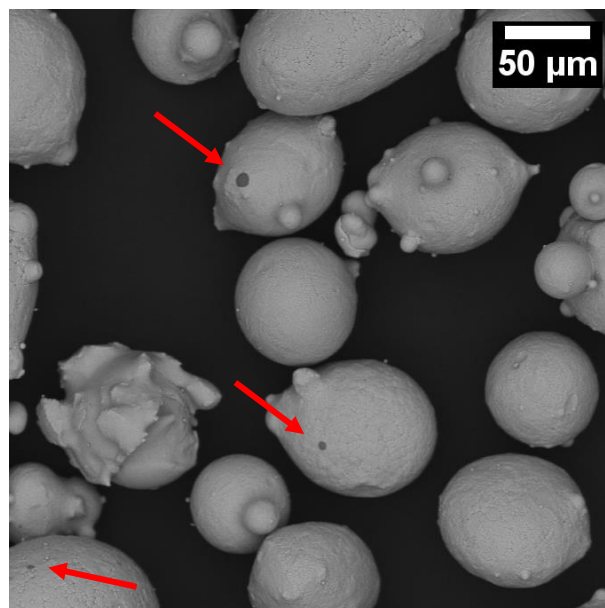


Fig. 4.2 Possible oxides found on powder particles

A total of 22 images was analysed using ImageJ software to measure the diameter of each particle detected. According to the powder supplier's datasheet, only 1% of the particles had a diameter below 45 μm . So, in this analysis, the lower threshold for the diameter was set at 20 μm . In order to calculate the particle size distribution of the powder, 18 diameter classes were defined with an amplitude of 10 μm , up to 200 μm in diameter, i.e., the maximum value found. Then, the particles were sort and put in the corresponding diameter class, obtaining the simple numerical distribution. With the purpose of obtaining a more significant outcome, the area-normalized distribution was calculated. Firstly, every particle was approximated as a circle, and its area A was calculated from the diameter d .

$$A = \pi \cdot \frac{d^2}{4} \quad (4.1)$$

Each i -th class contained n_i elements. The weight of each class wt_i was calculated summing the areas of all its particles.

$$wt_i = \sum_{k=1}^{n_i} A_k \quad (4.2)$$

Finally, the influence of the i -th class (X_i) was calculated as the ratio between the corresponding weight wt_i and the sum of the weights of the 18 classes.

$$X_i = wt_i / (\sum_{h=1}^{18} wt_h) \quad (4.3)$$

As reported in **Table 4.1**, the highest number of particles had a diameter between 40 and 60 μm . Particles above 100 μm diameter were less than 10% of the total and no particles larger than 200 μm in diameter were detected. In the area-normalized distribution, instead, bigger particles had more weight, and in particular, particles above 100 μm covered almost 25% of the total.

Table 4.1 Calculated particle size distribution of the powder

Diameter Range [μm]	Numerical Distribution	Area-normalized Distribution	Diameter Range [μm]	Numerical Distribution	Area-normalized Distribution
20-30	6.7%	1.0%	110-120	1.4%	4.5%
30-40	11.4%	3.5%	120-130	0.7%	2.4%
40-50	20.0%	9.7%	130-140	0.3%	1.4%
50-60	23.0%	16.4%	140-150	0.2%	1.2%
60-70	12.9%	13.0%	150-160	0.3%	1.9%
70-80	8.7%	11.5%	160-170	0.2%	1.4%
80-90	6.1%	10.4%	170-180	0.1%	0.8%
90-100	4.6%	10.0%	180-190	0.3%	2.7%
100-110	2.5%	6.5%	190-200	0.2%	1.9%

The numerical distribution is presented in **Fig. 4.3** adopting two graphical representations: the standard and the cumulative cases. The diameters reported on the horizontal axis indicate the upper limit of each class.

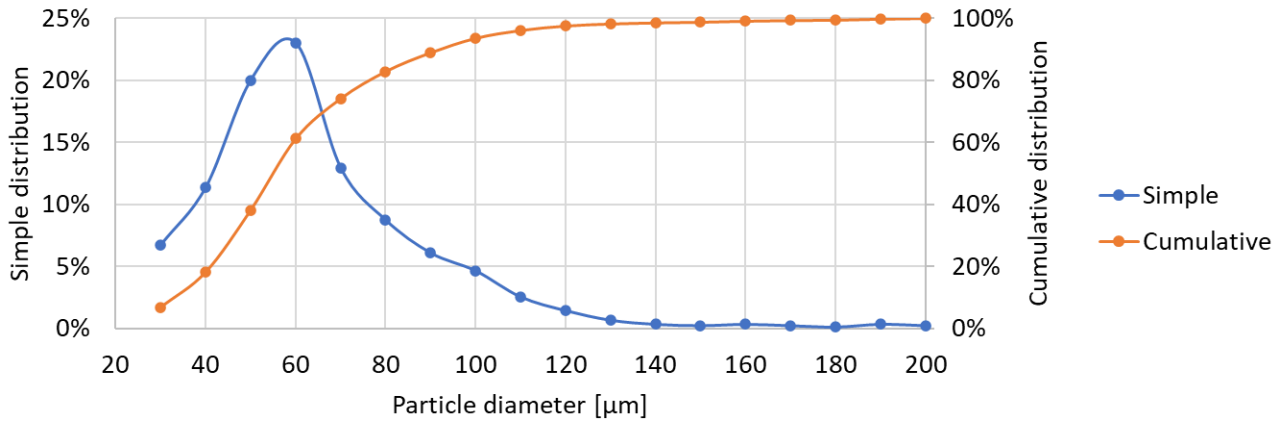


Fig. 4.3 Numerical distributions of particle diameters

Analogously, the area-normalized distributions, are provided in **Fig. 4.4** and, in particular, the cumulative distribution allowed to calculate the characteristic parameters of the powder D_{10} , D_{50} and D_{90} , respectively 46, 75 and 140 μm.

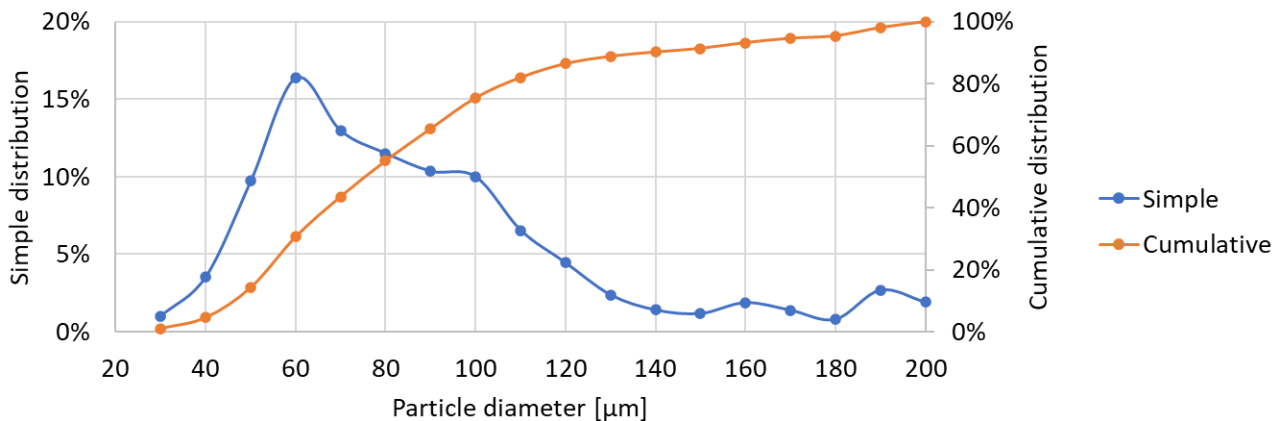


Fig. 4.4 Area-normalized distributions of particle diameters

The area-normalized distribution had a much wider peak, between 50 to 100 μm, and the particles above 120 μm gained much more weight. In fact, in the numerical distribution, they were extremely few.

The area-normalized distribution was considered the most significative and so it was compared to the particle size distribution provided by the supplier (**Table 4.2**). The same class diameters of the supplier’s datasheet were adopted.

Table 4.2 Comparison between the supplier’s datasheet and calculated distribution

Grain size [μm]	+250	+180	-150	-106	-53	-45
Supplier distribution [%]	0	4	84	52	4	1
Calculated cumulative area-normalized distribution [%]	0	5	91	80	20	9

The calculated distribution did not perfectly reflect the supplier's one because the content of smallest particles was overestimated. In particular, this method overestimated the number of particles below 106 μm , this was even more noticeable below 53 μm . However, particles above 250 μm were not found in neither of the two cases. In other words, the powder appeared finer than expected. The reasons of this might be manifold, first of all, the supplier adopted a physical sieve method instead of an image-based one. Then, even at the lowest SEM magnification i.e., 320x, a single image did not contain many particles and a significant amount of them was cut at the edges. This issue affected more likely larger particles. The software, of course, could not consider the cut particles, even if they were cut only for a small portion and this might be the reason of the underestimation of larger particles.

The other analysis on the powder included flowability and density calculations. The flowability test was conducted using the Hall funnel, the measurements were repeated three times and the results are shown in **Table 4.3**. The average value of 15.7 ± 0.2 s/50g was found.

Table 4.3 Flowability test results

Test	Value [s/50g]
1	15.9
2	15.5
3	15.6
Average	15.7
Standard Deviation	0.2

Afterwards, the apparent and the tap densities were measured so, the Hausner Ratio and the Compressibility Index were calculated (**Table 4.4**).

Table 4.4 Density results

Apparent Density [g/cm^3]	4.45
Tap Density [g/cm^3]	4.71
Hausner Ratio	1.06
Compressibility Index	5.5%

According to the previously mentioned **Table 3.3**, the powder placed in the first category with an excellent free flow.

Unlike the particle size distribution, the flowability and the density values were not present on the supplier's datasheet, hence could not be counterchecked.

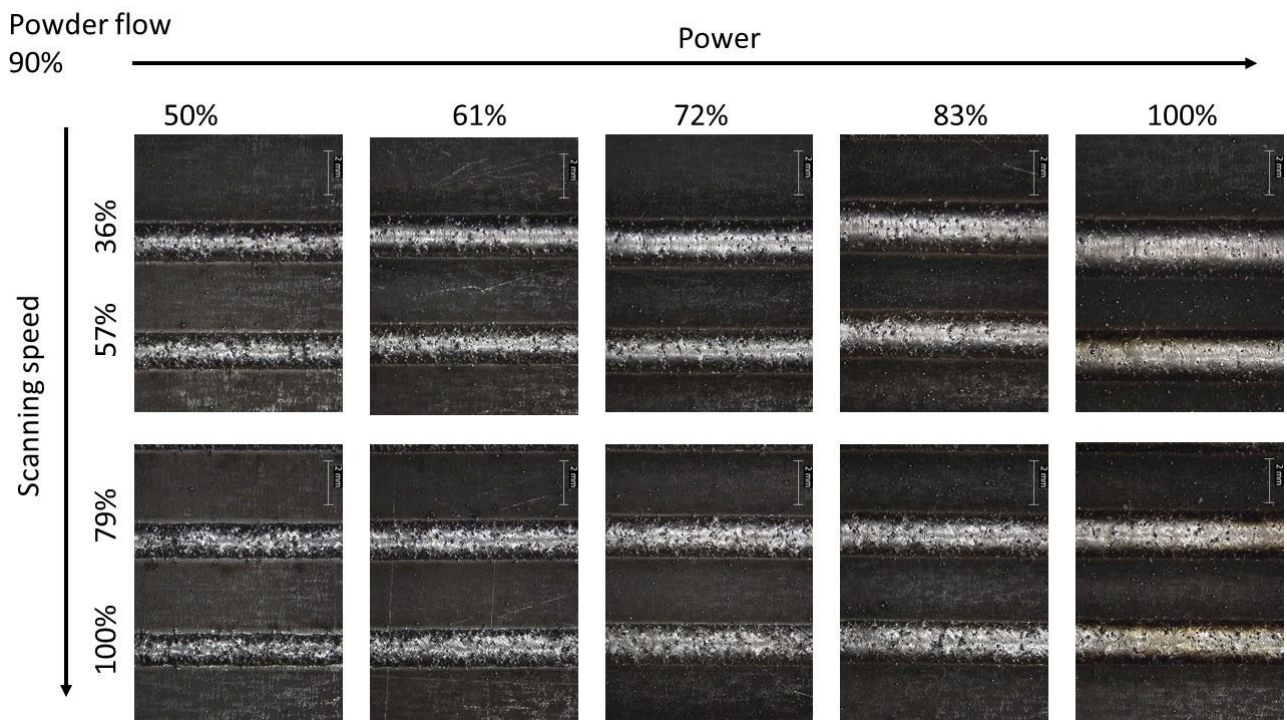
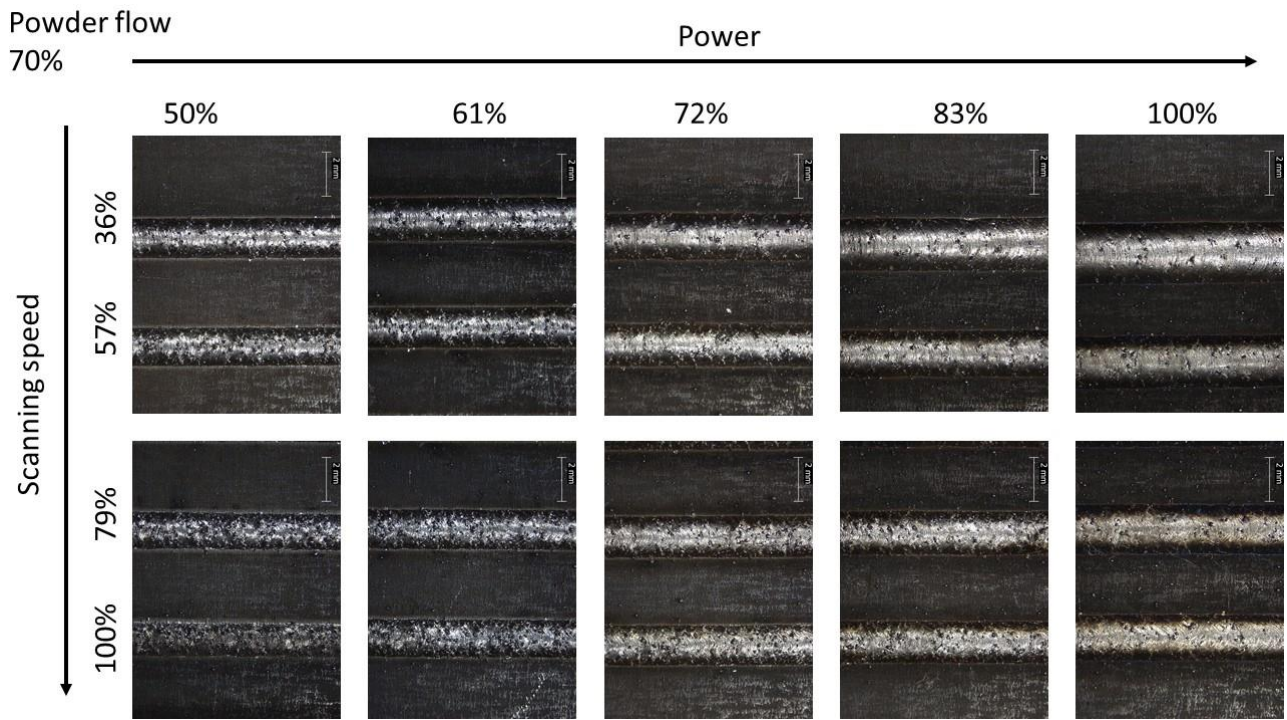
4.2 Single Scan Tracks

The stereomicroscope pictures for the on-top analysis are sort by building parameters in **Fig. 4.5**. The SST were observed at about half of their length to ensure that a steady-state deposition was reached. Most of SST had in the start and the end points a faded deposition, indeed not representative.

Two general trends were found: the SSTs produced with the same scanning speed showed a width increase with laser power. Instead, SSTs with the same power exhibited more adhered particles when the scanning speed increased. These behaviours were observed also by Oh et al. [40] on 17-4 PH samples. In particular, relatively to the latter trend, they stated that the surface roughness and waviness increased with the scanning speed. Beside this, some critical issues were found.

50% power samples exhibited a poor quality, especially at 70% powder feed rate and high scanning speed: depositions had slightly irregular borders and many unmelted particles on them. The same issue, at minor extent, was observed also at 61% power and 100% scanning speed. Samples with the same LEDs but higher powers, instead, did not show this issue, suggesting that the ineffective or incomplete melting was caused by an insufficient laser power rather than an insufficient LED. On the other hand, 100% power samples had much more regular borders and less unmelted particles but showed a slightly colourful surface. The colours ranged from brown and gold to blue and purple and were present both on the samples and on their borders. This is a consequence of a more severe oxidation phenomena and higher thermal shock caused by the higher temperature reached. However, samples with same LEDs but lower powers did not show as much severe oxidations. Eo et al. [72] investigated the effects of laser power on AISI 316L samples produced by DED. They used different laser powers but kept the energy density constant and observed that higher power caused higher oxidation. Moreover, all the samples of this thesis were produced in free air, without any controlled atmosphere, local or total. The adoption of a controlled atmosphere might have reduced the oxygen partial pressure on the meltpool [72] and so the oxidation.

In conclusion, according to this simple qualitative analysis, both scarce power and excessive power should be avoided because they led to some issues, a middle power might be preferable, as suggested in different studies [40], [65] [72], [73].



5 mm

Fig. 4.5 On-top views of single scans, sort by building parameters

The images from the optical microscope of the cross-section are reported in **Fig. 1.2**. Three different colours were used to assess the quality of the deposition in terms of geometry.

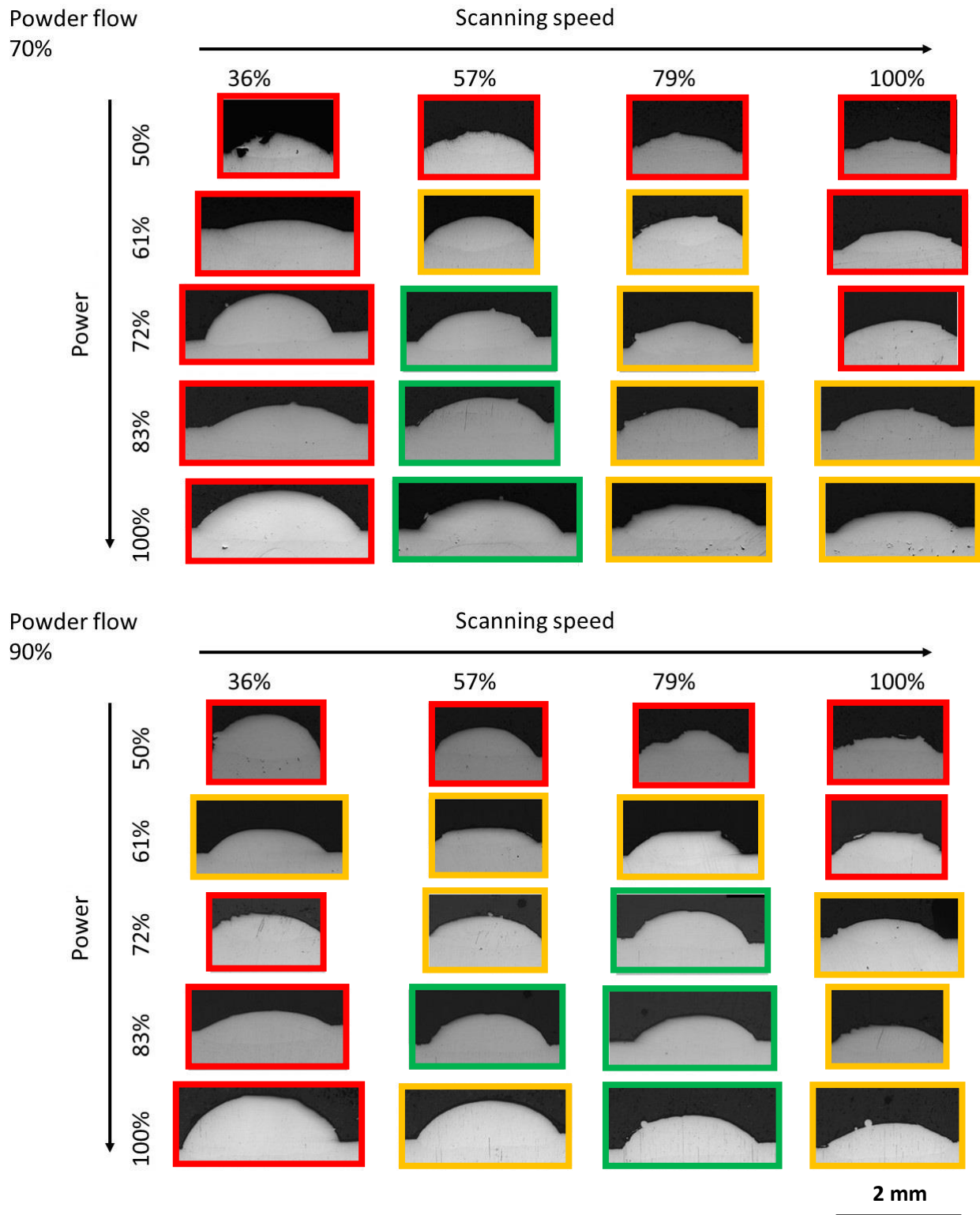


Fig. 4.6 Cross-section views of single scans, sort by building parameters

The adopted criteria for the preliminary classification were based on a comparison among the samples and were the following:

- High acceptability (green). Scans that showed all of these characteristics: regular shape, average growth $0.4 \text{ mm} < G < 0.6 \text{ mm}$, and sufficient penetration $D > 0.15 \text{ mm}$.
- Middle acceptability (orange). Scans that showed a lower growth $0.3 \text{ mm} < G < 0.4 \text{ mm}$ or an excessive one $G > 0.6 \text{ mm}$ but a sufficient penetration $D > 0.15 \text{ mm}$.
- Low acceptability (red). Scans that showed irregular shape, either insufficient growth $G < 0.3 \text{ mm}$, or insufficient penetration $D < 0.15 \text{ mm}$.

At first observation, the most critical samples were the ones built with 50% laser power, for both powder flows, as anticipated in the on-top analysis.

In particular, for 70% powder flow, the sample 1A (**Fig. 4.7**) exhibited very large pores on the left side. Defects like those would surely be unacceptable in a final component.

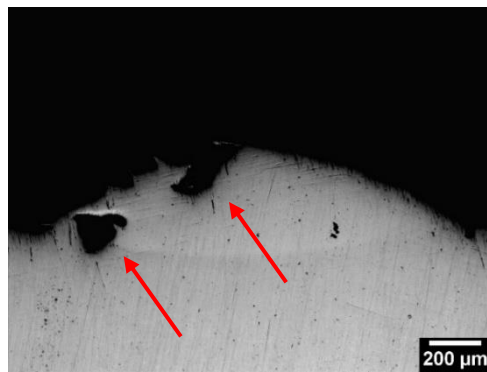


Fig. 4.7 Large porosities on sample 1A

For 90% powder flow, samples 6C and 6D had highly irregular shapes and almost no penetration (**Fig. 4.8**).

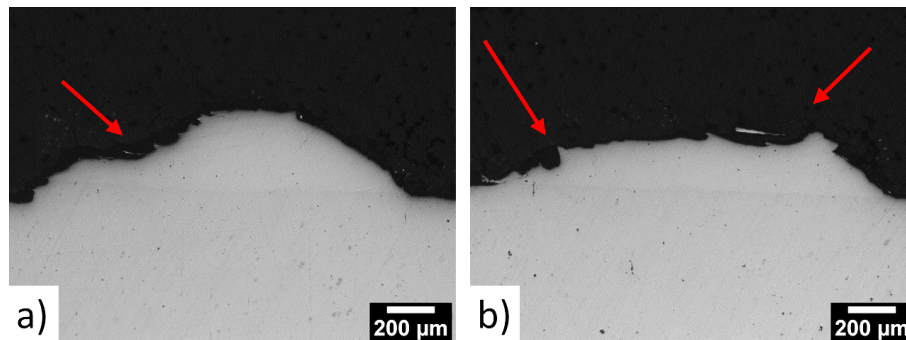


Fig. 4.8 Irregular profiles on samples 6C (a) and 6D (b)

Furthermore, it was observed that almost every sample produced at 100% scanning speed had an insufficient material deposition. Their dimensions were in fact rather smaller than the corresponding ones with the same power.

After a first qualitative analysis of on-top and cross-section views, it was concluded that 50% and 100% laser power and 100% scanning speed parameters brought to critical single scan tracks.

Deeper investigations were carried on the cross-section images, measuring the geometrical features i.e., Width (W), Growth (G) and Depth (D). The results are listed besides the process parameters in **Table 4.5**.

Table 4.5 Single scan tracks results

Sample ID	Power	Scanning Speed	LED	Powder flow	Width [mm]	Growth [mm]	Depth [mm]	G/D	Powder Efficiency
1A	50%	36%	50%	70%	1.441	0.283	0.144	2.0	12%
1B	50%	57%	31%	70%	1.537	0.215	0.159	1.4	16%
1C	50%	79%	23%	70%	1.475	0.245	0.075	3.3	23%
1D	50%	100%	18%	70%	1.353	0.157	0.082	1.9	17%
2A	61%	36%	61%	70%	1.892	0.175	0.249	0.7	10%
2B	61%	57%	38%	70%	1.752	0.391	0.175	2.2	32%
2C	61%	79%	28%	70%	1.72	0.309	0.172	1.8	34%
2D	61%	100%	22%	70%	1.61	0.284	0.09	3.2	38%
3A	72%	36%	72%	70%	2.088	0.694	0.142	4.9	43%
3B	72%	57%	45%	70%	1.885	0.468	0.18	2.6	42%
3C	72%	79%	33%	70%	1.824	0.383	0.175	2.2	45%
3D	72%	100%	26%	70%	1.764	0.273	0.159	1.7	40%
4A	83%	36%	83%	70%	2.368	0.331	0.293	1.1	23%
4B	83%	57%	52%	70%	2.07	0.443	0.211	2.1	43%
4C	83%	79%	38%	70%	1.933	0.369	0.216	1.7	46%
4D	83%	100%	30%	70%	1.87	0.303	0.268	1.1	47%
5A	100%	36%	100%	70%	2.633	0.618	0.204	3.0	48%
5B	100%	57%	63%	70%	2.34	0.522	0.191	2.7	57%
5C	100%	79%	45%	70%	2.184	0.355	0.23	1.5	50%
5D	100%	100%	36%	70%	2.016	0.309	0.2	1.5	51%
6A	50%	36%	50%	90%	1.784	0.627	0.126	5.0	26%
6B	50%	57%	31%	90%	1.654	0.442	0.093	4.8	27%
6C	50%	79%	23%	90%	1.471	0.313	0.153	2.0	23%
6D	50%	100%	18%	90%	1.552	0.196	0.077	2.5	20%
7A	61%	36%	61%	90%	1.941	0.391	0.186	2.1	17%
7B	61%	57%	38%	90%	1.854	0.391	0.205	1.9	27%
7C	61%	79%	28%	90%	1.708	0.347	0.161	2.2	30%
7D	61%	100%	22%	90%	1.695	0.246	0.12	2.1	27%
8A	72%	36%	72%	90%	1.809	0.293	0.188	1.6	12%
8B	72%	57%	45%	90%	1.792	0.36	0.198	1.8	24%
8C	72%	79%	33%	90%	1.943	0.494	0.159	3.1	49%
8D	72%	100%	26%	90%	1.774	0.315	0.175	1.8	36%
9A	83%	36%	83%	90%	2.125	0.282	0.26	1.1	14%
9B	83%	57%	52%	90%	1.941	0.517	0.153	3.4	37%
9C	83%	79%	38%	90%	2.015	0.426	0.175	2.4	44%
9D	83%	100%	30%	90%	1.813	0.309	0.164	1.9	36%
10A	100%	36%	100%	90%	2.591	0.831	0.183	4.5	50%
10B	100%	57%	63%	90%	2.347	0.599	0.192	3.1	52%
10C	100%	79%	45%	90%	2.233	0.522	0.192	2.7	59%
10D	100%	100%	36%	90%	2.065	0.353	0.202	1.7	47%

For each sample, W, G and D were plotted in function of the LED for each of the 5 laser powers (**Fig. 4.9**).

W was between 1.3 and 2.7 mm and, in first approximation, it slightly increased with the powder flow rate. W had the clearest trend: it increased with LED i.e., power increase and scanning speed decrease. However, the trend was less certain at 90% powder flow and 72% power. Also the sample with 50% power, 50% LED and 70% powder flow had an irregular behaviour, but it was due to its irregular shape, previously described in **Fig. 4.7**. High LEDs, so, created a larger meltpool, increasing the width of the scan track. In other words, more powder got effectively melted, enhancing the deposition effectiveness.

G lied between 0.15 and 0.85 mm and most of the values were condensed in the interval 0.2-0.45 mm. Again, a slightly increase with powder flow was observed in first approximation. Its trend, instead, showed a quick increase between 15% and 40% LED and then, in some samples continued to increase, while in others, decreased inverting the trend and. In both width and growth, 90% powder flow samples had a light increase, compared to 70% powder flow ones. It might be concluded that LED promoted the growth until a certain limit value, around 50%-60%. After that, the deposition becomes less effective.

D was the most fluctuating characteristic, it varied between 0.07 and 0.3 and had the least certain trend: generally, D seemed to increase with LED and slightly decrease with powder flow increase. This might be reasonable, because, with the same amount of energy supplied, higher powder flow means more powder to melt, and so, less energy remaining to melt the substrate.

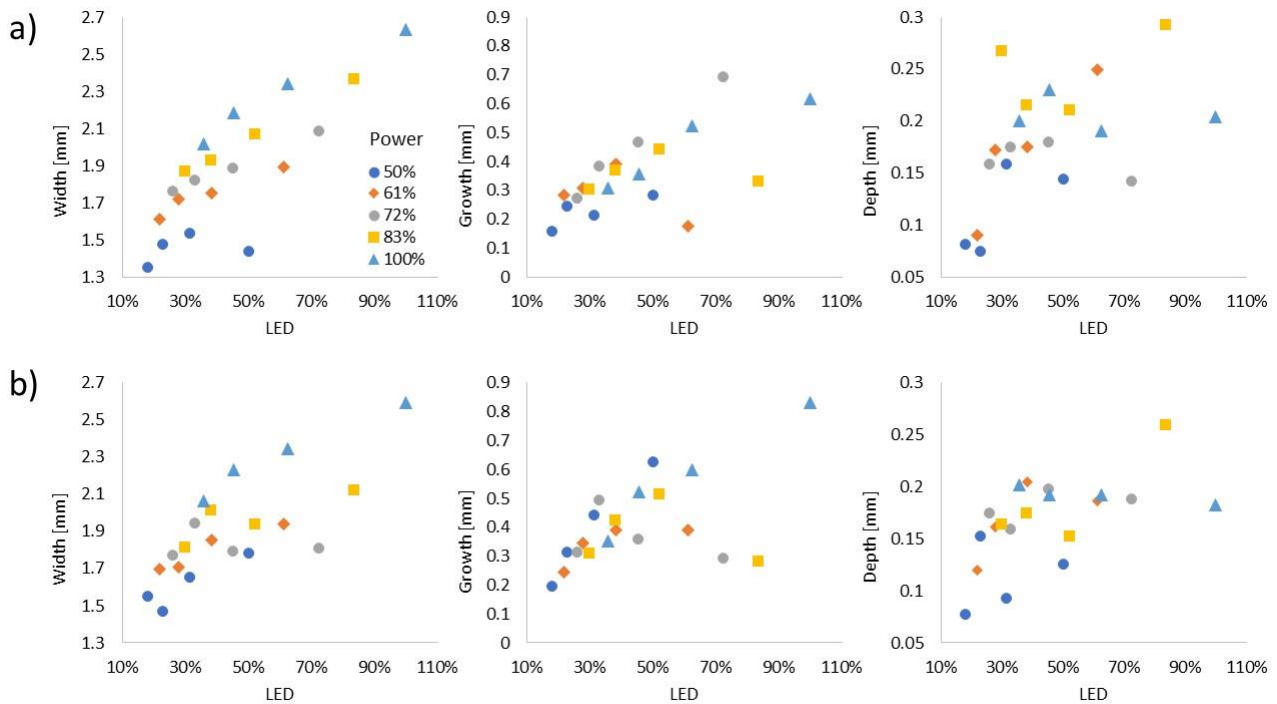


Fig. 4.9 Evaluation of geometrical features for 70% a) and 90% b) powder flow

Some more precise information were searched in the literature. In fact, single scans are a standard type of sample and are typically studied in DED applications.

Ho et al. [40] focused their study on 17-4 PH SSTs produced by DED and suggested that if a higher energy is supplied i.e., higher laser power, the melt pool dimensions increase and so W, G and D. When the scanning

speed decreases, instead, only W and G increase, while D remains almost constant. They also stated that an increase in powder feed rate increases W and G but does not significantly affect D.

Returning to the topic of how energy splits to melt the supplied powder and the substrate, the ratio G/D could be considered. Studies [58], [59] showed that, indeed, G/D is an important parameter to estimate the deposition effectiveness. If it is too low, namely $G/D < 0.5$, not enough new material is deposited and an excess of previous layers material is melted, finally resulting in an irregular shape component with the collapsed top portion. Conversely, if it is too high i.e., $G/D > 2$ the bonding to previous layer is too weak and so delamination and cracks may occur. The optimal range is set at $0.5 < G/D < 1$.

G/D ratio was plotted, again, in function of the LED for each of the 5 laser powers (Fig. 4.10). All the values lied in the range 0.7-5, even if the most of them was between 1-2 and 1.5-2.5, respectively for 70% and 90% powder flow rates. The separated effect of powder flow rates on G and D previously analysed was confirmed here, with their ratio: G/D slightly increases with powder flow rates.

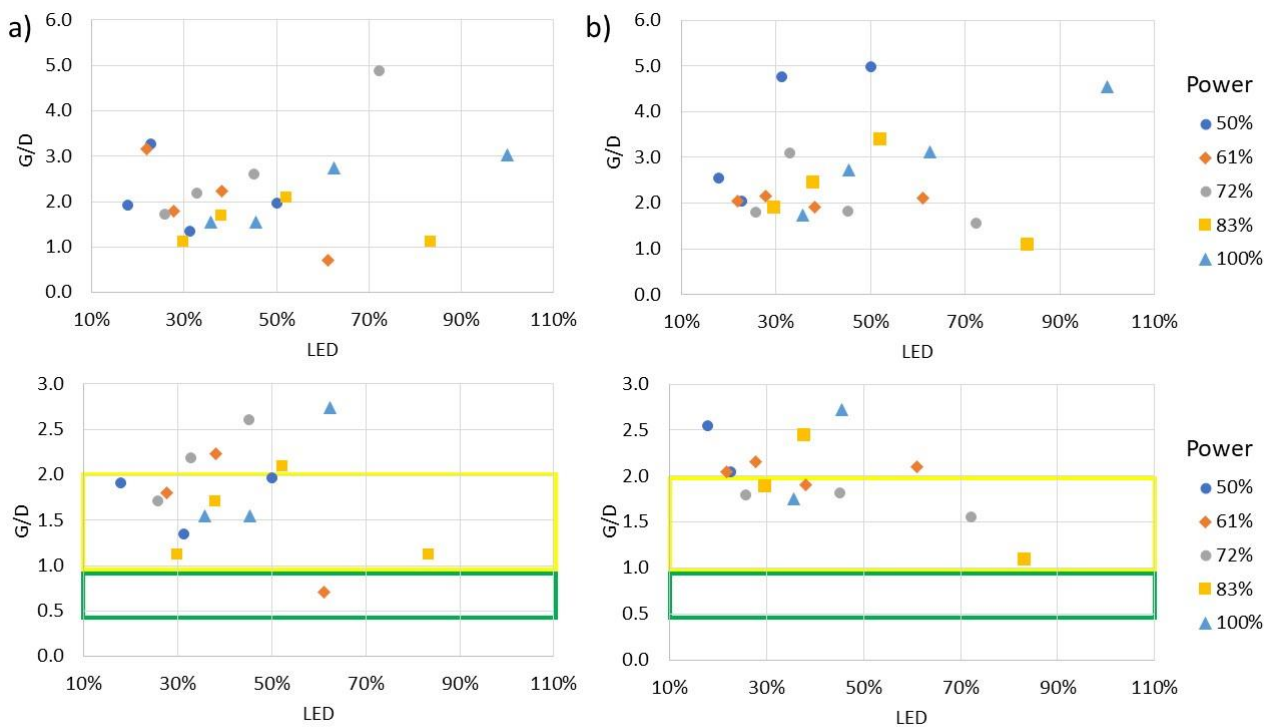


Fig. 4.10 G/D ratios for 70% a) and 90% b) powder flow. The optimal and the acceptable regions are highlighted in green and yellow, respectively

Going into details, only one sample (P 61%, v 36%, F 70%) lied in the aforementioned optimal range: all the others had a higher G/D ratio. In case of 70% powder flow, the majority of the samples lied in the acceptable interval between 1 and 2 but were fewer for 90% powder flow. So, it could be concluded that, under G/D point of view, lower powder flow was preferable.

Another key parameter in single scan study is the powder efficiency [60] which represents the fraction of delivered powder that has actually solidified into the track. Powder feedstock is rather expensive, so it is preferable to obtain the efficiency as high as possible. It is calculated as

$$P_e = \frac{A_g \cdot v \cdot \rho}{F} \quad (4.4)$$

Where ρ is the material density, corresponding to 7.8 g/cm^3 for 17-4 PH, as found in the literature [31]. F is the powder flow rate and A_g is the growth area in mm^2 , calculated approximatively as half ellipse:

$$A_g = \frac{\pi \cdot W \cdot G}{4} \quad (4.5)$$

The results were plotted in function of LED and power, like the previous graphs. P_e lied within a wide interval, from 10% to 60% (**Fig. 4.11**), precisely, the highest value detected was 59% in sample 10C (100% P, 79% v, 90% F). Generally, a power increase led to a strong increase in P_e . Also, P_e was higher at higher scanning speed and the most of 36% v samples were characterized by a considerable drop in P_e , even if it did not happen in 100% power samples. The increase of powder feed rate increased P_e only in the 50% power samples, while it did not have significant effect in 100% power samples and decreased in the others.

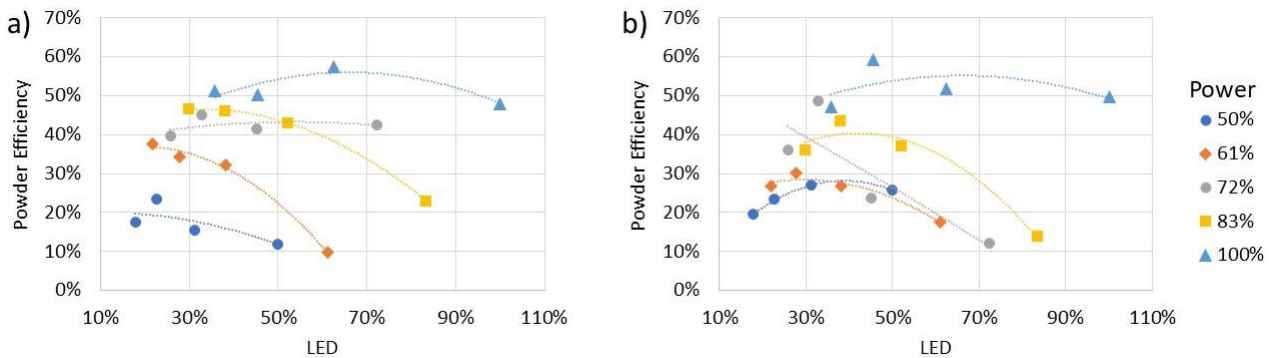


Fig. 4.11 Powder efficiencies for 70% a) and 90% b) powder feed rate

Summing up, the on-top analysis allowed to exclude the 100% and 50% values of laser power because they lead to severe oxidation phenomena and insufficient and/or irregular deposition, respectively. The ineffectiveness of 50% P deposition was confirmed by the cross-section images that highlighted their poor quality. Then, the meltpools' dimensions were measured and studied in function of LED and power. W exhibited a clear trend, it increased with LED and P. G showed a similar behavior but, in some samples, after a maximum value it decreased. Both W and G slightly increased with F . D , instead, slightly decreased with F , even if its trend was not clear. The ratio G/D was calculated to judge the deposition effectiveness. All the samples, except one, had an excessive G and were above the optimal range, even if the majority of them was acceptable. In this case, G/D increased with F and so lower value was preferred. At the end, the powder efficiency was calculated in order to understand the amount of powder that actually solidified into the scan track. Low power and low scanning speed were particularly detrimental, leading to very low P_e values. So, higher power and middle-high scanning speed were preferable.

4.3 Cubes

The analysis on the cubes started with some preliminary observations of their general deposition quality, regarding their shape, size and surface finish.

All the lateral surfaces were flat and perpendicular to the baseplate. The top surfaces, conversely, were not as flat as the lateral ones. For this reason, the minimum and the maximum heights were measured for each cube and compared to the theoretical value of 15 mm. The obtained height ranges were further studied in function of the VED. The deposition quality was classified through colours and, in general, higher VED produced better cubes, as depicted in **Fig. 4.12**.

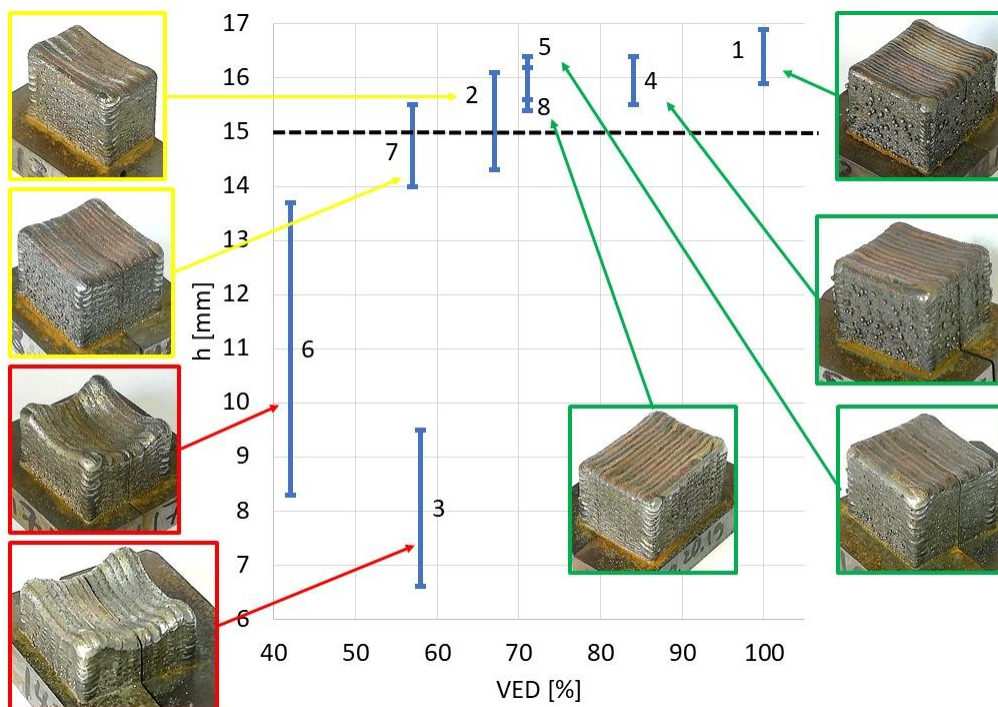


Fig. 4.12 Evaluation of the heights in function of the VEDs

All the green cubes had a VED above 70% and their height was slightly above the expected value of 15 mm. The difference between the maximum and minimum heights were very small too, around 1 mm. Thus, they had a good dimensional stability, and the top surfaces were almost flat. The yellow cubes intersected the value of 15 mm, and the height spans were larger, resulting in a less flat top surface. Critical issues were observed in the red cubes. Not only their heights were well below the expected value, but also the central parts of their upper faces actually collapsed, resulting in an unacceptable outcome. The cube #6, for example, had both excessive z-step and hatching distance, leading to the lowest VED amongst all the cubes. Despite its 100% powder feed rate, the final outcome is a very bad deposition in terms of geometrical stability. This happened because, during the building, after the deposition of each layer, the deposition head moved up more than the actual growth of the just deposited layer. Also, higher z-step implies a lower number of layers deposited, further enhancing the sample collapse problem. For these reasons, the z-step of the deposition head must be set as close as possible to the layer growth. At the opposite, setting a too low z-step would cause an excessive remelt of the previous layers and an inefficient deposition.

Furthermore, some other issues were observed on some samples regarding their low surface finish. Sample #1 had many adhered round particles on its lateral surfaces, their sizes generally increased with the cube's height, up to 1mm in diameter. Analog particles but lower in number and size were present also on the cubes #4 and #7. The other cubes, instead, showed a much better lateral surface finish, in particular #3 and #6.

The aforementioned samples' characteristics are compared in **Fig. 4.13**.

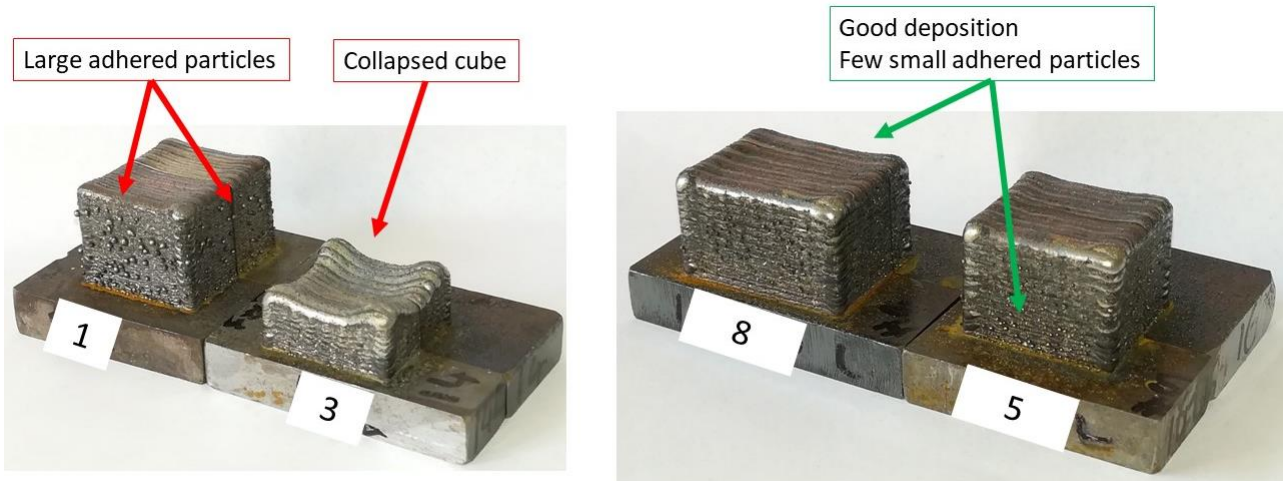


Fig. 4.13 Examples of cubes with the highlighted features. White labels indicate the sample ID number

The finish of the top surfaces, instead, were very similar one another. Scan tracks were clearly visible and created a ribbed surface. This is typical of the DED deposition and depend on the laser spot diameter.

In conclusion, it was observed that high VEDs produced geometrically stable cubes but with a poor lateral surface finish. On the other hand, low VEDs had opposite outcomes. Thus, according to this preliminary observation, the best process parameter set was associated to both the cubes #5 and #8. They combined the best geometrical stability with a very good lateral surface finish, compared to the other samples.

After this preliminary observations, the cubes' cross-sections were analysed in terms of porosity and hardness. The building parameters and the main results of these analysis are provided in **Table 4.6**

Table 4.6 Cubes' building parameters and general results of the porosity and hardness analysis

Sample ID	1	2	3	4	5	6	7	8
Power	50%	61%	72%	61%	72%	72%	50%	72%
Scanning speed	57%	57%	79%	64%	64%	79%	71%	64%
Powder flow	50%	70%	70%	70%	80%	100%	70%	80%
HD	71%	93%	93%	93%	93%	100%	71%	93%
ΔZ	56%	78%	78%	56%	78%	100%	78%	78%
VED	100%	67%	58%	84%	71%	42%	57%	71%
Build Rate [cm ³ /h]	24.0	43.7	60.1	35.1	49.1	83.2	42.0	49.1
Porosity [%]	0.092	0.044	0.078	0.031	0.041	0.034	0.033	0.030
Standard Deviation [%]	0.044	0.016	0.042	0.018	0.022	0.052	0.029	0.037
Average Hardness [HV]	406	400	392	418	413	399	415	403
Standard Deviation [HV]	4.9	11.6	7.1	5.5	7.2	11.0	10.8	7.1

The build rate expresses how fast the deposition is, in terms of built volume per unit of time [64]. It is calculated as the product of scanning speed, hatching distance and layer thickness and it is measured in cm³/h.

$$\text{Build rate} = v \cdot HD \cdot \Delta Z \quad (4.6)$$

This index represents an additional judgement parameter that was used at the end of the analysis.

4.3.1 Porosity

From each image taken at the optical microscope, a percentual value of porosity was found. The results of all images collected are reported in **Table 4.7**. In particular, to facilitate the readability, a scale of colours was assigned: green for values below 0.030% up to red for values over 0.17%. Porosity values, in fact, lied in a rather wide range, from 0.007% in samples #6 and #8 to 0.249% in sample #6.

Table 4.7 Results of images analysis for porosity

		Sample ID							
		1	2	3	4	5	6	7	8
Image porosity [%]	1	0.119	0.055	0.116	0.024	0.042	0.021	0.030	0.054
	2	0.130	0.053	0.217	0.029	0.048	0.010	0.033	0.065
	3	0.090	0.049	0.134	0.049	0.040	0.016	0.016	0.017
	4	0.072	0.027	0.079	0.034	0.026	0.028	0.012	0.027
	5	0.021	0.041	0.086	0.071	0.056	0.014	0.048	0.014
	6	0.168	0.048	0.044	0.013	0.028	0.011	0.015	0.041
	7	0.178	0.031	0.027	0.026	0.030	0.023	0.019	0.012
	8	0.111	0.069	0.074	0.024	0.095	0.027	0.026	0.014
	9	0.100	0.049	0.051	0.014	0.023	0.044	0.150	0.050
	10	0.122	0.042	0.068	0.015	0.010	0.017	0.024	0.170
	11	0.046	0.024	0.049	0.012	0.039	0.020	0.014	0.027
	12	0.134	0.052	0.066	0.026	0.077	0.047	0.041	0.008
	13	0.031	0.089	0.072	0.024	0.027	0.249	0.025	0.011
	14	0.047	0.057	0.058	0.039	0.044	0.023	0.019	0.010
	15	0.092	0.035	0.050	0.051	0.024	0.038	0.033	0.016
	16	0.069	0.031	0.091	0.075	0.032	0.007	0.028	0.007
	17	0.061	0.027	0.070	0.031	0.021	0.019	0.033	0.008
	18	0.127	0.030	0.045	0.016	0.041	0.018	0.033	0.010
	19	0.050	0.029	0.107	0.021	0.084	0.044	0.018	0.019
	20	0.077	0.033	0.065	0.020	0.026	0.008	0.033	0.015
Average Porosity [%]		0.092	0.044	0.078	0.031	0.041	0.034	0.033	0.030
Standard Deviation [%]		0.044	0.016	0.042	0.018	0.022	0.052	0.029	0.037

Then, for each sample, standard deviation was calculated. It was observed that, in some of them, due to their extremely wide range of porosities, standard deviation even exceeded the average value. All the samples achieved a good average porosity, below 0.1%. #1 and #3 were respectively 0.092% and 0.078%, while the others were well below these values, between 0.044 and 0.030. The best samples were #4, #6, #7 and #8.

For a better visualization of the results, the average porosity values were plotted in function of VED and pictures with the porosity value close to the average ones were placed beside the corresponding samples (Fig. 4.14).

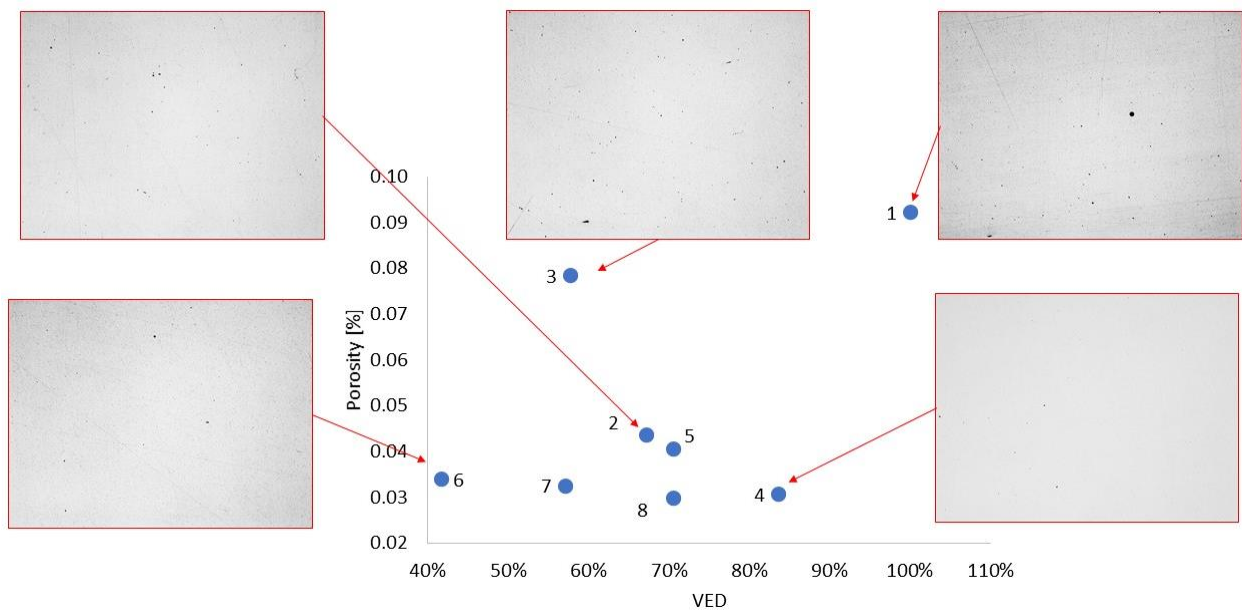


Fig. 4.14 Average porosity and relative images

Moreover, the effects of other parameters, such as laser power, scanning speed and powder flow were singularly investigated in Fig. 4.15. However, due to the low number of samples available and the high number of parameters varying among them, no plausible trends were found.

However, Mathoho et al. [37] studied the effects of process parameters on 17-4 PH samples produced by DED and concluded that high scanning speed promoted pore formation, probably because the meltpool moved too fast to fill some pores. On the other hand, an insufficient scanning speed might cause an excessive heat concentration, causing evaporation and pores formation. High LEDs, in fact, promote evaporation and pores formation. They also observed that lower powder feed rate resulted in higher porosity samples.

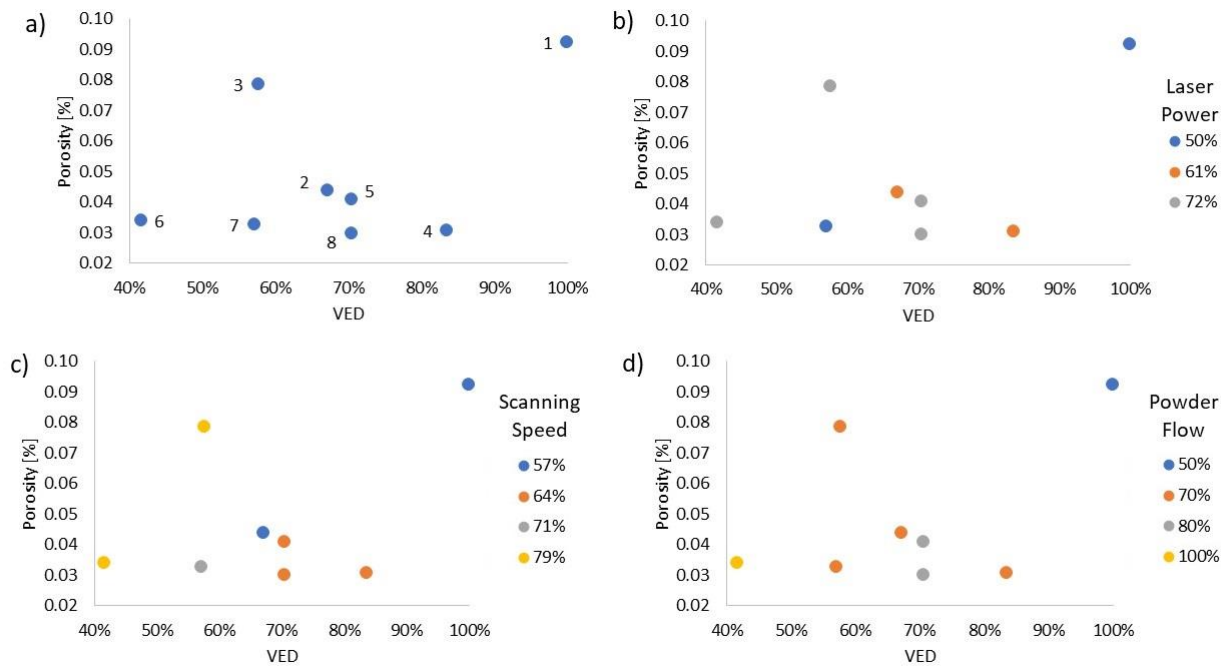


Fig. 4.15 Average cube porosity in general a) and divided by power b), scanning speed c) and powder flow d)

Maximum porosity images were collected in **Fig. 4.16**. They exhibited a decreasing trend with respect to the VEDs, even if sample #1 represented an exception. Also, an interesting behaviour was observed: high porosity percentages could be caused by different factors: the presence of one large pore, such as samples #6 and #8, many small pores like #1 and #4 or an intermediate situation between them, like #3 and #7.

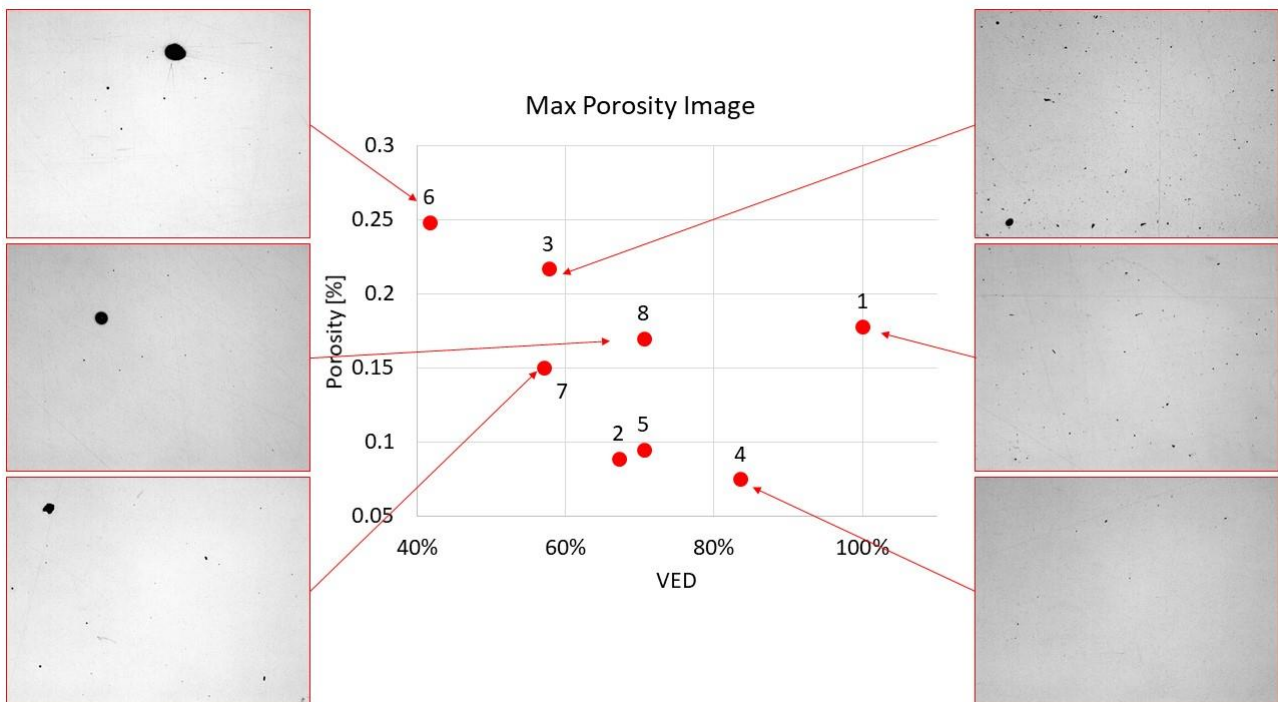


Fig. 4.16 Collection of images with the highest average porosity

Nevertheless, the average value is not the only parameter to judge the quality of the samples: different studies [55], [62], [63], [74] showed that the size of the pores could strongly influence the mechanical properties of the AM processed components. For example, few large pores would be more detrimental than many small ones, even if the average porosities were the same. For this reason, the following analysis concentrated on the pore size.

Hence, the dimensions of the largest pores were measured, both in terms of area and of maximum Feret diameter. In **Fig. 4.17**, the majority of samples had the trends of maximum porosity images and largest pores almost coincident, but not samples #1 and #3. This means that in those samples, the maximum porosity was mainly distributed in smaller pores rather than in one large.

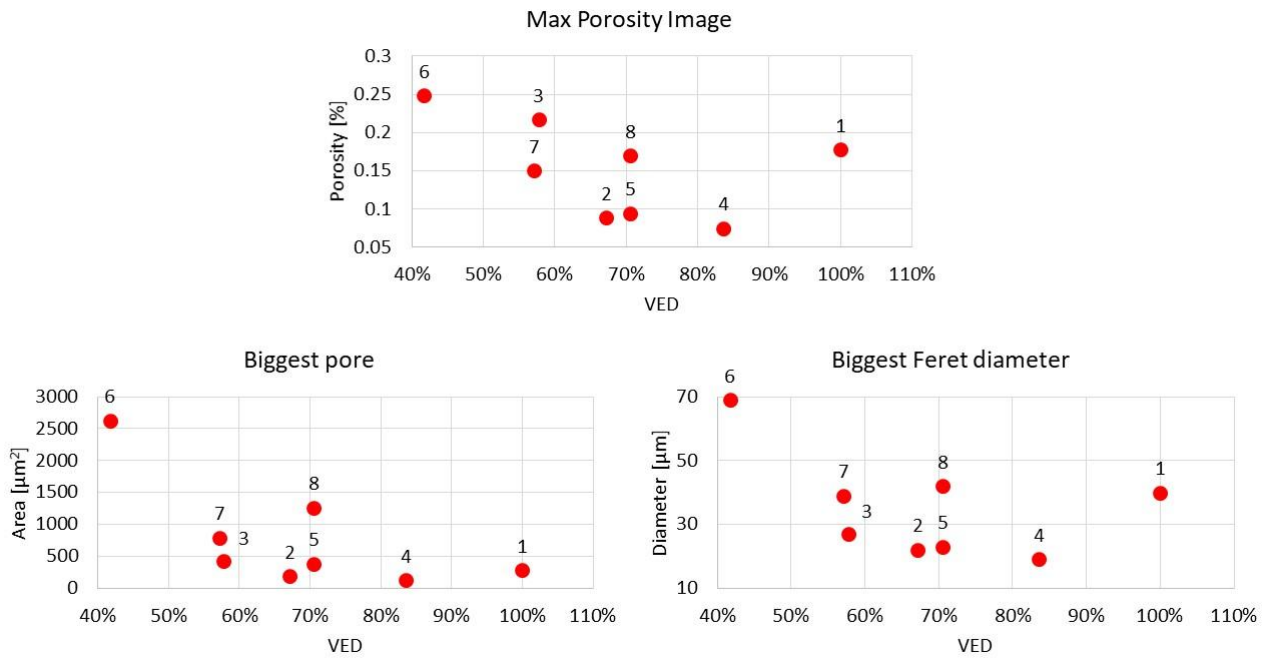


Fig. 4.17 Comparison of maximum porosity images and largest pores

After this consideration, all the images were further processed to classify the dimensions of each visible pore, rather than considering the total porosity. The first parameter measured was the area: pores below the threshold of $4 \mu\text{m}^2$ were considered negligible or just image artifacts, thus were excluded from the following analyses. Then, assuming each pore a perfect circle, the equivalent diameter d_{eq} , was calculated from its area A as

$$d_{eq} = \sqrt{\frac{4 \cdot A}{\pi}} \quad (4.7)$$

The second parameter measured was the maximum Feret diameter was measured. Its lowest value found was $2.7 \mu\text{m}$, corresponding to an area of $4 \mu\text{m}^2$ and will be discussed later.

The largest pore of all was found in sample #6 and had an area of $2629 \mu\text{m}^2$, corresponding to an equivalent diameter of $57.9 \mu\text{m}$. Its maximum Feret diameter was $69.1 \mu\text{m}$.

24 diameter classes were defined at a step size of $2.5 \mu\text{m}$, up to $70 \mu\text{m}$. For each sample, the pores were divided in these classes. The numerical frequency expressed how many pores belonged to each class. The

results were expressed as percentages of the total number of pores detected in the sample, because, trivially, the total number depends on how many images were taken.

As reported in **Table 4.8**, for every sample, more than 80% of the detected pores had an equivalent diameter below 5 μm and up to 95% of the total number had an equivalent diameter below 7.5 μm^2 . Also, the most of classes from 20 μm to 70 μm was empty. This means that larger pores were extremely low in number. To facilitate the readability of the results the empty classes were excluded from the following tables.

Table 4.8 Numerical frequency of equivalent diameters, divided into diameter classes

Class interval [μm]	Sample ID							
	1	2	3	4	5	6	7	8
0 - 2.5	14.7%	19.2%	19.2%	19.0%	13.2%	20.0%	23.1%	17.4%
2.5 - 5	73.2%	69.2%	73.3%	61.6%	72.2%	66.3%	64.8%	63.9%
5 - 7.5	9.7%	9.0%	5.6%	11.9%	9.6%	8.0%	9.6%	13.9%
7.5 - 10	1.3%	1.8%	1.1%	4.5%	2.9%	4.0%	2.1%	
10 - 12.5	0.7%	0.3%	0.7%	3.0%	1.5%			3.5%
12.5 - 15	0.3%	0.3%			0.3%	0.6%		
15 - 17.5		0.3%				0.6%		0.7%
17.5 - 20	0.1%							
20 - 22.5			0.1%		0.3%			
30 - 32.5							0.4%	
40 - 42.5								0.7%
57.5 - 60						0.6%		

This approach, however, was not enough satisfactory because the importance of the bigger pores, even if they were only few, was supposed to be much more than few percentage points. For this reason, a diameter-normalization was carried out in the following way.

Each i -th class contained n_i elements. The weight of each class wt_i was calculated summing the diameters of all its pores.

$$wt_i = \sum_{k=1}^{n_i} d_k \quad (4.8)$$

Finally, the influence of the i -th class (X_i) was calculated as the ratio between the corresponding weight wt_i and the sum of the weights of the 24 classes.

$$X_i = wt_i / (\sum_{h=1}^{24} wt_h) \quad (4.9)$$

As reported in **Table 4.9**, after this calculation, the few large pores could cover up an important percentage of total porosity area: 59% in sample #6 and 48% in #8. Consequently, these samples showed lower percentages in the smaller classes than the other samples.

Table 4.9 Diameter-normalized frequency of equivalent diameters, divided into diameter classes

Class interval [μm]	Sample ID							
	1	2	3	4	5	6	7	8
0 - 2.5	9.7%	13.1%	13.5%	11.5%	8.3%	11.9%	15.9%	9.9%
2.5 - 5	67.5%	65.0%	70.9%	53.0%	63.3%	54.9%	59.5%	51.3%
5 - 7.5	16.0%	14.7%	9.7%	17.6%	14.8%	11.8%	16.3%	20.3%
7.5 - 10	2.8%	4.3%	3.1%	9.8%	6.5%	9.0%	5.1%	
10 - 12.5	2.2%	0.7%	2.1%	8.1%	4.3%			9.3%
12.5 - 15	1.1%	1.1%			1.1%	1.8%		
15 - 17.5		1.1%				2.2%		2.5%
17.5 - 20	0.7%							
20 - 22.5					1.7%			
22.5 - 25			0.8%					
30 - 32.5							3.2%	
40 - 42.5								6.7%
57.5 - 60						8.3%		

Sample #3 had a good porosity distribution because no excessively big pores were found and so the highest contribution is given by very small pores (below 5 μm). Sample #7, on the other hand, started to show some issues because, even if it did not have pores in the range 10-30 μm , only one pore gave a not negligible contribution of 3.2%. Sample #6 was the worst because more than the 10% of its total porosity was concentrated in a very few and very large pores, which, under the mechanical properties point of view, might be the most detrimental [62] because they might reduce the loaded cross-section area [55]. However, as mentioned in Chapter 1.3.2, samples built via DED technology shows very small pores and low average porosity values. Kleszczynski et al. [63] stated that only huge defects (> 1mm long) have negative effects on yield strength of 17-4 PH samples. Such large defects are typically caused by other AM techniques, such as L-PBF. Thus, the pores found in this thesis were too small to represent an issue.

Moreover, Biswal et al. [55] stated that the shape of voids is more meaningful than their size and the elongated ones could be particularly detrimental to mechanical properties. For this reason, a deeper investigation was conducted on the shape of the pores measuring the Feret's diameters. Then, the results were compared to the equivalent diameters previously calculated.

So, a similar statistical analysis was conducted on the Feret diameters maintaining the same diameter classes. The numerical distributions are provided in **Table 4.10**, while the diameter-normalized ones in **Table 4.11**.

Table 4.10 Numerical frequency of maximum Feret diameters, divided into diameter classes

Class interval [μm]	Sample ID							
	1	2	3	4	5	6	7	8
2.5 - 5	65.4%	67.7%	67.9%	59.0%	64.9%	73.1%	72.2%	66.0%
5 - 7.5	20.9%	23.1%	21.2%	24.6%	21.6%	18.9%	18.9%	17.4%
7.5 - 10	8.8%	7.4%	6.8%	7.5%	8.2%	3.4%	6.4%	10.4%
10 - 12.5	1.8%	0.5%	1.6%	5.2%	3.2%	2.3%	1.4%	2.8%
12.5 - 15	1.8%	0.3%	0.7%	1.9%	1.2%	1.1%	0.7%	0.7%
15 - 17.5	0.4%	0.8%	0.7%	1.1%	0.3%			0.7%
17.5 - 20	0.1%		0.2%	0.7%	0.3%			1.4%
20 - 22.5	0.3%	0.3%	0.6%			0.6%		
22.5 - 25			0.1%		0.3%			
25 - 27.5	0.3%		0.2%					
37.5 - 40							0.4%	
40 - 42.5	0.1%							0.7%
67.5 - 70						0.6%		

Table 4.11 Diameter-normalized frequency of maximum Feret diameters, divided into diameter classes

Class interval [μm]	Sample ID							
	1	2	3	4	5	6	7	8
2.5 - 5	48.0%	52.2%	50.8%	39.8%	48.0%	53.3%	55.5%	45.4%
5 - 7.5	23.7%	29.2%	25.3%	27.4%	25.2%	22.4%	24.2%	19.1%
7.5 - 10	14.3%	13.1%	11.5%	11.6%	13.5%	6.1%	11.9%	15.8%
10 - 12.5	3.8%	1.2%	3.4%	10.7%	7.0%	4.9%	3.3%	5.8%
12.5 - 15	4.7%	0.7%	1.8%	4.6%	3.1%	3.1%	2.2%	1.8%
15 - 17.5	1.2%	2.5%	2.2%	3.3%	0.9%			2.0%
17.5 - 20	0.5%		0.8%	2.5%	1.0%			4.6%
20 - 22.5	1.1%	1.2%	2.5%			2.3%		
22.5 - 25			0.5%		1.3%			
25 - 27.5	1.4%		1.2%					
37.5 - 40							3.0%	
40 - 42.5	1.1%							5.4%
67.5 - 70						7.9%		

The distributions were similar to the equivalent diameter ones: small diameter pores were much more numerous, but they had a lighter impact on the total porosity.

In order to study the circularity of the pores, the diameters-normalized distributions of the equivalent diameters and the Feret diameters' ones were compared in **Fig. 4.18**.

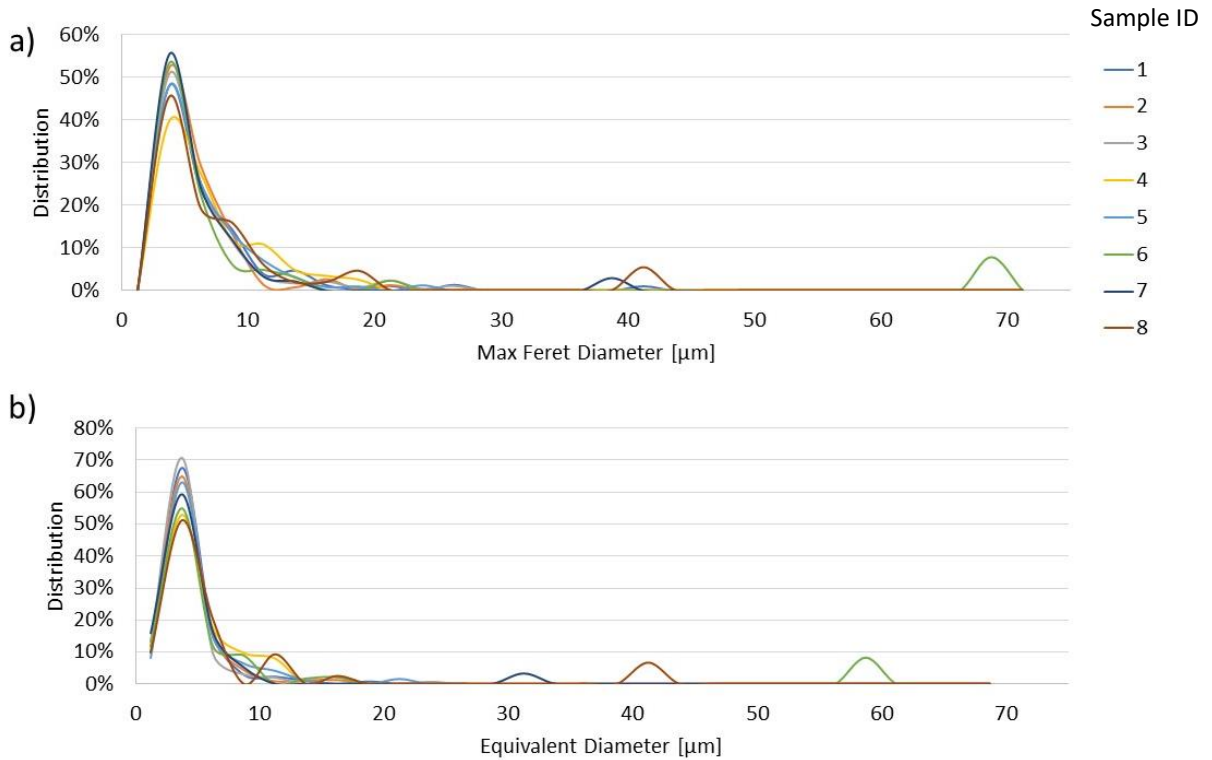


Fig. 4.18 Diameter-normalized distributions of the Feret (a) and the equivalent (b) diameters

Generally, the peaks below 10 μm were higher and narrower in d_{eq} than in Feret. The peaks corresponding to larger, instead, had the same shapes but were shifted on the left because they usually indicate one single pore.

Excluding the case limit of a perfectly round pores

$$d_{eq} < Max_{Feret} \quad (4.10)$$

Since these two values did not differ much, it was concluded that pores had predominantly a rather regular shape. Thus, Feret diameters found were consistent with the corresponding equivalent diameters and no large and very elongated shaped voids were present.

By way of example, a comparison between the two diameters in the cube #1 is shown in **Fig. 4.19**. It was in line with the aforementioned considerations.

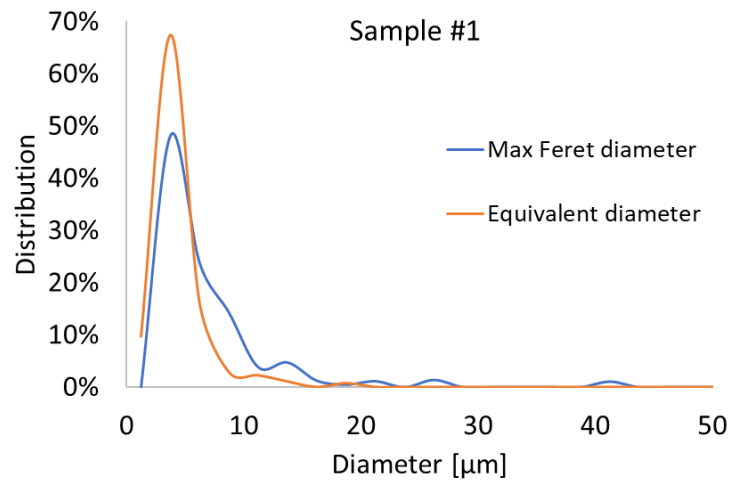


Fig. 4.19 Comparison between Max Feret and equivalent diameter-normalized distributions

A deeper inspection on the shapes of the largest pores found, i.e., with an area above $100 \mu\text{m}^2$, was performed, since they had a greater importance compared to the others. In this case, both minimum and maximum Feret diameters were measured (**Fig. 4.20**) and their ratio, called Feret Ratio, was calculated.

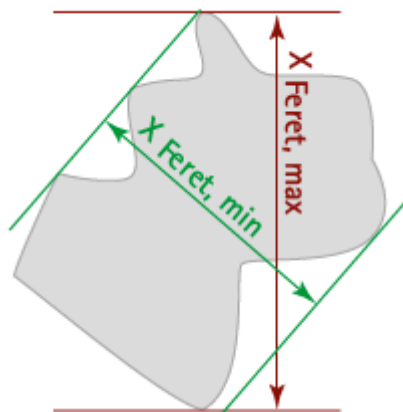


Fig. 4.20 Representation of Min and Max Feret diameters

The ratio equals 1 for perfectly round pores and the more the shape is irregular, the lower the ratio gets. The results are collected in **Table 4.12**.

Table 4.12 Details of pores above 100 μm^2

Sample ID	Area [μm^2]	d_{eq} [μm]	Feret Max [μm]	Feret Min [μm]	Feret Ratio
6	2629	58	69	53	0.76
8	1261	40	42	40	0.95
7	793	32	39	30	0.76
3	429	23	27	21	0.77
5	382	22	23	22	0.95
1	280	19	40	19	0.47
2	191	16	17	16	0.94
6	181	15	21	13	0.64
8	178	15	18	15	0.84
2	175	15	22	15	0.67
5	165	15	15	14	0.93
1	159	14	15	14	0.94
1	132	13	26	12	0.46
6	123	13	13	12	0.93
4	121	12	17	10	0.61
1	120	12	13	12	0.94
5	114	12	13	12	0.89
1	110	12	21	12	0.56
5	109	12	14	12	0.88
8	109	12	16	11	0.71
1	107	12	19	13	0.68
8	107	12	18	10	0.58

The highlighted values represented the most irregular shaped pores, and they all were on the sample #1. The picture of the largest one is reported in **Fig. 4.21**. The cube #1 had the highest VED, suggesting that excessive VEDs might promote irregular pores.

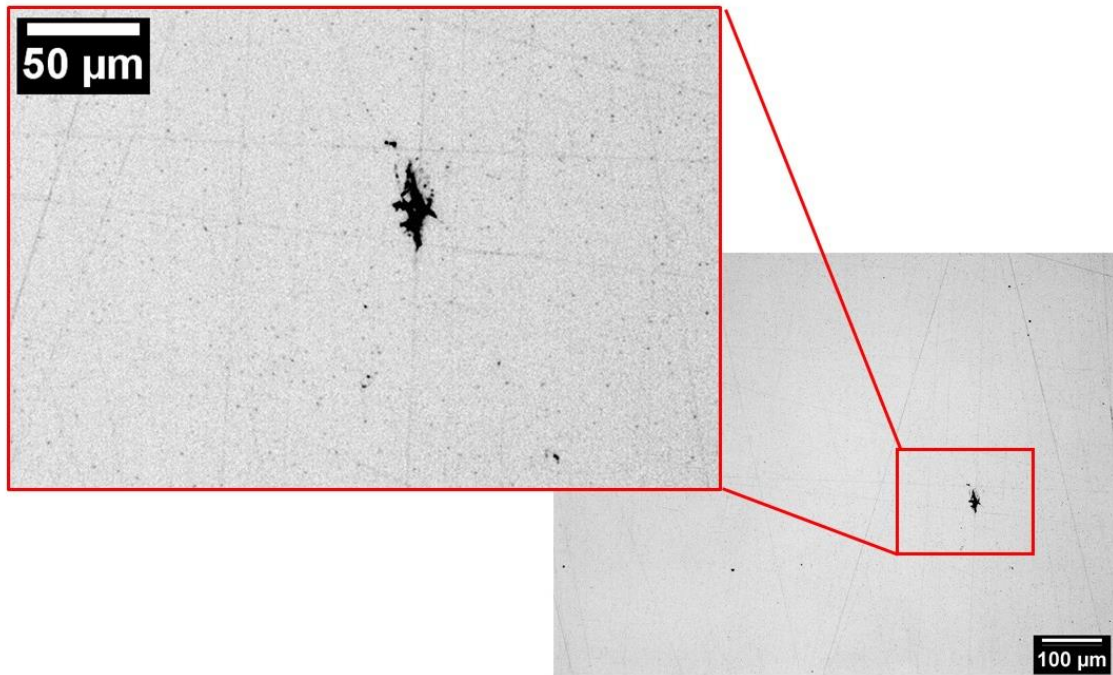


Fig. 4.21 The most irregular shaped and largest pore found in sample #1

According to the analysis performed, the pores found did not represent a big issue to the mechanical properties, neither in terms of size [63], nor in terms of shape [55].

In conclusion, cube #4 had excellent average porosity (0.030%) and also a quite low amount of large pores. On the other hand, cube #6 had a similar average value (0.034%) but showed some large pores.

Cube #4 might have one of the best process parameters, but a practical consideration was done comparing the previously mentioned build rates [64]. The values ranged between 24 and 83 cm³/h and were reported in **Fig. 4.22**.

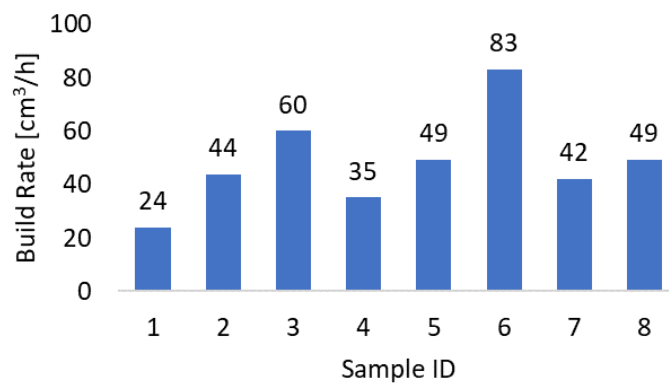


Fig. 4.22 Build rates of the samples

Not necessarily high build rates resulted in high porosity, for example cube #1 had the lowest build rate and the highest porosity. Cube #4 had a rather low build rate and so a compromise between porosity and build rate was necessary: cubes #5 and #8 had the same process parameters and showed a slightly higher porosity but a 40% higher build rate, for this reason, this might be considered the best set of parameters. Finally, the cube #7 was in an intermediate situation between #4 and #5 both in terms of porosity than build rate.

After these considerations, the samples were again observed under the optical microscope, focusing on the research of defects. Some pores were photographed at higher magnification, i.e., 500x and a selection of them was collected in **Fig. 4.23**. In some pictures, suspect oxides were present but due to their nanometric dimensions, they were considered negligible and probably caused by the manipulation of the samples rather than their building process.

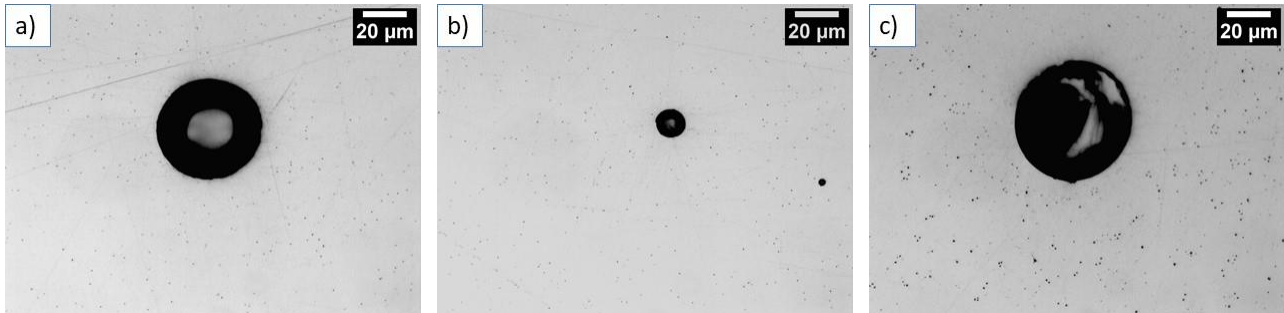


Fig. 4.23 Porosities on cubes #2 (a), #4 (b) and #7 (c) at 500x magnification

Main defectiveness was found on the cube #3 at the interface with the base plate (**Fig. 4.24**). In particular, an extremely high number of pores was present on the baseplate and many defects, about 100 µm long, were spread along the interface line.

Such a high defectiveness is clearly unacceptable and, maybe, was caused by an excessive scanning speed (100%) combined to an insufficient powder feed rate (70%).

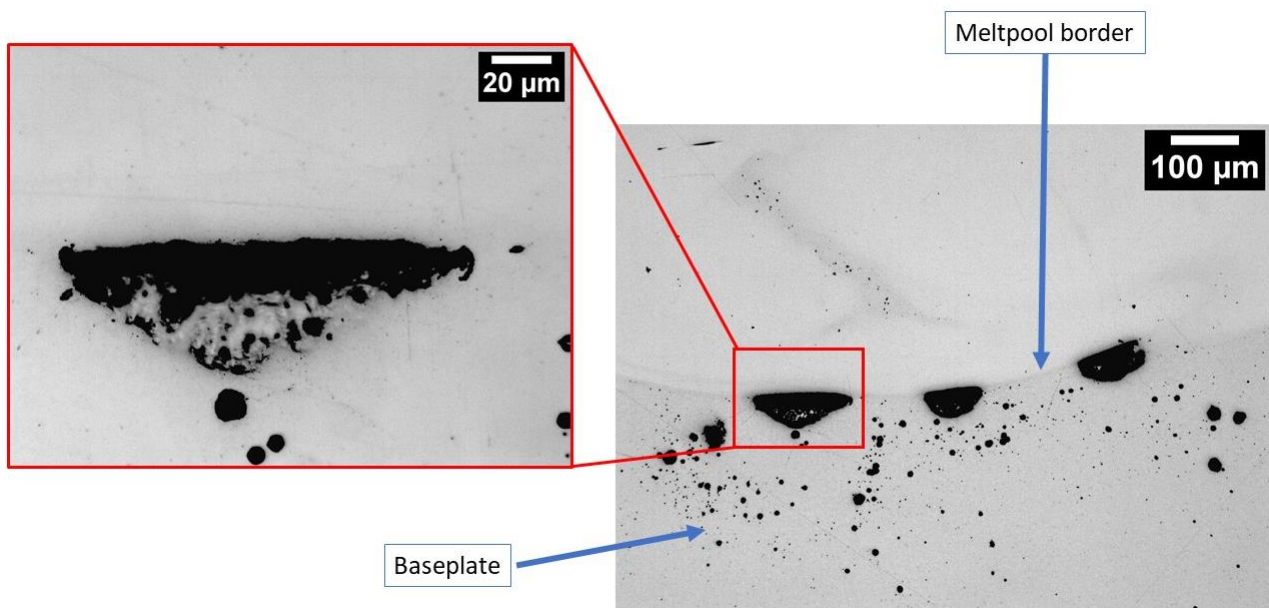


Fig. 4.24 Defects and porosities at the base interface in cube #3 at 100x and 500x magnifications

Many other defects were found in cube #6 (**Fig. 4.25**). Their size and shape were compatible with powder particles and so it was concluded that those were partially melted particles.

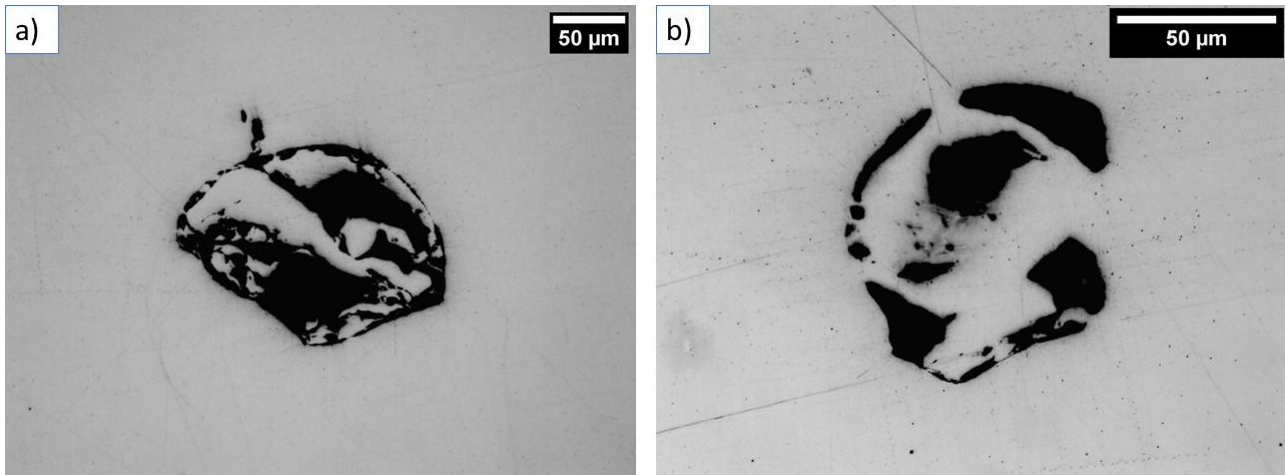


Fig. 4.25 Defects on cube #6 at 200x (a) and 500x (b) magnification

This cube was the only built with 100% powder flow rate. This excessive value, probably, had promoted the presence of partially molten particles. Also, the scanning speed was 100% and this resulted in a lower interaction time to effectively melt all particles, despite the 100% laser power.

Some other defects are reported in **Fig. 4.26**, after the acid etching.

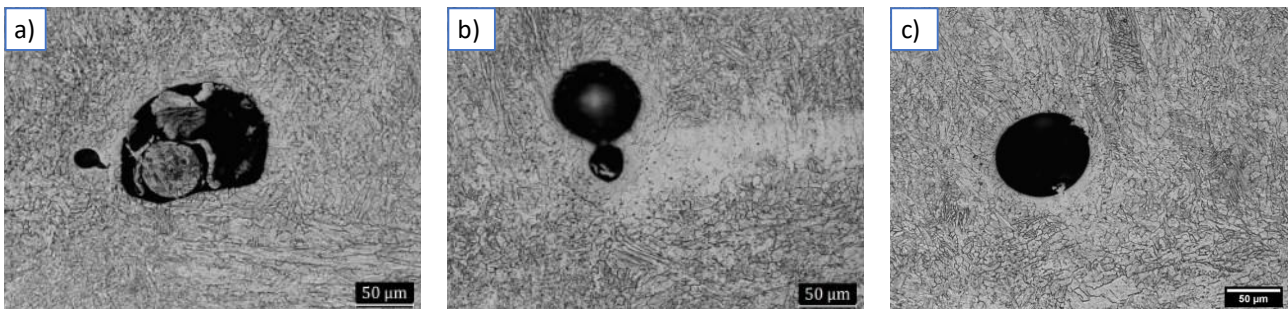


Fig. 4.26 Fusion defects (a), (b) and pore (c) in the sample #6 at 200x magnification after the etching

Samples were further observed under Scanning Electron Microscope (SEM) and few elongated pores were found (**Fig. 4.27**). Their lengths were irrelevant i.e., below 10 μm , in most cases. The only exception was found on the cube #6, with a length of around 20 μm .

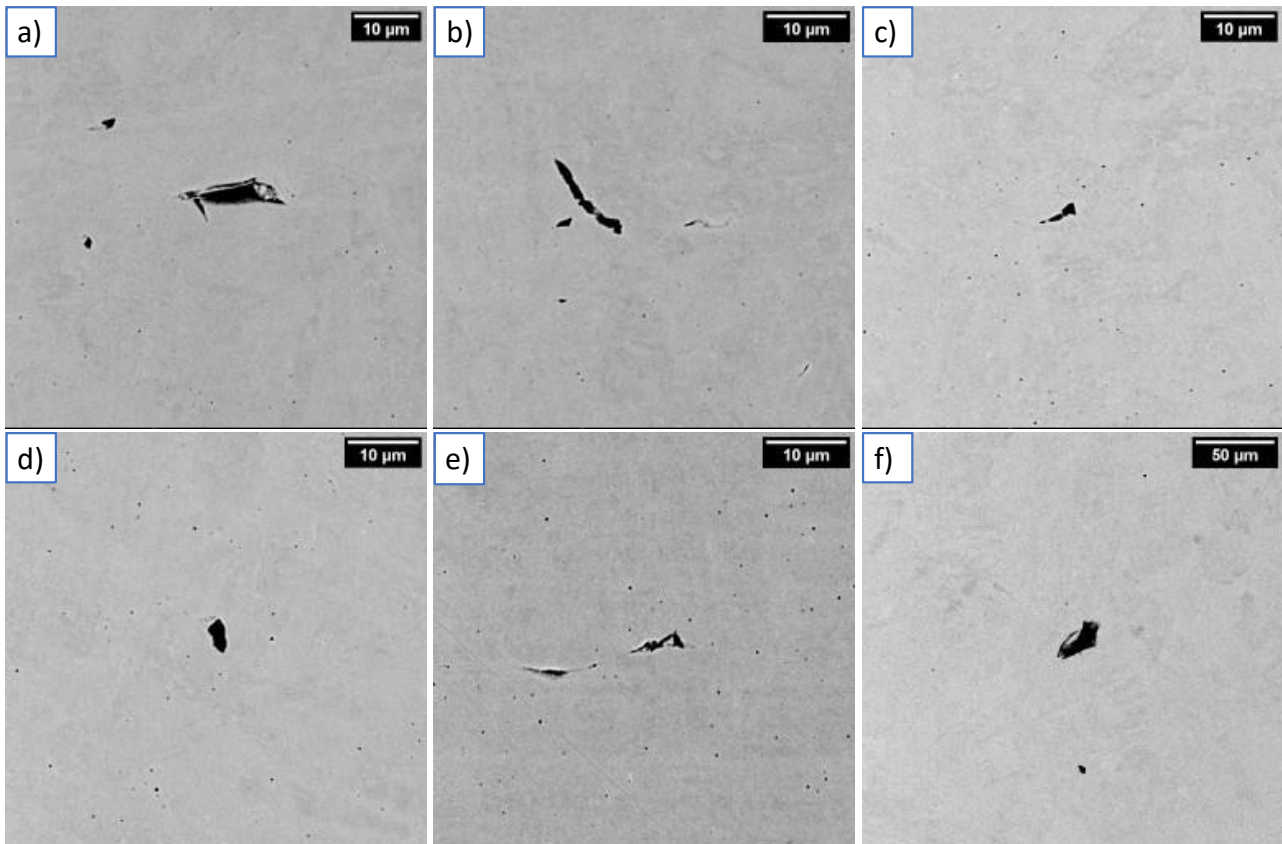


Fig. 4.27 SEM images of sample #1 (a,b,c), sample #2 (d), sample #3 (e) and sample #6 (f)

During the SEM analysis, the only noteworthy element was observed on sample #6 and it was judged as a potential oxide **Fig. 4.28**. All the possible oxides observed so far had nanometric dimensions but this one was much larger, with a diameter of 4.8 μm .

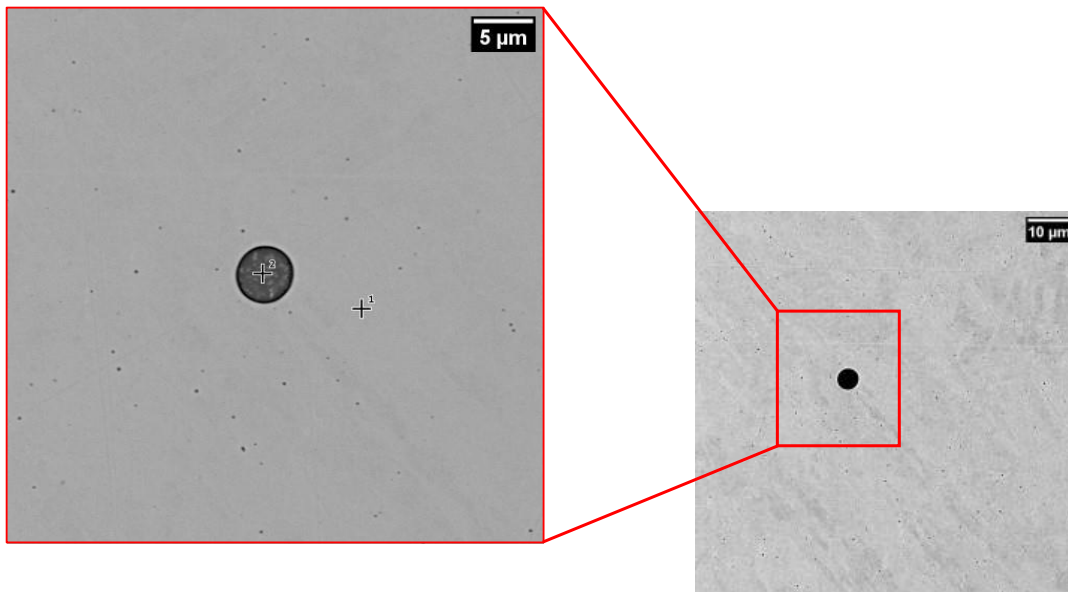


Fig. 4.28 Suspected oxide on sample #6

Thanks to its larger dimension, a deeper inspection was possible. An *Energy Dispersive Spectroscopy* (EDS) was performed selecting two points: the centre of the suspect oxide and the surrounding metal for a comparison. EDS is a function of SEM microscopes and offered an estimation of the chemical composition of the selected points, exploiting the diffraction of the electrons. The results are reported in **Table 4.13**.

Table 4.13 Comparison of chemical composition between metal and suspect oxide

Metal			Suspect Oxide		
Element	Atomic Conc. [%]	Weight Conc. [%]	Element	Atomic Conc. [%]	Weight Conc. [%]
Fe	76.34	77.68	O	50.85	27.03
Cr	16.79	15.91	Cr	15.40	26.60
Cu	2.44	2.83	Si	18.42	17.19
Ni	2.37	2.54	Fe	9.09	16.87
Si	2.05	1.05	Mn	5.51	10.06

The composition of the metal was in line with the expected values, found in the supplier's datasheet. The suspected oxide, instead, was characterized by a high oxygen content and also chromium and silicon. The corresponding oxides are Cr_2O_3 or SiO_2 but the uncertainty in this case was too high. In conclusion, on the basis of the analysis carried out, the presence of other relatively large oxides was not detected but, however, further researches might be necessary.

4.3.2 Microstructure

After the etching, the samples were once again observed under the optical microscope to study their microstructure. At 50x and 100x magnifications, the meltpool borders were visible. All the samples were built adopting the 0-90° scanning strategy. Thus, the longitudinal and the transverse cross-sections of the scan tracks were alternated in the z direction. The transverse cross-sections were obviously more significant because they showed much more information. The grain growth directions were, as expected and discussed in Chapter 2, preferentially perpendicular to the meltpool borders, as shown in **Fig. 4.29**.

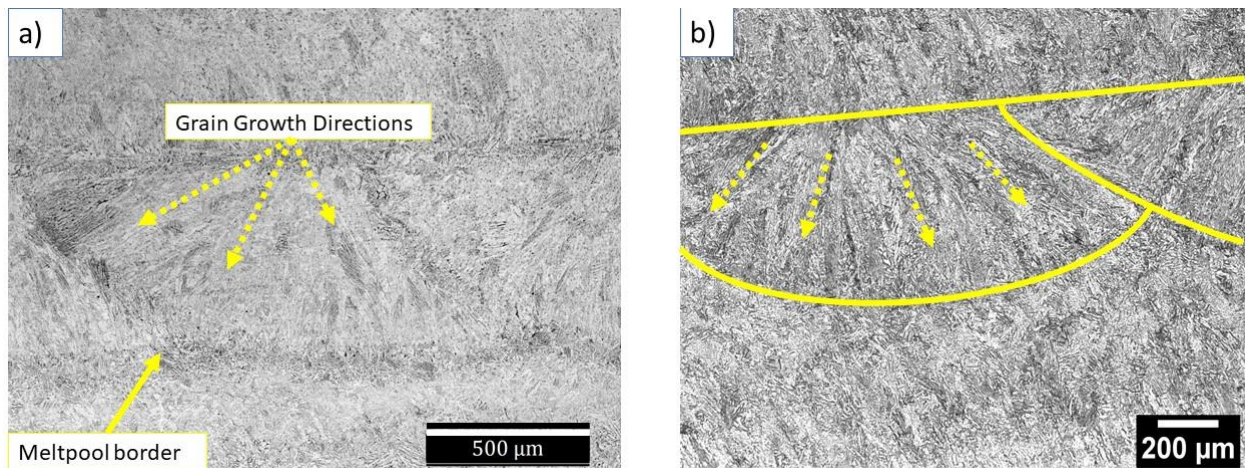


Fig. 4.29 Examples of meltpool borders at 50x magnification in samples #7 (a) and #6 (b)

Also, it was noticed that the scan tracks of the sample #7 had a higher overlap than the ones of the sample #6. The reason was that the hatching distance adopted during the building was respectively 71% and 100%. Lower hatching distance promoted a higher overlapping. Besides that, the dimensions of the scan tracks were different, too. Consistently to what observed in the SST analysis, they generally increased with laser power, while they decreased with the scanning speed.

At 500x magnification microstructure was visible: martensite and δ -ferrite dendrites were observed, consistently to what was suggested in many studies [37], [38], [40], [65]. A higher concentration of dendrites was detected at the meltpool borders (**Fig. 4.30**).

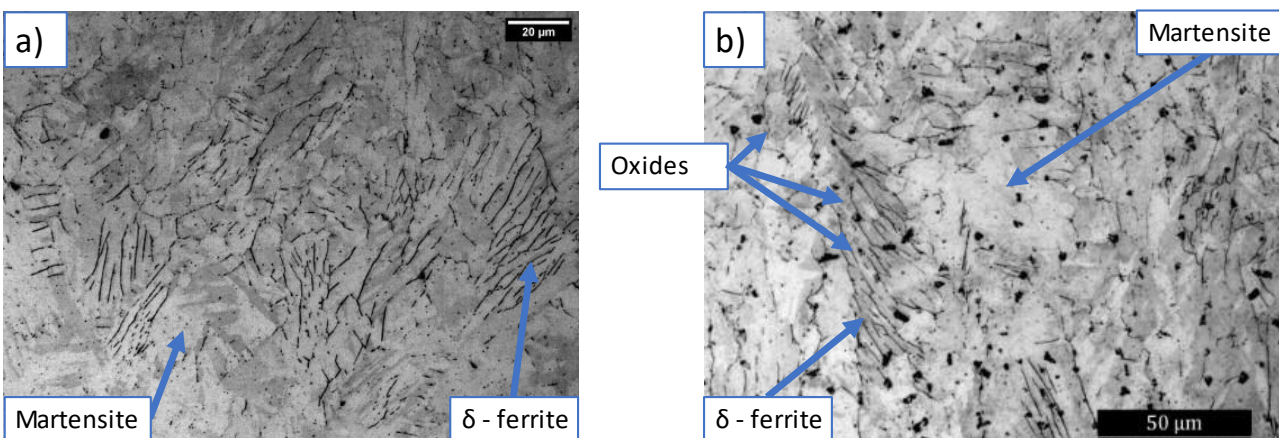


Fig. 4.30 Microstructure of sample 1 a) and sample 7 b)

In contrast to the previous optical microscope and SEM observations, in some samples, the presence of small oxides (below 5 μm in diameter) was observed in few different spots. In all probability, they were caused by the etching itself, as long as they were not present before.

As already mentioned, within the same samples, rather different microstructure appeared in different areas of the meltpools. In particular the δ -ferrite dendrites number, shape, and size (**Fig. 4.31**)

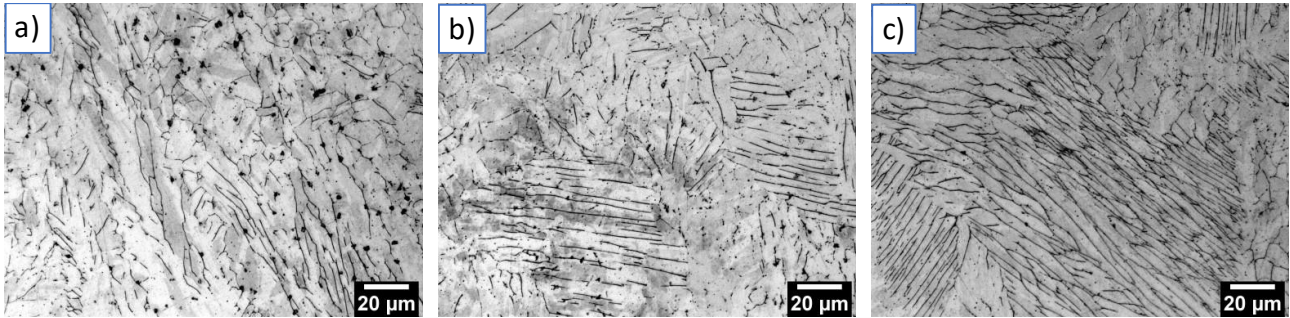


Fig. 4.31 Sample #7 at the base (a), middle (b) and top (c) portions

Considering these internal variations, every sample showed a similar microstructure. Laser power and scanning speed did not change enough to influence the microstructure. Also, such a great variety did not allow a characterization based on the building process parameters of the cubes.

4.3.3 Hardness

All the hardness measurements performed are reported in **Table 4.14** .

Table 4.14 Hardness measurements

Sample ID	Position	Measured Hardness [HV]			Position Average [HV]	Standard Deviation [HV]	Total Average [HV]	Standard Deviation [HV]
1	Top	405	413	407	408	4	406	5
	Centre	403	398	405				
	Bottom	413	402	406				
2	Top	394	385	399	393	7	400	12
	Centre	397	398	387				
	Bottom	416	407	418				
3	Top	380	395	389	388	8	392	7
	Centre	386	389	389				
	Bottom	394	404	398				
4	Top	419	405	422	415	9	418	6
	Centre	420	415	419				
	Bottom	423	420	422				
5	Top	417	405	419	414	8	413	7
	Centre	401	408	412				
	Bottom	420	415	422				
6	Top	389	385	398	391	7	399	11
	Centre	399	410	393				
	Bottom	416	392	412				
7	Top	407	408	401	405	4	415	11
	Centre	408	416	415				
	Bottom	420	433	430				
8	Top	390	398	405	398	8	403	7
	Centre	406	400	400				
	Bottom	410	413	409				

The lowest value reported was 388 HV in sample #3 and the highest one was 428 HV in sample #7. In most of the samples, hardness decreased in the z direction in fact, it was higher at the bottom and lower at the top. An exception is represented by cube #1, where this trend was not observed (**Fig. 4.32**).

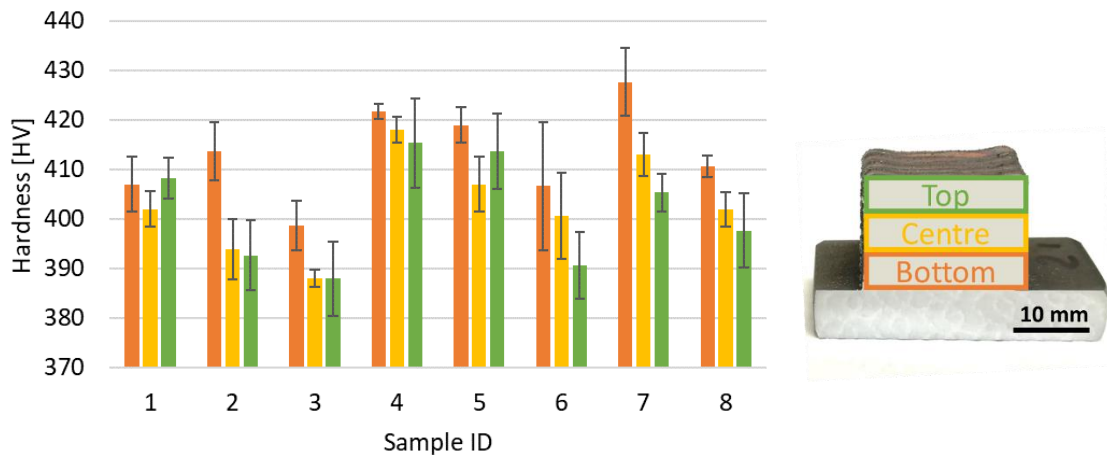


Fig. 4.32 Hardness values at different z positions

The reason of this this might be caused by the typical characteristics of heat transfer during the DED process. The bottom layers had slower cooling rate because of the many new layers deposited. These, in fact, helped the layers below to maintain a rather high temperature, vaguely resembling a precipitation hardening heat treatment. Top layers, instead, did not benefit of this effect and showed a lower hardness in most of the samples.

Then, the general average values were studied in function of the Volumetric Energy Density parameter (**Fig. 4.33**). Even if results were rather dispersed, a slight hardness increase with VED increase seemed to be present, except for cube #1. The particularly lower powder feed rate of this cube might have influenced it characteristics.

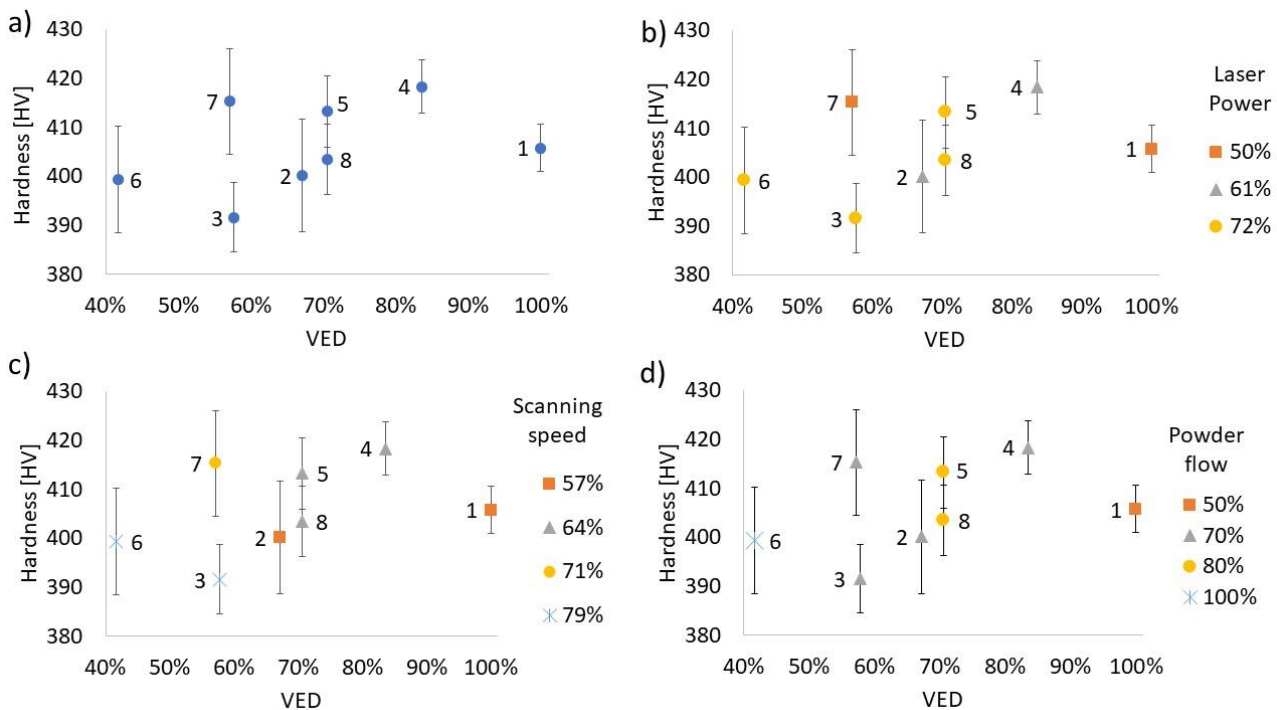


Fig. 4.33 Average cube hardness in general a) and divided by power b), scanning speed c) and powder flow d)

The effects of other parameters, such as laser power, scanning speed and powder flow were further investigated. Once again, due to the low number of samples available and the high number of parameters varying among them, no plausible trends were found.

The samples with highest hardness were #4 and #7 while the least hard was #6. A higher hardness value is not necessarily a positive characteristic because, generally, even if it is correlated to a higher tensile strength [45], it also involves lower elongation and ductility values [32]. Thus, the hardness goal depends on the final application of the component.

Additionally, the obtained hardness values were compared with other values found in the literature for the same material. The considered values referred to samples not only produced via AM techniques such as DED and L-PBF, but also via other conventional processes like press & sinter and wrought (**Fig. 4.34**).

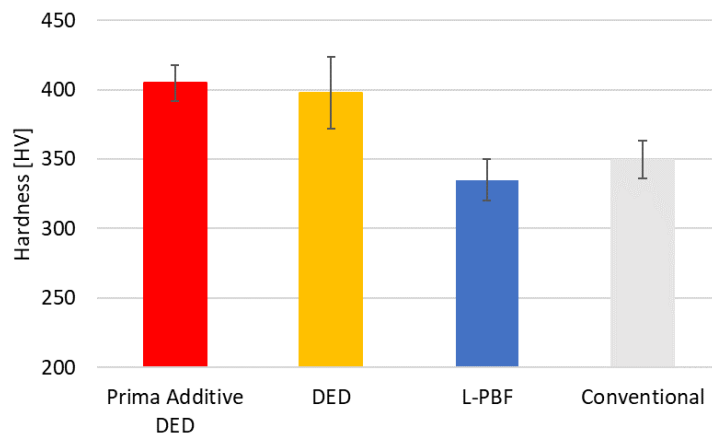


Fig. 4.34 Hardness comparison of as-built 17-4 PH samples produced via different techniques [37], [38], [66-69]

The samples studied in the thesis were in the as-built condition, i.e., without any heat-treatments. In this case, the obtained hardness values were in line with the ones found in the samples produced by DED, both around 400 HV. The L-PBF technique, instead, achieved rather low hardness values, around 330 HV. The conventional methods reached values around 350 HV. So, the samples produced by Prima Additive were amongst the hardest ones.

However, as extensively discussed in Chapter 2, the 17-4 PH stainless steel lends itself well to heat treatments that can increase its hardness. For this reason, different heat treatments are commonly performed, so they are contemplated in the majority of studies and applications. In almost every case, the solution annealing heat treatment (1100°C for 1 hour) caused a decrease in the hardness, up to 10%. On the contrary, if the solution annealing was followed by an ageing heat treatment (480°C for 1 hour), a considerable increase in the hardness was always recorded, up to 50% more than the as-built condition. Thus, if a high hardness is desired, a solution annealed followed by an ageing is the recommended heat treatment. In fact, the hardness of the samples might reach the values of 520-530 HV, as suggested in studies [37], [38].

Summing up all the analysis on the cubes, the preliminary observations concluded that an insufficient LED, when associated to high hatching distance and z-step, caused an unacceptable geometrical instability. The samples #3 and #6 were, indeed, the most critical. On the contrary, a too high LED (above 80%) caused a poor surface finish, with many adhered particles (samples #1 and, at lower extent, #4). This might be problematic

in case of objects with small geometries because an invasive post-processing treatment would not be feasible. The most promising set of parameters were #2, #5 (that is the same of #8) and #7. The overall porosities of the samples were very low, even if the worst samples (#3 and #6) exhibited large and numerous pores and defects. These two samples also showed the lowest hardness. The most promising samples had a very similar porosity and hardness, so, another parameter considered: the build rate. The samples #5 and #8 had a build rate higher than the #7 and #2 of almost 17% and 12%, respectively. This, for sure, represents a great advantage for the manufacturer in terms of both time and costs.

5 Conclusions

In this thesis project, different samples in 17-4 PH realized by Directed Energy Deposition were examined, investigating how process parameters affected their geometrical and structural characteristics. First of all, the powder was analysed, determining its particle size distribution and the relative D10, D50 and D90 parameters. Morphology of particles was mostly round, even if many defects were present, such as satellites. Flowability and density were calculated, finding excellent results.

Single Scan Tracks were observed on-top and in cross-section views. The former highlighted some issues in samples produced at minimum and maximum laser power. Cross-section analysis consisted in the evaluation of the geometrical characteristics of meltpools (width, growth, depth, G/D) and also in calculation of powder efficiencies (P_e). According to G/D evaluations, the lower powder feed rate was preferable and higher P_e values were achieved by high power and medium-high scanning speed samples.

Massive Cubes were extensively analysed. Vicker's microhardness was evaluated at different heights within the cubes, discovering a decrescent trend with the height. The average hardness were between 392 and 418 HV. Porosity was evaluated in terms of average values, obtaining very good results, between 0.030% and 0.092%. Further researches were carried on single pore dimension and their statistical distribution: small pores were more numerous but together covered a smaller area than the few large ones. Besides pores, under the SEM and optical microscope, other defects were spotted, such as fusion defects and partially melted powder particles. Finally, the martensitic and δ -ferrite microstructure was observed. The low number of samples available and their high number of changing process parameter did not allow to find a one-to-one correlation between characteristics and parameters. Despite that, a comparison between them allowed to find the best set of parameters.

Moreover, future studies and researches might be performed on the best set and on very similar combinations: for example, new samples might be built and tensile tests performed to investigate the effects on the mechanical properties.

References

- [1] I. Gibson, D. W. Rosen, and B. Stucker, *Additive manufacturing technologies: Rapid prototyping to direct digital manufacturing*. Springer US, 2010.
- [2] "http://www.esa.int/ESA_Multimedia/Images/2014/04/Additive_Manufacturing_process." .
- [3] M. K. Niaki and F. Nonino, "The Management of Additive Manufacturing Enhancing Business Value. Springer Series in Advanced Manufacturing," 2018. [Online]. Available: <http://www.springer.com/series/7113>.
- [4] A. Salmi, P. Minetola, and A. Saboori, "Additive Manufacturing Systems and Materials," Course Slides - Politecnico di Torino, 2019.
- [5] T. S. Srivatsan and T. S. Sudarshan, *Additive Manufacturing*. CRC Press, 2015.
- [6] M. Srivastava, S. Rathee, S. Maheshwari, and T. K. Kundra, *Additive Manufacturing*. Boca Raton, FL : CRC Press/Taylor & Francis Group, 2019.: CRC Press, 2019.
- [7] G. J. Peacock, "Method of making composition horseshoes," US746143A, 1902.
- [8] T. Wohlers and T. Gornet, *History of Additive Manufacturing*, Wohlers Reports. 2014.
- [9] C. Hull, "Apparatus for production of three-dimensional objects by stereolithography," US Patent 4,575,330, 1984.
- [10] "https://www.3dsystems.com/our-story." .
- [11] R. Larson, "Method and device for producing three-dimensional bodies," US Patent 5786562A, 1993.
- [12] G. Kim et al., "Three-Dimensional Printing: Basic Principles and Applications in Medicine and Radiology," *Korean Journal of Radiology*, vol. 17, p. 182, Feb. 2016, doi: 10.3348/kjr.2016.17.2.182.
- [13] R. Sanders, L. Forsyth, and K. Philbrook, "3-D Model maker," US Patent 5506706, 1996.
- [14] L. Yang et al., "Additive Manufacturing of Metals: The Technology, Materials, Design and Production Springer Series in Advanced Manufacturing," 2017. [Online]. Available: <http://www.springer.com/series/7113>.
- [15] "https://www.ansa.it/canale_motori/notizie/componentie_tech/2020/03/23/coronavirus-stampanti-3d-strategiche-per-supporti-medicali_c8e6d71c-a02f-4aa4-85a0-fc5fe3547685.html." .
- [16] A. Ahrari, K. Deb, S. Mohanty, and J. H. Hattel, "Multi-Objective Optimization of Cellular Scanning Strategy in Selective Laser Melting," 2017.
- [17] "https://www.lastampa.it/cronaca/2020/03/14/news/coronavirus-mancano-le-valvole-in-rianimazione-facciamole-con-la-stampante-3d-1.38593309." .
- [18] "https://clustercollaboration.eu/open-calls/amable-calls-ideas-additive-manufacturing-covid-19." .
- [19] S. Tornincasa and E. Chirone, *Disegno tecnico industriale*, vol. 1. Edizioni Il Capitello, 2014.
- [20] "https://www.loc.gov/preservation/digital/formats/fdd/fdd000504.shtml." .

- [21] S. L. Sing, C. F. Tey, J. H. K. Tan, S. Huang, and W. Y. Yeong, "2 - 3D printing of metals in rapid prototyping of biomaterials: Techniques in additive manufacturing," in *Rapid Prototyping of Biomaterials (Second Edition)*, Second Edition., R. Narayan, Ed. Woodhead Publishing, 2020, pp. 17–40.
- [22] F. Wirth, S. Arpagaus, and K. Wegener, "Analysis of melt pool dynamics in laser cladding and direct metal deposition by automated high-speed camera image evaluation," *Additive Manufacturing*, vol. 21, pp. 369–382, May 2018, doi: 10.1016/j.addma.2018.03.025.
- [23] Z. Yu et al., "Effect of laser remelting processing on microstructure and mechanical properties of 17-4 PH stainless steel during laser direct metal deposition," *Journal of Materials Processing Technology*, vol. 284, Oct. 2020, doi: 10.1016/j.jmatprotec.2020.116738.
- [24] B. Abiodun, Sisa Pityana, Mxolisi Brendon Shongwe, and Titilayo Akinlabi Esther, "Effect of Scanning Speed on Laser Deposited 17-4PH Stainless Steel," 2017.
- [25] "<https://www.primaadditive.com/the-laser-metal-deposition-process/>."
- [26] "<https://www.forgemag.com/articles/84865-the-use-of-direct-metal-deposition-dmd-additive-manufacturing-on-forging-dies/>."
- [27] "<https://www.spilasers.com/application-additive-manufacturing/what-is-laser-metal-deposition>"
- [28] D. C. Hofmann *et al.*, "Developing Gradient Metal Alloys through Radial Deposition Additive Manufacturing," *Scientific Reports*, vol. 4, no. 1, May 2015, doi: 10.1038/srep05357.
- [29] A. Aversa *et al.*, "The role of Directed Energy Deposition atmosphere mode on the microstructure and mechanical properties of 316L samples," *Additive Manufacturing*, vol. 34, Aug. 2020, doi: 10.1016/j.addma.2020.101274.
- [30] A. Popovich and V. Sufiiarov, "Metal Powder Additive Manufacturing," in *New Trends in 3D Printing*, InTech, 2016.
- [31] M. Boniardi and A. Casaroli, "Stainless steels Gruppo Lucefin Research & Development," 2014.
- [32] S. Barella and A. Gruttadauria, *Metallurgia e Materiali Non Metallici*, Esculapio. 2016.
- [33] "<https://www.welderdestiny.com/dissimilar-metals-welding.html>."
- [34] ASM International, "Alloy Digest Sourcebook: Stainless Steels," 2000. [Online]. Available: www.asminternational.org.
- [35] H. K. Rafi, D. Pal, N. Patil, T. L. Starr, and B. E. Stucker, "Microstructure and Mechanical Behavior of 17-4 Precipitation Hardenable Steel Processed by Selective Laser Melting," *Journal of Materials Engineering and Performance*, vol. 23, no. 12, pp. 4421–4428, Dec. 2014, doi: 10.1007/s11665-014-1226-y.
- [36] A. Yadollahi, N. Shamsaei, S. M. Thompson, A. Elwany, and L. Bian, "Mechanical and microstructural properties of selective laser melted 17-4 ph stainless steel," in *ASME International Mechanical Engineering Congress and Exposition, Proceedings (IMECE)*, 2015, vol. 2A-2015, doi: 10.1115/IMECE2015-52362.
- [37] I. Mathoho, E. T. Akinlabi, N. Arthur, M. Tlotleng, and N. W. Makoana, "The effects of LENS Process parameters on the behaviour of 17-4 PH stainless steel."

- [38] I. Mathoho, E. T. Akinlabi, N. Arthur, and M. Tlotleng, "Impact of DED process parameters on the metallurgical characteristics of 17-4 PH SS deposited using DED," *CIRP Journal of Manufacturing Science and Technology*, vol. 31, pp. 450–458, Nov. 2020, doi: 10.1016/j.cirpj.2020.07.007.
- [39] S. Cheruvathur, E. A. Lass, and C. E. Campbell, "Additive Manufacturing of 17-4 PH Stainless Steel: Post-processing Heat Treatment to Achieve Uniform Reproducible Microstructure," *JOM*, vol. 68, no. 3, pp. 930–942, 2016, doi: 10.1007/s11837-015-1754-4.
- [40] W. J. Oh, Y. Son, S. Y. Cho, S. W. Yang, G. Y. Shin, and D. S. Shim, "Solution annealing and precipitation hardening effect on the mechanical properties of 630 stainless steel fabricated via laser melting deposition," *Materials Science and Engineering A*, vol. 794, Sep. 2020, doi: 10.1016/j.msea.2020.139999.
- [41] A. Yadollahi, N. Shamsaei, S. Thompson, and D. Seely, "Effects of process time interval and heat treatment on the mechanical and microstructural properties of direct laser deposited 316L stainless steel," *Materials Science and Engineering A*, Dec. 2015.
- [42] A. Saboori et al., "An investigation on the effect of powder recycling on the microstructure and mechanical properties of AISI 316L produced by Directed Energy Deposition," *Materials Science and Engineering A*, vol. 766, Oct. 2019, doi: 10.1016/j.msea.2019.138360.
- [43] B. de La Batut, O. Fergani, V. Brotan, M. Bambach, and M. el Mansouri, "Analytical and Numerical Temperature Prediction in Direct Metal Deposition of Ti6Al4V," *Journal of Manufacturing and Materials Processing*, vol. 1, no. 1, p. 3, Jul. 2017, doi: 10.3390/jmmp1010003.
- [44] T. DebRoy et al., "Additive manufacturing of metallic components – Process, structure and properties," *Progress in Materials Science*, vol. 92. Elsevier Ltd, pp. 112–224, Mar. 01, 2018, doi: 10.1016/j.pmatsci.2017.10.001.
- [45] E. J. Pavlina and C. J. van Tyne, "Correlation of Yield Strength and Tensile Strength with Hardness for Steels," *Journal of Materials Engineering and Performance*, vol. 17, no. 6, Dec. 2008, doi: 10.1007/s11665-008-9225-5.
- [46] P. Guo, B. Zou, C. Huang, and H. Gao, "Study on microstructure, mechanical properties and machinability of efficiently additive manufactured AISI 316L stainless steel by high-power direct laser deposition," *Journal of Materials Processing Technology*, vol. 240, pp. 12–22, Feb. 2017, doi: 10.1016/j.jmatprotec.2016.09.005.
- [47] F. Ahmed et al., "Study of powder recycling and its effect on printed parts during laser powder-bed fusion of 17-4 PH stainless steel," *Journal of Materials Processing Technology*, vol. 278, Apr. 2020, doi: 10.1016/j.jmatprotec.2019.116522.
- [48] D. Pacucci, "Ottimizzazione del processo Direct Energy Deposition dell'acciaio H13," 2019.
- [49] "<http://www.fsg-international.com/cnc-shop-machine-tool-fiber-laserjan-3-fibermak-momentum-sm-40003000-x-1500.html>".
- [50] A. Lucenti, "Effetti dei trattamenti termici sulle microstrutture e sulle proprietà meccaniche dell'acciaio AISI 316L da Deposizione Diretta," 2019.
- [51] "www.phenom-world.com".

- [52] "<http://www.labulk.com/astmb212-free-flowing-metal-powders-apparent-density-hall-flowmeter-funnel/>."
- [53] "<https://www.leica-microsystems.com/products/>."
- [54] "<https://sites.google.com/site/gobanengineeringnotes/materials-testing/hardness-testing/vickers-hardness-test?tmpl=%2Fsystem%2Fapp%2Ftemplates%2Fprint%2F&showPrintDialog=1>."
- [55] R. Biswal, A. K. Syed, and X. Zhang, "Assessment of the effect of isolated porosity defects on the fatigue performance of additive manufactured titanium alloy," *Additive Manufacturing*, vol. 23, pp. 433–442, Oct. 2018, doi: 10.1016/j.addma.2018.08.024.
- [56] A. Carrozza et al., "Single Scans of Ti-6Al-4V by Directed Energy Deposition: A Cost and Time Effective Methodology to Assess the Proper Process Window," *Metals and Materials International*, Jan. 2021, doi: 10.1007/s12540-020-00930-3.
- [57] D. McGlinchey, "Bulk Solids Handling: Equipment Selection and Operation," 2008.
- [58] L. Peng et al., "Direct laser fabrication of nickel alloy samples," *International Journal of Machine Tools and Manufacture*, vol. 45, no. 11, pp. 1288–1294, Sep. 2005, doi: 10.1016/j.ijmachtools.2005.01.014.
- [59] E. Capello and B. Previtali, "The influence of operator skills, process parameters and materials on clad shape in repair using laser cladding by wire," *Journal of Materials Processing Technology*, vol. 174, no. 1–3, pp. 223–232, May 2006, doi: 10.1016/j.jmatprotec.2006.01.005.
- [60] U. de Oliveira, V. Ocelík, and J. T. M. de Hosson, "Analysis of coaxial laser cladding processing conditions," *Surface and Coatings Technology*, vol. 197, no. 2–3, pp. 127–136, Jul. 2005, doi: 10.1016/j.surfcoat.2004.06.029.
- [61] "<https://www.olympus-ims.com/en/insight/breaking-down-the-technical-cleanliness-workflow-part-2/>."
- [62] P. Wang, H. Lei, X. Zhu, H. Chen, and D. Fang, "Influence of manufacturing geometric defects on the mechanical properties of AlSi10Mg alloy fabricated by selective laser melting," *Journal of Alloys and Compounds*, vol. 789, pp. 852–859, Jun. 2019, doi: 10.1016/j.jallcom.2019.03.135.
- [63] S. Kleszczynski and A. Elspaß, "Influence of isolated structural defects on the static mechanical properties of PBF-LB/M components," in *Procedia CIRP*, 2020, vol. 94, pp. 188–193, doi: 10.1016/j.procir.2020.09.036.
- [64] D. Herzog, K. Bartsch, and B. Bossen, "Productivity optimization of laser powder bed fusion by hot isostatic pressing," *Additive Manufacturing*, vol. 36, Dec. 2020, doi: 10.1016/j.addma.2020.101494.
- [65] A. A. Adeyemi, E. Akinlabi, R. M. Mahamood, K. O. Sanusi, S. Pityana, and M. Tlotleng, "Influence of laser power on microstructure of laser metal deposited 17-4 ph stainless steel," *IOP Conference Series: Materials Science and Engineering*, vol. 225, p. 012028, Aug. 2017, doi: 10.1088/1757-899x/225/1/012028.
- [66] LeBrun, T.; Nakamoto, T.; Horikawa, K.; Kobayashi, H. "Effect of retained austenite on subsequent thermal processing and resultant mechanical properties of selective laser melted 17–4 PH stainless steel." *Mater. Des.* 2015, 81, 44–53.

- [67] Irrinki, H.; Jangam, J.S.D.; Pasebani, S.; Badwe, S.; Stitzel, J.; Kate, K.; Gulsoy, O.; Atre, S.V. Effects of particle characteristics on the microstructure and mechanical properties of 17–4 PH stainless steel fabricated by laser-powder bed fusion. *Powder Technol.* 2018, 331, 192–203.
- [68] P. K. Samal, N. N. North, A. Hoganas, I. Hauer, and H. Ab, “Properties of 17 – 4 PH stainless steel produced via press and sinter route.”
- [69] Grupo Lucefin. (2018). Precipitation Hardening Stainless Steel. http://www.lucefin.com/wp-content/files_mf/1.4542pha63062.pdf
- [70] ASTM B213–17 Standard test methods for flow rate of metal powders using the hall flowmeter funnel, ASTM Int.
- [71] ASTM B212–17 Standard Test Method for Apparent Density of Free-Flowing Metal Powders Using the Hall Flowmeter Funnel, ASTM Int.
- [72] D. R. Eo, S. H. Park, and J. W. Cho, “Controlling inclusion evolution behavior by adjusting flow rate of shielding gas during direct energy deposition of AISI 316 L,” *Additive Manufacturing*, vol. 33, May 2020, doi: 10.1016/j.addma.2020.101119.
- [73] H. Gu, H. Gong, D. Pal, K. Rafi, T. Starr, B. Stucker, Influences of energy density on porosity and microstructure of selective laser melted 17-4PH stainless steel, 2013 Solid Freeform Fabrication Symposium, 2013 474-89.
- [74] Z. E. Tan, J. H. L. Pang, J. Kaminski, and H. Pepin, “Characterisation of porosity, density, and microstructure of directed energy deposited stainless steel AISI 316L,” *Additive Manufacturing*, vol. 25, pp. 286–296, Jan. 2019, doi: 10.1016/j.addma.2018.11.014.